Experimental Studies of Magnetic Reconnection in 3D Geometries

ARCHIVES
MASSACHUSETTS INSTITUTE OF TECHNOLOGY
NOV 10 2014
LIBRARIES

by

Arturs Vrublevskis

B.A., Colby College (2007)

Submitted to the Department of Physics
in partial fulfillment of the requirements for the degree of

Doctor of Philosophy

at the

MASSACHUSETTS INSTITUTE OF TECHNOLOGY

September 2014

© Massachusetts Institute of Technology 2014. All rights reserved.

Signature redacted

Author ....
Department of Physics
August 19, 2014

Signature redacted

Certified by............ ....
Jan Egedal
Associate Professor
Thesis Supervisor

Signature redacted

Accepted by....... ....
Krishna Rajagopal
Professor of Physics, Associate Department Head for Education

Experimental Studies of Magnetic Reconnection in 3D Geometries

by

Arturs Vrublevskis

Submitted to the Department of Physics
on August 19, 2014, in partial fulfillment of the
requirements for the degree of
Doctor of Philosophy

Abstract

Magnetic reconnection is an important and prevalent plasma physics phenomenon occurring in astrophysical (solar flares), space (magnetospheric substorms), and laboratory settings (tokamak sawtooth oscillations). It allows for a change in the magnetic field topology in plasmas while also transferring the magnetic field energy to plasma energy. In return, the global magnetic field topology can affect the dynamics of reconnection. Major advances have been made in understanding reconnection in two dimensions, which, however, are not necessarily applicable to fully three dimensional settings. We aim to add to the fundamental understanding of reconnection in three dimensions through observations in controlled laboratory experiments.

To that effect we constructed and characterized an experimental setup at the Versatile Toroidal Facility that includes a washer plasma gun and a suite of diagnostics. We pulse a coil that drives reconnection along an X-line and also forms magnetic nulls in the plasma.

We theoretically and experimentally investigated the relevant magnetic field configurations of a current coil in a background magnetic field. Notably, a coil tilted with respect to the background field produces nested separatrix surfaces consisting of field lines that encircle the null coil a certain number of times. The results are, to the best of our knowledge, original and contain features of relevance to the interaction of the Earth's magnetic field with the interplanetary magnetic field.

In addition, we observed diamagnetic currents near the null points and magnetic reconnection along the X-line. The effective resistivity of the current sheet is significantly larger than the classical Spitzer resistivity. Thus, the observed reconnection cannot be explained as Sweet-Parker reconnection mediated by the classical resistivity. The reconnection current sheet extends to an azimuthal current sheet around the plasma beam. The azimuthal current sheet also is consistent with diamagnetic currents.

Thesis Supervisor: Jan Egedal
Title: Associate Professor

Acknowledgments

It has been a long and challenging journey and I am thankful to the people who supported me. First of all, I am grateful to my thesis advisor, Prof. Jan Egedal, for taking me on as a graduate student and for his support. I would also like to thank Prof. John Belcher and Prof. Enectali Figueroa-Feliciano for serving on my thesis committee. Thanks to the VTF group, especially Dr. Ari Le and Dr. Obioma Ohia who were colleagues but will continue to be dear friends.

Prof. Belcher deserves additional recognition for sharing his own experiences in a letter to "The Tech" and thus encouraging me and an unknown number of other students at MIT to seek help when needed.

I am grateful to Prof. Maris Knite and Prof. Gita Revalde at Riga Technical University for their support, trust, and patience while I was still finishing my thesis.

I am thankful to my family. Most importantly, I am thankful to my wife Nora and son Atis for their unwavering love. I belong to them.

Contents

1 Introduction **21**

1.1 Importance of Magnetic Reconnection 25
1.2 Reconnection Basics in 2D 27
  1.2.1 Flux Conservation in Ideal Plasmas 27
  1.2.2 Magnetic Diffusion 28
  1.2.3 Sweet-Parker Reconnection 29
  1.2.4 Hall Reconnection 31
  1.2.5 Remaining Questions 32
1.3 Reconnection in 3D 32
  1.3.1 Importance of Reconnection in 3D 32
  1.3.2 3D Reconnection Basics 33
  1.3.3 3D Reconnection in Magnetosphere 39
  1.3.4 Experimental investigations 42
1.4 Thesis Objectives and Outline 43

2 Experimental Setup **45**

2.1 The Versatile Toroidal Facility 45
2.2 Setup for 3D Reconnection Experiments 47
  2.2.1 Null Coil 49
  2.2.2 Experimental Procedure 52
2.3 Parameters 53
2.4 Diagnostics 54
  2.4.1 Rogowski Probes 55

2.4.2 Magnetic Coil Array 58
2.4.3 Langmuir Probe Array 65
2.4.4 Fast Camera 71

3 Plasma Gun **73**
3.1 Basic Principles 73
3.2 Implementation 74
3.3 Electronics 77
3.4 Plasma Gun Currents 79

4 Expected Field Configurations **83**
4.1 Normal 83
4.1.1 With X-points 84
4.1.2 With Null Points 85
4.2 Tilted 89
4.2.1 Null Coil Field Dominates 89
4.2.2 Background Field Dominated and Limiting Configurations . . 96

5 Plasma Beam Oscillations **99**
5.1 Observations 99
5.1.1 Current Signatures 99
5.1.2 Density Signatures 103
5.2 Interpretation 110
5.2.1 Kink Instability 110
5.2.2 Drift Waves 111

6 Results for the Normal Configuration **113**
6.1 Magnetic Field Structure 113
6.2 Current Structure 116
6.3 Plasma Density Structure 126
6.4 Electron temperature 131
6.5 Magnetic Coil Array Measurements 133

6.5.1 Diamagnetic Currents Across Separatrices 133

6.5.2 Reconnection and Azimuthal Current Sheet 137

6.6 Summary and Interpretation 139

7 Results for the Tilted Configuration **141**

7.1 Magnetic Field Structure 141

7.2 Current and Plasma Density Structures 144

7.3 Interpretation 145

8 Discussion and Conclusions **149**

List of Figures

1-1 Basic ideas of reconnection. 23

1-2 Basic reconnection 2D setup including a current sheet. 24

1-3 (a) X-ray image of a solar flare. (b) Cartoon model of a solar flare. . 25

1-4 Basic setup of solar wind interaction with Earth magnetosphere. . . . 26

1-5 Basic Hall reconnection setup including the signature quadrupolar out-of-plane magnetic fields. 31

1-6 Possible setup for non-null reconnection in 3D. 35

1-7 Geometry and terminology of magnetic field nulls in 3D. 36

1-8 Torsional spine reconnection. 36

1-9 Torsional fan reconnection. 37

1-10 Spine-fan reconnection. 38

1-11 Magnetic field lines in two separator reconnection setups differing in the magnitude of current along the separator. 39

1-12 Magnetosphere vacuum model fields for the special case of IMF and dipole perfectly parallel. 40

1-13 Magnetosphere vacuum model fields for a 45° tilt between IMF and the dipole. 41

1-14 Time evolution of flux surfaces in the FRC experiments by Stenzel et al. 42

2-1 A photograph of VTF. 46

2-2 Coordinate systems used. 47

2-3 Toroidal and poloidal directions in a toroidal geometry. 48

2-4 Basic experimental setup. 49

2-5 View from the top of the basic setup in the toroidal VTF geometry. . 50

2-6 A photograph of the null coil mounted inside the vacuum chamber with probe arrays attached. 51

2-7 Circuit for pulsing the null coil. 52

2-8 Top: current in a null coil turn and the corresponding expected total magnetic field at the center of the coil from all 12 turns as a function of time. Middle: gun discharge current. Bottom: gun anode bias current. 53

2-9 Left: basic principles of a Rogowski probe. Right: photograph of the Rogowski probe array. 56

2-10 The basics of the effective circuit for the Rogowski probes. 57

2-11 Left: basic principles of a magnetic coil. Right: diagram of the magnetic coil array used. 59

2-12 Magnetic coil array mounted on top of the Rogowski probe array. . . 60

2-13 Electric circuit for measuring the output voltage of the magnetic coils using digitizers. 61

2-14 Top: an example of the measured fields in two of the magnetic coils. Middle: same as top with vacuum fields subtracted. Bottom: magnetic fields in channel 4 due to plasma currents obtained after further subtracting a fit for the magnetic field component due to the phase shift in the null coil. 63

2-15 An example of the magnetic fields due to the plasma current for a row of the magnetic coils. 64

2-16 Example Langmuir trace for a select probe and time. 67

2-17 Left: schematic of a single Langmuir probe. Right: photograph of two probes as part of a probe string. 68

2-18 Single-string Langmuir probe set mounted on top of the Rogowski array. 69

2-19 Electric circuit for measuring the Langmuir probe current using digitizers. 69

3-1 Basic principles of the plasma gun operation. 74

3-2 An example actual design of a washer plasma gun (RWM facility). . . 75

3-3 Early version of the assembled gun (left) and with the ceramic housing removed (middle and right). 75

3-4 Close up view of the gun with the ceramic housing removed. 76

3-5 Main components of the plasma gun electronics. 78

3-6 The main plasma gun currents (discharge I_{dis} and bias I_{bias}) and the location of the separate Rogowski coils. 79

3-7 The measured current components I_{bias}, I_{gun}, and I_{GND} of the gun anode bias current. 80

3-8 The oscillatory component evident in the I_{gun} and I_{GND} current measurements. 81

4-1 Representative open, closed, and separator field lines with the null coil's dipole parallel to the background field. 85

4-2 Representative field lines with the null coil's dipole antiparallel to the background field and an X-line radially inside the null coil. 86

4-3 Representative field lines with the null coil's dipole antiparallel to the background field and one null point formed. 87

4-4 Representative field lines with the null coil's dipole antiparallel to the background field and two null points formed. 87

4-5 Representative field lines in 3D with the null coil's dipole antiparallel to the background field and two null points formed. 88

4-6 Representative field lines in the x-y plane with the null coil tilted, it's dipole antiparallel to the background field and two null points formed. Null coil field dominates. 90

4-7 Representative field lines in 3D with the null coil tilted, it's dipole antiparallel to the background field and two null points formed. Null coil field dominates. 91

4-8 Representative field lines in 3D with the null coil tilted, it's dipole antiparallel to the background field and two null points formed. Null coil field dominates. View along the negative z-axis. 92

4-9 Number of times a field line starting at a given coordinate in the x-z plane and at Y = -0.2 encircles the null coil for the tilted and null coil field dominated configuration 93

4-10 Separatrix surfaces originating from the lower null point corresponding to different encirclement numbers. 93

4-11 Complementary separatrix surfaces of the two null points for different encirclement numbers. 94

4-12 Separators for encirclement numbers zero, one, and two connecting the two null points. 94

4-13 Nested separatrix surfaces originating from the lower null point corresponding to different encirclement numbers. 95

4-14 Representative field lines in the x-y plane with the null coil tilted, it's dipole antiparallel to the background field, and two null points formed. Background field dominates. 96

4-15 Representative field lines in the x-y plane with the null coil tilted, it's dipole antiparallel to the background field, and two null points formed. This is the limiting case between the background and null coil field dominated configurations. 97

5-1 The measured current components I_{bias}, I_{gun}, and I_{GND} of the gun anode bias current where the latter two exhibit prominent oscillatory component. The null coil was not fired. 100

5-2 The measured current oscillations at the gun output and summed over all of the Rogowski probe array coils. Also shown is the total signal of the Rogowski probe array coils in the inner-most band and in the center coil. 101

5-3 The measured oscillations of four Rogowski array coils in the inner band separated by 90 degrees, shifted in time correspondingly, and shifted vertically. 102

5-4 Measured current density oscillations in data frames from a single oscillation period. The null coil is not fired. 106

5-5 Plasma density measured by the single-string Langmuir probes at different x-coordinates at five different times during a single oscillation period consistent with a plasma beam oscillating in the x-coordinate. 107

5-6 Density and current oscillations during a compression phase between two null phases. 108

5-7 Left: average beam density measured by the single-string Langmuir probes. Right: the Langmuir characteristics and the corresponding electron temperature ranges as a result of the gyrating beam. 109

5-8 Right: basic setup for a drift wave where a cylindrical beam of plasma stretches along the background magnetic field with azimuthal density perturbations. Left: density oscillations out of phase with an opposing E×B drift leads to oscillations. 111

6-1 Plasma beam before the beam bias is applied and the null coil is fired in a visible light fast camera image from the top view. 114

6-2 Plasma beam before the beam bias is applied and the null coil is fired in a visible light fast camera image from the bottom view. 114

6-3 Fast camera top view during the null phase. 115

6-4 Fast camera bottom view during the null phase. 115

6-5 Modulation of the oscillations in the total plasma current at the gun output as the null coil current is pulsed. 117

6-6 Anti-correlated current fluctuations in the probes radially inside the null coil and radially outside the null coil during the null phase. . . . 118

6-7 Current fluctuations as measured with the Rogowski probe array at select times during a null phase. 122

6-8 Left: current fluctuations in four coils averaged over ten shots. Right: the average current density from the whole Rogowski array at one select time frame. 123

6-9 Modulation of the oscillations in the total plasma current at the gun output as the null coil current is pulsed for the case when the beam is displaced with respect to the null coil and intersects the Rogowski probe array at the inner probe band. 124

6-10 Current fluctuation sums in the probes radially inside the null coil and radially outside the null coil during the null phase for the case of plasma beam displaced with respect to the null coil. 125

6-11 Plasma density as measured by the single-string Langmuir probes radially outside the null coil at X = 14.7 cm (green), X = 16.0 cm (black), and X = 17.2 cm (blue). 126

6-12 Average density evolution in time. 128

6-13 Average plasma density measured by a single probe upstream of the null coil (Y = -12.5 cm, blue) and downstream of the null coil (Y = +12.5 cm, black). 129

6-14 Average density evolution in time for the normal configuration with plasma beam displaced. 130

6-15 Electron temperature at select times. 132

6-16 The measured z-component of the plasma current at select times. . . 135

6-17 An example measured B_y component of the magnetic field due to pronounced inferred azimuthal plasma currents. 136

6-18 The expected diamagnetic current polarities near null points based on pressure gradient and magnetic field directions. 136

6-19 The empirical scaling for the effective resistivity in MRX. 138

6-20 The expected diamagnetic current polarities for the plasma beam. . . 139

7-1 Plasma beam before the beam bias is applied and the null coil is fired in a visible light fast camera image from the bottom view. 142

7-2 Fast camera bottom view during the null phase for the tilted configuration. 142

7-3 Fast camera top view during the null phase for the tilted configuration. 143

7-4 Fast camera bottom view for a displaced plasma beam before bias is applied but the null coil is already fired. 143
7-5 Modulation of the oscillations in the total plasma current at the gun output as the null coil current is pulsed for the tilted configuration. . 144
7-6 Anti-correlated current fluctuations in the probes radially inside the null coil and radially outside the null coil during the null phase for the tilted configuration. 145
7-7 Average density evolution in time for the tilted configuration. 147

List of Tables

2.1 Timing schedule for the experiments performed 53
2.2 Typical plasma parameters in our experiments 54

Chapter 1

Introduction

The Sun is not only the source of almost all energy on Earth but also emits plasma in the form of solar wind that travels well beyond the Earth orbit. This plasma consists of a significant fraction of charged particles, thus the release, dynamics, energization, and the effects of it on Earth are regulated by the Sun's, Earth's, and interplanetary magnetic fields (IMF). In the ideal plasma model magnetic flux through a given plasma element is constant. In this model then the space around the Earth governed by the Earth's constant magnetic field - the magnetosphere - would not be affected by the solar wind engrossed in the interplanetary and solar magnetic fields. Contrary to these predictions, one does routinely observe the influence of varying degrees of the solar wind on magnetosphere in the form of aurorae and magnetic substorms. A non-ideal process that plays a significant role in this coupling between plasmas linked by fields of different origins is magnetic reconnection and it is the goal of this thesis to advance the fundamental understanding of this process through observations in controlled laboratory experiments.

We first loosely define magnetic reconnection as topological restructuring of magnetic fields caused by a change in connectivity of field lines in the presence of plasma [1–5]. This idea is illustrated in Fig. 1-1 from [6] where in (a) and (b) we are following time evolution $t_1 - t_3$ of magnetic fields and plasma elements A-D. In an ideal plasma (a), any two plasma elements A and B that at time t_1 are on the same field line will remain connected by a field line at all later times t_2 and t_3. This no longer holds true if reconnection takes place. In (b) at t_1 the plasma evolution is still ideal and two roughly opposite field lines are moving towards each other together with the given labeled plasma elements. At t_2 an X-point forms and reconnection occurs as a result of which at t_3 it is plasma elements A and C connected with the same field line instead of the original A and B. Further time evolution for these plasma elements can again be ideal.

Usually, as a result of reconnection some of the magnetic field energy is transformed into the plasma kinetic energy and the plasma on the newly reconnected field line flows rapidly away from the reconnection region. This acceleration can also be interpreted as plasma again following the field evolution as the bent reconnected field lines straighten out. These flows are illustrated in (c) where generic 2D reconnection setup is translated in the third dimension and the plasma flows are illustrated with colored arrows - inflow in green and the accelerated outflow in red.

The opposite reconnecting fields of the two inflow regions require a current along the X-line. This current self-consistently generates fields and forms an extended current sheet shown in two dimensions in red in Fig. 1-2 from [4]. Any finite magnetic field component along this X-line direction is called the guide field.

To summarize, one could possibly expect reconnection in plasmas where field lines with some opposite components meet. In the basic setup a current sheet forms, field lines reconnect at an X-point, and plasma gets accelerated and ejected out of the reconnection region along with the newly reconnected field lines.

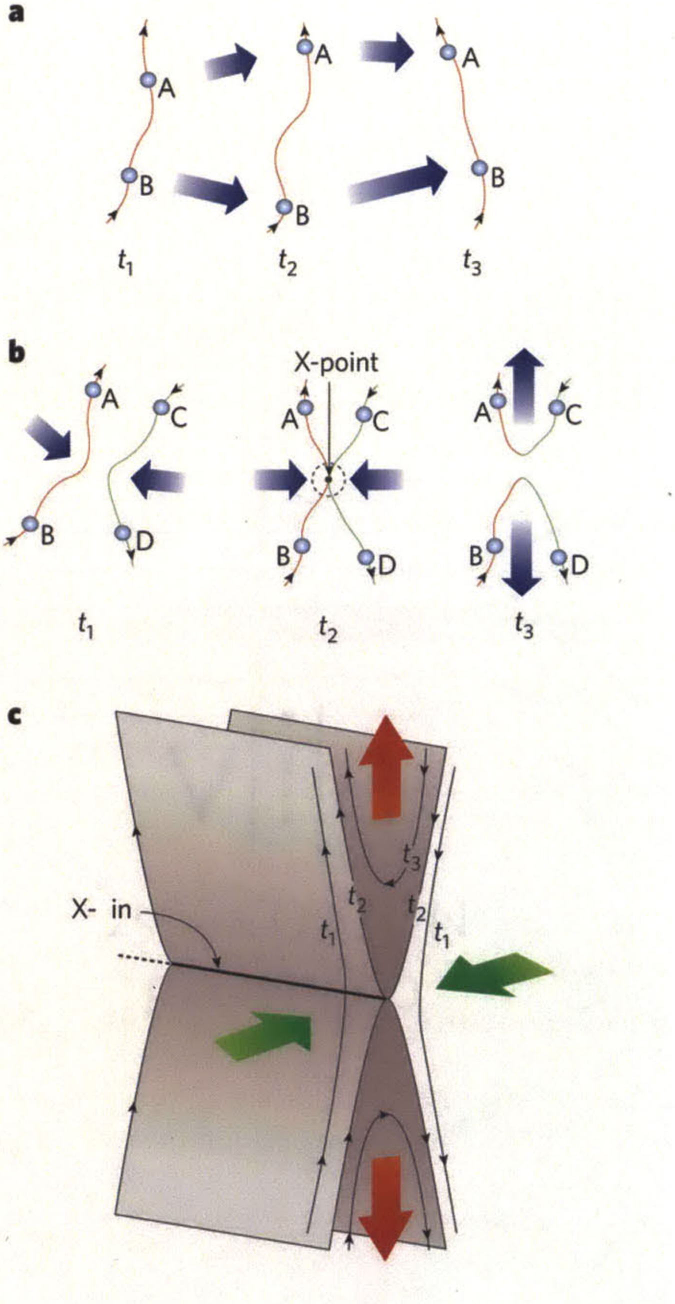
a
A
B
A
B
A
B
t_1
t_2
t_3
b
X-point
A
C
B
D
A
C
B
D
A
C
B
D
t_1
t_2
t_3
c
X- in
t_3
t_2
t_2
t_1
t_1

Figure 1-1: Basic ideas of reconnection. In (a) and (b) we are following time evolution of magnetic fields and plasma element. In an ideal plasma (a), any two plasma elements on the same field line will remain connected by a field line at all later times. In (b) reconnection takes place at t_2 and connectivity of plasma changes. (c) illustrates flows in the basic reconnection setup. Reproduced from [6].

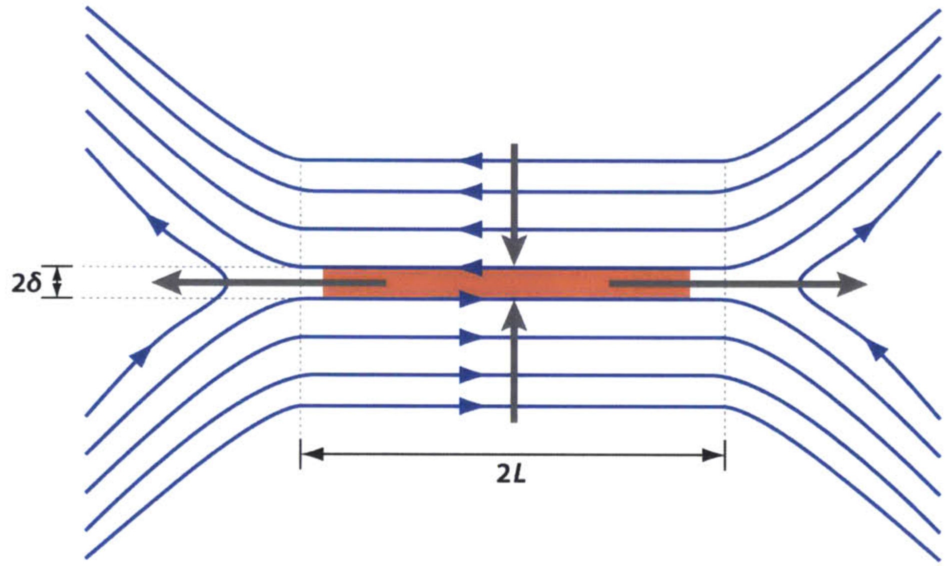

Zweibel EG, Yamada M. 2009.
Annu. Rev. Astron. Astrophys. 47:291–332

Figure 1-2: Basic reconnection 2D setup including a current sheet (red). Reproduced from [4].

1.1 Importance of Magnetic Reconnection

The importance of magnetic reconnection lies in its prevalence and consequences in various nature and laboratory settings. Reconnection is widely used to describe processes on the Sun such as solar flares [7, 8] and coronal mass ejections (CMEs) [9]. Flares are observed to release as much as 10^{25} J of energy in a matter of hours. This is explained as accumulation of magnetic energy on longer time scales followed by a rapid conversion and release in the form of plasma energy through the process of reconnection. An example X-ray image together with a cartoon model are shown in Fig. 1-3 from [8].

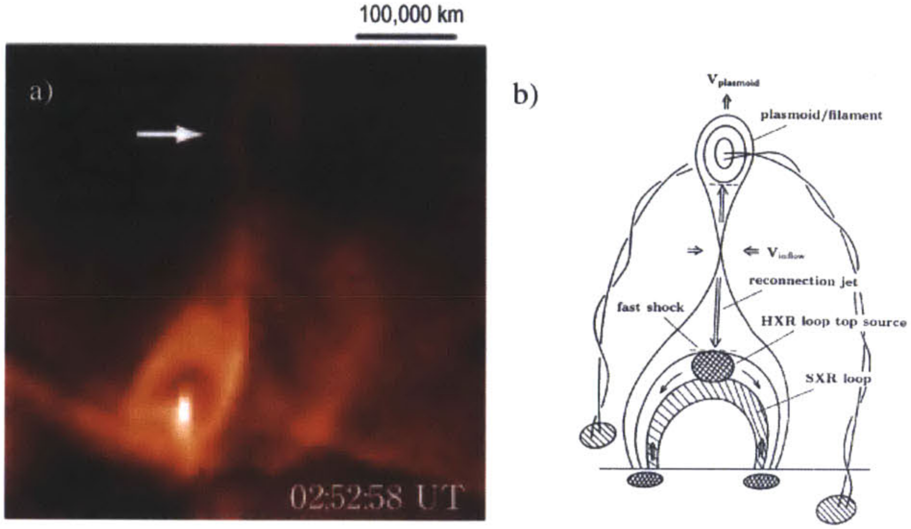

Figure 1-3: (a) X-ray image of a solar flare. (b) Cartoon model of a solar flare. Note the characteristic reconnection geometry and the marked outflow jet. Reproduced from [8].

Since the heliosphere is by definition filled with solar wind plasma and, in addition, can have regions of interplanetary fields with different directions, then reconnection can be observed in the heliosphere beyond the Sun. Examples include the solar wind in general [10] and its interaction with Earth's magnetosphere in particular [11, 12]. The basic setup for magnetosphere and the two general regions where reconnection is observed are shown in Fig. 1-4 with the time evolution of field lines as numbered. There solar wind with, in this case, a predominantly southward IMF is traveling from the Sun on the left far outside of the figure and towards Earth and its southward pointing dipole field. First, reconnection can happen on the dayside of the magnetosphere between the IMF and the Earth magnetic field. Second, reconnection can happen on the nightside where the solar wind has stretched oppositely pointing Earth magnetic field lines (see lines 5 and 5' in Fig. 1-4) forming Earth's magnetotail. The exact location and nature of reconnection within these two general regions, especially on the dayside, depends sensitively on solar wind conditions and is a topic of ongoing research. In addition, the setup is inherently three dimensional and is further discussed in Section 1.3.3.

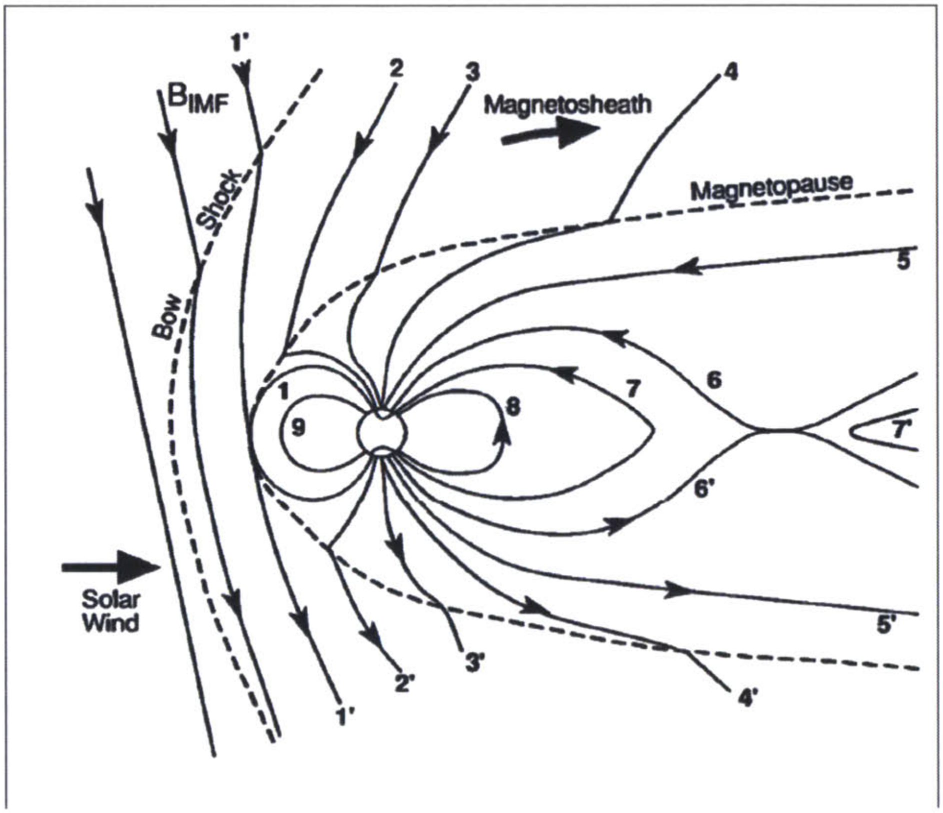

Figure 1-4: Basic setup of solar wind interaction with Earth magnetosphere. The two general regions where reconnection is observed are on the dayside and in the magnetotail. Reproduced from [12].

As a consequence of reconnection in magnetosphere, IMF and Earth magnetic field lines temporarily connect and solar wind plasma can stream along them towards Earth atmosphere resulting in magnetic substorms and auroras. If magnetosphere is also impacted by a CME, then through reconnection enough energetic solar wind particles can couple to magnetosphere to have potentially significant consequences for civilization. For example, the energetic particle flux can damage satellites while induced ground currents can lead to failures in the power grid and blackouts.

Magnetic reconnection is expected to occur outside of the heliosphere as well. For example, since dynamo theories require topological changes in magnetic fields then one can expect reconnection to take place in stars, galaxies, and possibly even accretion disks. More exotic occurrences would include magnetars [13].

On Earth, reconnection is observed in laboratory plasma experiments. For example, it is manifested in sawtooth oscillations and disruptive instabilities in tokamak plasmas [14–16], which are of consequence for any future tokamak fusion reactors. In addition, reconnection is also systematically investigated in dedicated reconnection experiments (see Section 1.3.4).

1.2 Reconnection Basics in 2D

1.2.1 Flux Conservation in Ideal Plasmas

The non-ideal nature of reconnection can be analyzed using the generalized Ohm's law in the two-fluid model for plasma, which for quasi-neutral hydrogen plasma is:

$$\mathbf{E} + \mathbf{U} \times \mathbf{B} = \eta \mathbf{J} + \frac{\mathbf{J} \times \mathbf{B}}{e n_e} - \frac{\nabla \cdot \mathbb{P}_e}{e n_e} - \frac{m_e}{e} \frac{d\mathbf{u}_e}{dt}. \tag{1.1}$$

Here $\mathbf{U}$ is the bulk plasma flow and $\mathbf{u}_e$ is the electron fluid flow velocity. Terms of the left-hand side of the equation can be interpreted as the electric field in the frame of reference of a given plasma fluid element. Ideal plasma would correspond to shorting all of internal electric fields or, mathematically, to having the right-hand side of the equation equal to zero. Indeed,

$$\mathbf{E} + \mathbf{U} \times \mathbf{B} = 0 \tag{1.2}$$

is the corresponding familiar equation from the ideal MHD model. Using Eq. 1.2 in Faraday's law

$$\frac{\partial \mathbf{B}}{\partial t} = -\nabla \times \mathbf{E} \tag{1.3}$$

we get

$$\frac{\partial \mathbf{B}}{\partial t} = \nabla \times (\mathbf{U} \times \mathbf{B}), \tag{1.4}$$

which can be rewritten in terms of the flux Φ enclosed by a given plasma element:

$$\frac{d\Phi}{dt} = 0. \tag{1.5}$$

Eq. 1.5 implies that reconnection is not possible in ideal plasma.

1.2.2 Magnetic Diffusion

A first attempt to account for the non-ideal nature of plasma would be to include electron-ion collisions and the resulting plasma resistivity η:

$$\eta = \frac{\nu_{ei} m_e}{e^2 n} \tag{1.6}$$

so that Eqs. 1.2 and 1.3 become, correspondingly,

$$\mathbf{E} + \mathbf{U} \times \mathbf{B} = \eta \mathbf{J} \tag{1.7}$$

and

$$\frac{\partial \mathbf{B}}{\partial t} = \nabla \times (\mathbf{U} \times \mathbf{B}) + \frac{\eta}{\mu_0} \nabla^2 \mathbf{B}. \tag{1.8}$$

The added term enables magnetic diffusion whereby magnetic flux through a plasma element resistively diffuses at a time scale given by the ratio of the third and the first term in Eq. 1.8:

$$\tau_R \sim \frac{\mu_0 L^2}{\eta}. \tag{1.9}$$

Here L is the length scale for field variations. While magnetic diffusion allows for a decoupling between plasma and magnetic flux, the time scales are not fast enough to explain all of the observed reconnection phenomena. For example, a magnetic field structure the size of a sunspot with $L \sim 10^7$ m at coronal temperature of 10^6 K would resistively dissipate only in $\tau_R \sim 10^7$ years.

1.2.3 Sweet-Parker Reconnection

Field reconfiguration on faster scales than magnetic diffusion requires magnetic reconnection. The basic model for reconnection both historically and in terms of complexity was developed by Sweet and Parker [17] and corresponds to Fig. 1-2. Here we estimate the scaling of reconnection rate within this model.

First, we apply Eq. 1.7 to the inflow region outside of the current sheet with essentially no current. There $E_i \sim U_i B_i$. Within the current sheet with essentially no magnetic field the same Eq. 1.7 gives $E_o \sim \eta J$. Assuming that the electric field does not change significantly between the two regions ($E_i \sim E_o$) then we have

$$U_i \sim \frac{\eta J}{B_i}. \tag{1.10}$$

Another equation relating J and the inflow magnetic field B_i is given by Ampere's law:

$$\mathbf{J} = \frac{1}{\mu_0} \nabla \times \mathbf{B} \Longrightarrow J \sim \frac{B_i}{\mu_0 \delta}. \tag{1.11}$$

Eqs. 1.10 and 1.11 together imply that the inflow speed is given by

$$U_i \sim \frac{\eta}{\mu_0 \delta}. \tag{1.12}$$

Next, conservation of mass for the given general geometry of the current sheet of width δ and length L (see Fig. 1-2) requires that

$$L U_i = \delta U_o, \tag{1.13}$$

where U_o is the plasma outflow speed.

Finally, we can write the pressure balance equation between the inflow and outflow regions:

$$\frac{B_i}{2\mu_0} + p_i + \frac{1}{2}\rho_i U_i^2 = \frac{B_o}{2\mu_0} + p_o + \frac{1}{2}\rho_o U_o^2. \tag{1.14}$$

We assume that plasma pressures p_i and p_o are small compared to the magnetic field pressures, that the magnetic field in the outflow B_o is small compared to the inflow field B_i, that inflow and outflow densities $\rho_i \sim \rho_o$ are similar, and that the inflow velocity U_i is small compared to the outflow velocity U_o. Eq. 1.14 then gives the following scaling for the outflow velocity in terms of the inflow Alfvén velocity $v_{A,i}$:

$$\frac{B_i}{2\mu_0} \sim \frac{1}{2}\rho U_o^2 \Longrightarrow U_o \sim \sqrt{\frac{B_i^2}{\mu_0 \rho}} = v_{A,i}. \tag{1.15}$$

We can then combine Eqs. 1.12, 1.13, and 1.15 to obtain the following scalings:

$$U_i \sim \sqrt{\frac{\eta v_{A,i}}{\mu_0 L}} = \frac{v_{A,i}}{\sqrt{S}} \tag{1.16}$$

$$\tau_{SP} = \frac{L}{U_i} = \frac{\tau_R}{\sqrt{S}} \tag{1.17}$$

where we have used the Lundquist number S, which is defined according to $S = \frac{\tau_R}{\tau_A}$ and describes the ratio between the second (convective) and third (diffusive) terms in Eq. 1.8 for a flow scaling with the Alfvén velocity. Here $\tau_A = \frac{L}{v_A}$.

Furthermore, Eqs. 1.13, 1.15, and 1.16 can be used to express the current sheet width δ in terms of the current sheet length L and the Lundquist number S:

$$\delta = L\,\frac{U_i}{U_o} \sim L\,\frac{\left(\frac{v_{A,i}}{\sqrt{S}}\right)}{v_{A,i}} \sim \frac{L}{\sqrt{S}}. \tag{1.18}$$

Eq. 1.17 implies that for large S the time scale for Sweet-Parker reconnection can be much shorter than the resistive diffusion time scale. For example, for the sunspotsized coronal structure from Section 1.2.2 with $S \sim 10^9$ the Sweet-Parker reconnection time scale is only $\tau_{SP} \sim 300$ years compared to $\tau_R \sim 10^7$ years. Nevertheless, even this significantly shorter timescale is still orders of magnitude too long.

1.2.4 Hall Reconnection

Reconnection faster than that explained by resistivity (through either magnetic diffusion or Sweet-Parker mechanism) is called collisionless reconnection. It can be described by retaining additional terms in the generalized Ohm's law (Eq. 1.1, repeated below):

$$\mathbf{E} + \mathbf{U} \times \mathbf{B} = \eta \mathbf{J} + \frac{\mathbf{J} \times \mathbf{B}}{en_e} - \frac{\nabla \cdot \mathbb{P}_e}{en_e} - \frac{m_e}{e} \frac{d\mathbf{u}_e}{dt}.$$

In addition to the resistivity term ηJ, the right-hand side includes the Hall $(J \times B)$ term, the electron pressure tensor $\mathbb{P}_e$ term, and the electron inertia term du_e/dt. It has been established in simulations [18] that the inclusion of the Hall and electron pressure terms can lead to collisionless reconnection with the basic model illustrated in Fig. 1-5 reproduced from [4]. The quadrupole out-of-plane magnetic field signature has been observed in both magnetosphere [19] and laboratory [20] reconnection settings.

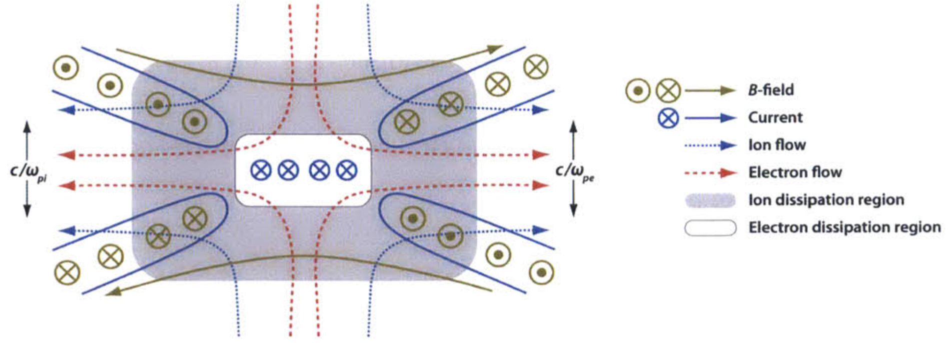

Zweibel EG, Yamada M. 2009.
Annu. Rev. Astron. Astrophys. 47:291–332

Figure 1-5: Basic Hall reconnection setup including the signature quadrupolar out-of-plane magnetic fields. Reproduced from [4].

1.2.5 Remaining Questions

Despite extensive research efforts and the progress outlined in previous chapters numerous unanswered questions regarding magnetic reconnection remain. These include but are not limited to the following:

- What mechanism is responsible for particle energization as observed, for example, in Earth's magnetotail [21]? Is the acceleration due to spatially large-scale parallel electric fields so that a single reconnection region provides all of the acceleration [22] or are multiple reconnection regions necessary so that electrons are repeatedly accelerated as they interact with numerous instances of reconnection [23]?

- How are the different reconnection length scales related? For example, how is the length of the current sheet related to the global system size?

- What regulates and triggers sudden transition from slow steady-state reconnection to fast explosive bursts resulting in CMEs and magnetic substorms?

- How is reconnection different in fully 3D geometries? Theoretical and computational research on reconnection often requires making the simplification of a 2D geometry for the problem to be tractable. However, theoretical and experimental observations suggest that reconnection in 3D geometries is both important and potentially different from its 2D analogue.

The question of reconnection in 3D geometries is further addressed in the following chapters and is the focus of this thesis.

1.3 Reconnection in 3D

1.3.1 Importance of Reconnection in 3D

Reconnection models discussed in previous chapters have assumed translational symmetry along the X-line. Since our working definition for reconnection references magnetic connectivity of plasma elements then this assumption has significant implications. Ideal translational symmetry of the 2D plane divided by separatrices would imply that there exist separatrix surfaces dividing the full 3D space into regions that are not interconnected with magnetic field lines. Ideal plasma in one region would always remain in that region spare reconnection. If, however, the familiar 2D geometry is localized along the third dimension, then the apparent 2D reconnection topology and dynamics do not necessarily have to translate to physical plasma effects in the full 3D space.

In addition to theoretical considerations, research in 3D reconnection is motivated by experimental observations. A prominent location for localized reconnection regions in general and magnetic null points in particular is in the solar atmosphere ([24] and refs. therein). Note, however, that these reports are based on extrapolations into the corona of remote field measurements at the level of photosphere. In situ detection of magnetic nulls has been reported in Earth's magnetosphere [25–27]. The 3D nature of reconnection in magnetosphere is further discussed in Section 1.3.3.

1.3.2 3D Reconnection Basics

As was described in the previous section, intuitive notions about reconnection in 2D may not be true in full 3D. This motivates establishing a rigorous definition for magnetic reconnection as a change in magnetic connectivity of plasma elements. Then a necessary and sufficient requirement of reconnection is for

$$\int E_{||} ds \neq 0 \tag{1.19}$$

to be true for any measurable set of field lines [28, 29] where the integral is taken along field lines.

In general, reconnection occurs according to the following scenario:

1. Initially, plasma and magnetic field dynamics are ideal. Magnetic flux through each plasma element and magnetic connectivity between any two plasma elements do not change in time. The system might contain current sheets.

2. Due to an external driver or a perturbation system enters a state where ideal dynamics are not possible in some region in space (diffusion region). It might be either because it would lead to singular flows (e.g. $\mathbf{E} \times \mathbf{B}$ drift at magnetic nulls) or because of plasma becoming non-ideal in some localized region (e.g. gaining significant resistivity). Either way, ideal plasma dynamics are no longer compatible with the existing magnetic topology and magnetic reconnection happens.

If in 2D reconnection is exclusive to a region around an X-point with geometry as in Fig. 1-2 (with or without guide field) then in 3D several different reconnection geometries are possible [30, 31]:

- Non-null reconnection in geometries with no magnetic field nulls,
- Null point reconnection,
- Separator reconnection.

These geometries and the corresponding reconnection regimes are discussed in detail below.

Non-null reconnection

Non-null reconnection occurs when a diffusion region exists unrelated to magnetic nulls. A possible setup is shown in Fig. 1-6 reproduced from [31]. Plasma is assumed to have finite resistivity in a localized diffusion region around the origin. If plasma and the entrained field lines are driven to cross this region then the non-ideal dynamics in the diffusion region, disparate from the ideal driving dynamics outside of the diffusion region, lead to a change of connectivity between plasma elements.

Null point reconnection

Another possible location for non-ideal flow is at magnetic null points. The general geometry and terminology used is shown in Fig. 1-7 (a). Each null has two groups of field lines asymptotically connected to it. One group consists of two separate

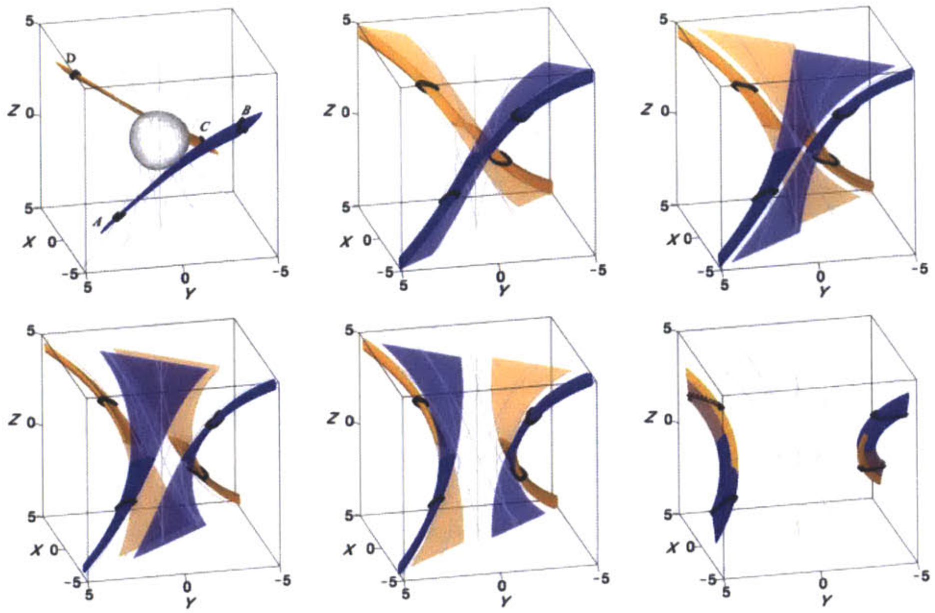

Figure 1-6: Possible setup for non-null reconnection in 3D. Two sets of field lines in orange and blue are followed in time as they encounter a diffusion region (shaded surface). Reproduced from [31].

field lines either both approaching or receding from the null on opposite sides. The neighboring field lines, however, do not cross the null. These two field lines together are called the spine of the given null. Second group of field lines, that are connected to the null, locally form a plane called the fan plane separating the space into two distinct regions. Hence, field lines in the fan are separatrices and the fan itself is a separatrix surface.

Fig. 1-7 (b) shows how the fans of two null points can intersect. In such case there is a field line called the separator connecting the two nulls at the intersection of the fans.

For a single null, three reconnection regimes can be distinguished based on the driving perturbation and the resulting induced current sheet:

- Torsional spine reconnection,
- Torsional fan reconnection,
- Spine-fan reconnection.

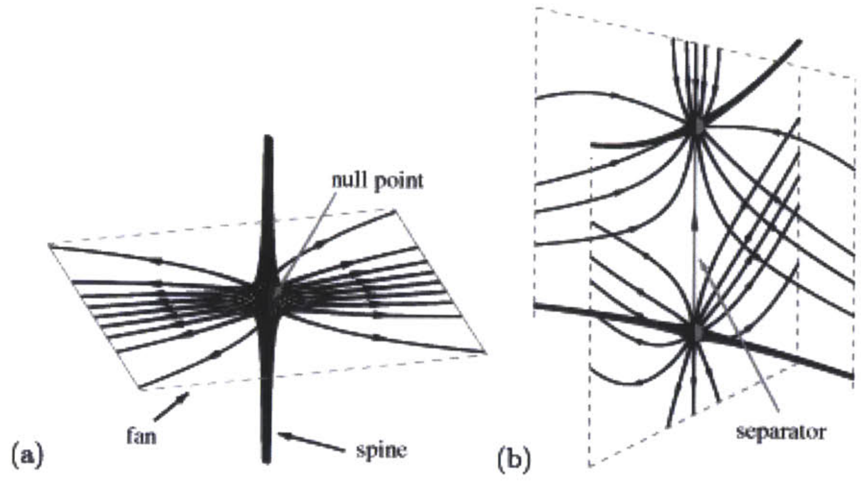

Figure 1-7: Geometry and terminology of magnetic field nulls in 3D. (a) Field lines connected to the null consist of two spine field lines and a surface of separatrix field lines (fan). (b) When fans of two nulls intersect a field line (separator) connects the two nulls. Reproduced from [31].

Torsional spine reconnection Reconnection in torsional spine regime is driven by a rotational perturbation of the fan plane and the nearby field lines. As shown in Fig. 1-8 (a), this perturbation twists field lines around the spine and induces current along the spine (solid black arrow). Plasma connectivity changes within this current as shown in (b) where two sections of originally (at t_0) same field line outside of the diffusion region (grey) are followed in time.

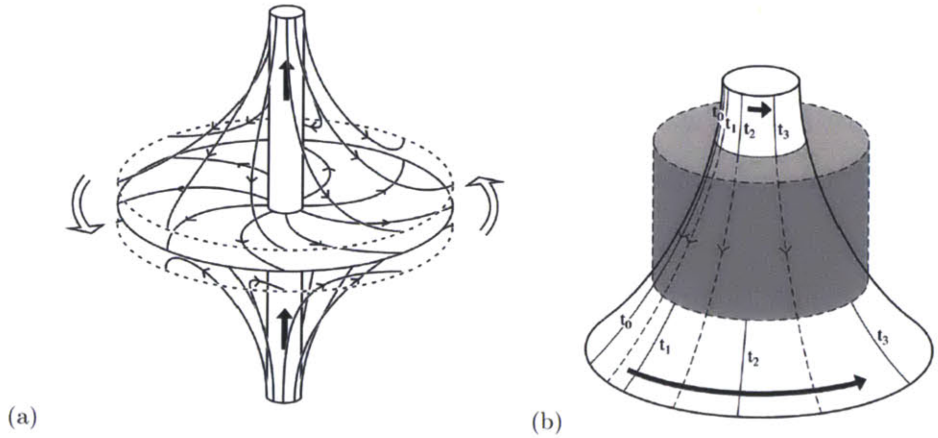

Figure 1-8: Torsional spine reconnection. (a) Rotational perturbation of the fan plane twists field lines around the spine and induces current along the spine (solid black arrow). (b) Resulting change in time in plasma connectivity between field line sections outside of the diffusion region (gray). Reproduced from [30].

Torsional fan reconnection Here reconnection is driven by a rotational perturbation of the spine and the nearby field lines (Fig. 1-9). This results in twisting of field lines near the fan plane and induces a rotational current layer coplanar to the fan (solid black arrows.

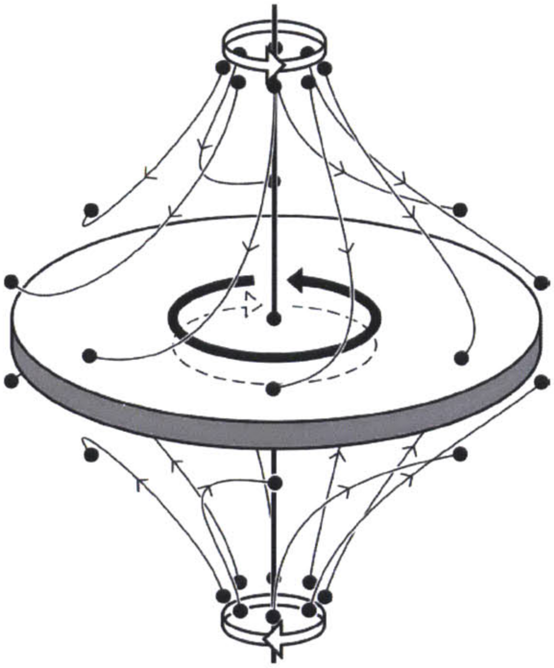

Figure 1-9: Torsional fan reconnection. Rotational perturbation of the spine twists the field lines in the fan plane and induces a rotational current layer coplanar to the fan. Reproduced from [30].

Spine-fan reconnection Unlike the torsional reconnection regimes induced by a rotational perturbation, spine-fan reconnection is driven by a shear disturbance of either spine or fan (or both) (Fig. 1-10). The disturbance breaks the rotational symmetry of the initial null geometry and defines a plane. In this plane the spine and the fan form a Y-type structure containing a diffusion region (gray) and an out-of-plane current sheet (solid black arrows). Outside of the diffusion region plasma and flux is transported across both the spine and the fan (empty arrows).

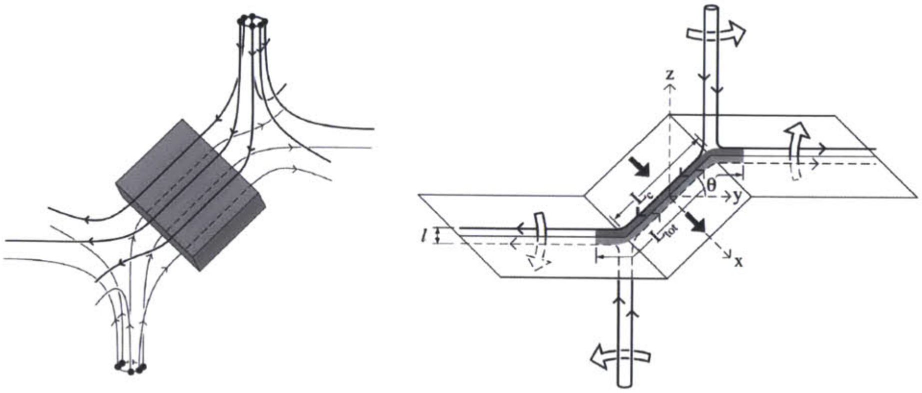

(a)

(b)

Figure 1-10: Spine-fan reconnection. Shear disturbance of either spine or fan (or both) leads to a Y-type structure containing a diffusion region (gray) and an out-of-plane current sheet (solid black arrows). Outside of the diffusion region plasma and flux is transported across both the spine and the fan (empty arrows). Reproduced from [30].

Separator reconnection

The above non-null and null point reconnection regimes assumed presence of at most a single null point and conceivably are the most basic reconnection setups in 3D. However, observations and models suggest that the more complex configuration involving a separator between two magnetic null points be considered as a prominent reconnection location. This topic is focus of ongoing research. Magnetic topologies illustrating this regime are shown in Fig. 1-11. There (a) and (b) setups differ in the magnitude of current along the separator. Note that the projections of field lines in the $Z = 0$ plane are hyperbolic in (a) and elliptic in (b). The possibility of elliptic field line projections around a reconnection site provides strong support to the claim that reconnection in 3D cannot be interpreted as a simple extension of 2D models.

The above basics provide a framework to investigate particular occurrences of reconnection. In particular, below we review basic models of 3D reconnection in Earth's magnetosphere. The rest of this thesis focuses on research in a laboratory setting.

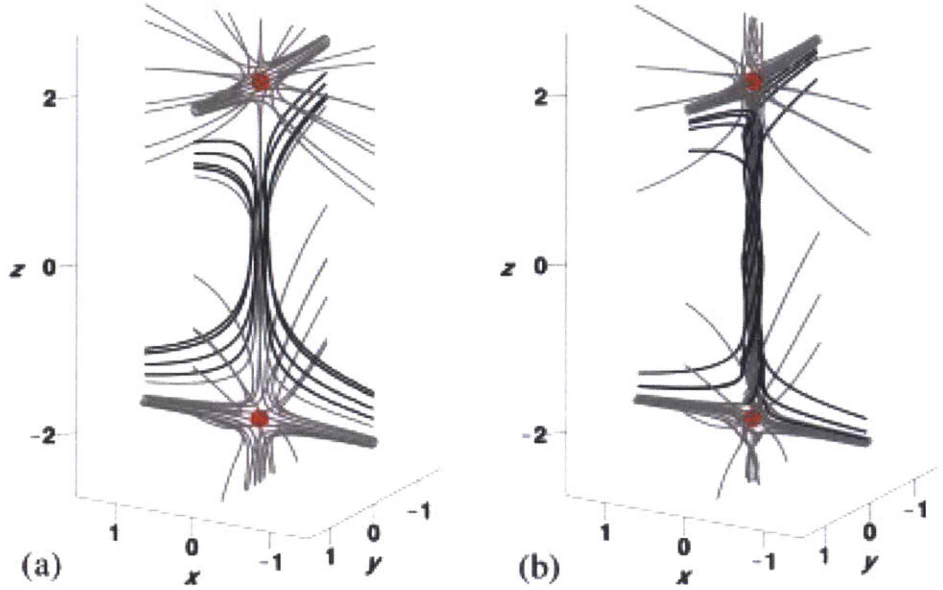

Figure 1-11: Magnetic field lines in two separator reconnection setups differing in the magnitude of current along the separator. Of consequence, projections of field lines in the Z = 0 plane are hyperbolic in (a) and elliptic in (b). Reproduced from [31].

1.3.3 3D Reconnection in Magnetosphere

Examples of 3D reconnection in nature include occurrence in the Earth magnetosphere. Research of magnetospheric reconnection there is valuable, first, because of potential consequences of reconnection related magnetospheric events for civilization and, second, because the magnetosphere provides unique opportunities to make in situ reconnection measurements using spacecraft that are not possible in other settings (astrophysical or laboratory) due to scale sizes or inaccessibility by instruments.

A reconnecting magnetosphere model was first proposed by Dungey et al. [11, 32], extended beyond antiparallel fields by Cowley [33], and tested in resistive MHD simulations by Dorelli et al. [34]. In an approach similar to ours in this thesis and dictated by the complexity of the problem, they first investigated the topology of a vacuum model magnetic field. This allows one to identify potential locations and regimes for reconnection to occur. The field consists of a superposition of a uniform straight IMF together with a possibly tilted Earth's dipole field. By definition, the actual topology changes once reconnection is allowed.

We focus on cases where the IMF projection along the dipole is positive (northward

IMF). In the special case of IMF and dipole perfectly parallel the field line geometry is rotationally symmetric about the dipole axis (Fig. 1-12). Two null points are formed (red and blue spheres, Earth is the purple sphere in the center) connected by a spine (not shown) through Earth. Separatrices from the two null points connect to form a closed surface. All field lines inside the sphere, except for the spine, are closed (blue lines). All field lines outside of the sphere are external and never connect to Earth (red lines). Since the two separatrix surfaces coincide then every field line on the separatrix surface is also a separator. Thus, there are infinitely many separators.

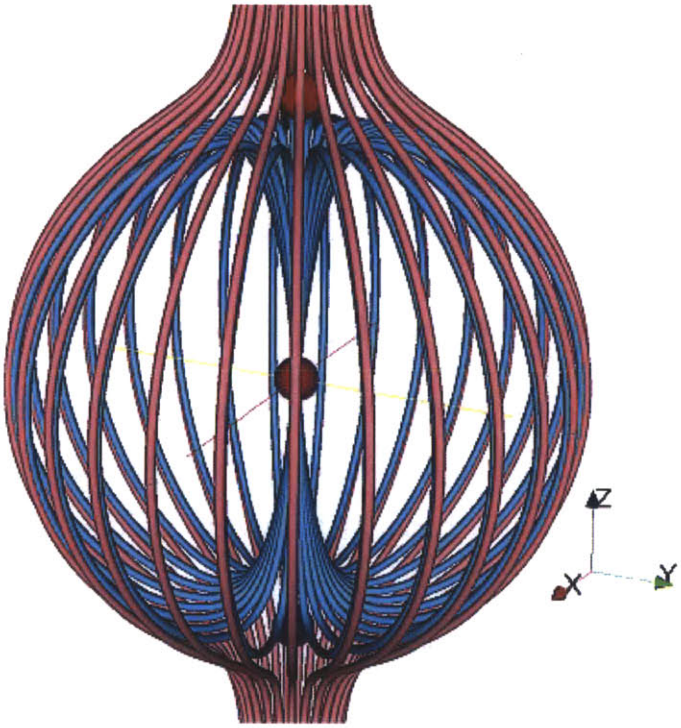

Figure 1-12: Magnetosphere vacuum model fields for the special case of IMF and dipole perfectly parallel. Shown are the resulting two null points (red and blue spheres), Earth (purple sphere in the center), closed and open field lines (blue and red respectively). Reproduced from [34].

The topology changes radically for even the slightest tilt of IMF with respect to the dipole. While there are still two null points, the symmetry is broken and the corresponding separatrix surfaces no longer overlap. Instead, the two surfaces intersect at two separators (yellow) forming a single loop. This is illustrated in Fig. 1-13 for a 45° tilt where field lines are traced starting with points near each of the two nulls. In addition to closed field lines inside the separatrix surfaces and external field lines flowing completely around the structure and never connecting to Earth (not shown), there are now open field lines that connect to Earth at one end and are open at the other end.

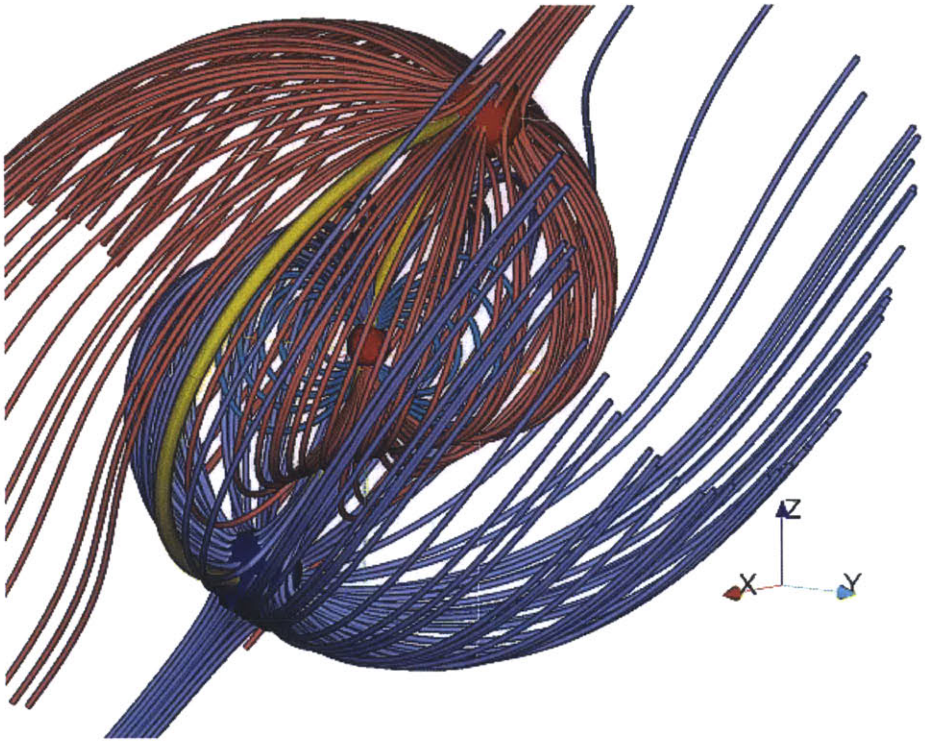

Figure 1-13: Magnetosphere vacuum model fields for a 45° tilt between IMF and the dipole. Shown are the two resulting null points (red and blue spheres), Earth (purple sphere in the center), and field lines traced starting with points near each of the two nulls. Reproduced from [34].

It was proposed already by Cowley [33] that separator reconnection could occur in this setup. The numerical resistive MHD experiments by Dorelli et al. [34] suggest that diffusion region includes but is not limited to the separator. They also discovered that each of the two null geometries can split up into several nulls and rejoin again. However, even with several nulls locally instead of a single null, the global topology remains largely unaffected by this splitting and is equivalent to the two null global topology already discussed.

Another important conclusion made by Dorelli et al. [34] is that knowledge of local magnetic field topology as, for example, determined from spacecraft data, may not be sufficient to analyze magnetospheric reconnection phenomena since it does not reveal the complete picture of the complex magnetic interconnections. Thus spacecraft observations and numerical simulations should be complemented with well diagnosed laboratory experiments that can capture both local reconnection phenomena and the global magnetic topology.

1.3.4 Experimental investigations

In the lab, 3D null point configurations relevant to our research have been observed experimentally by Stenzel et al. when pulsing current through a Helmholtz coil [35]. An initial rise in the current establishes a field-reversed configuration (FRC) with two 3D nulls and drives these nulls axially apart. However, no reconnection was observed at the nulls. After all, the driven flux expansion is unimpeded. The measured time evolution of flux surfaces is shown in Fig. 1-14.

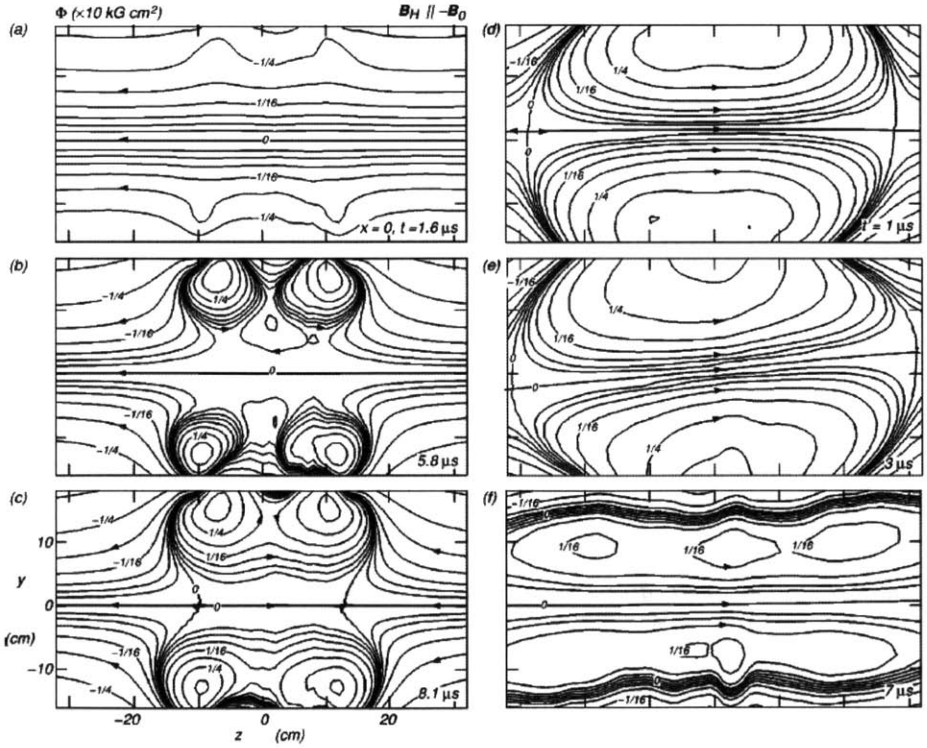

Figure 1-14: Time evolution of flux surfaces in the FRC experiments by Stenzel et al. Two 3D nulls are formed and driven apart with no reconnection observed at the nulls. Reproduced from [35].

3D reconnection at nulls has been observed at the Swarthmore Spheromak Experiment (SSX) and within the complementary computational study using the HiFi multi-fluid modeling framework [36, 37]. There reconnection occurs at a null point between two spheromaks of the same handedness during relaxation and merging towards the minimum energy state. Authors observe correlated rapid motion of the magnetic null and the reconnection region.

In the non-null regime 3D reconnection has been experimentally observed as a result of interaction between two flux ropes in linear devices [38, 39].

1.4 Thesis Objectives and Outline

The objective of this thesis is experimental study of magnetic reconnection in 3D geometries in a dedicated setup in the Versatile Toroidal Facility (VTF). Achieving this objective required developing of the setup (including a suite of diagnostics and a plasma source), characterizing the plasma, and theoretically investigating the geometries. We then measured the plasma parameters and dynamics to determine the presence, character, and effects of reconnection in these geometries.

This thesis is organized as follows:

- Chapter 1 has introduced the magnetic reconnection phenomenon and has presented the present state of knowledge as well as the unresolved issues thus providing motivation for this work,
- Chapters 2 and 3 together introduce the experimental setup for this research with Chapter 3 dedicated to the plasma source (washer plasma gun),
- In Chapter 4 we present in detail the magnetic field configurations theoretically expected in our experiments,
- Chapter 5 presents observations of plasma beam oscillations in our setup. While these oscillations are not directly related to magnetic reconnection, they must be understood since they are observed in addition to any reconnection phenomena,

- Chapters 6 and 7 then discuss the experimental observations of magnetic reconnection in, respectively, the normal and tilted configurations introduced in Chapter 4,

- Finally, Chapter 8 provides an overview, draws conclusions, and suggests future work.

Chapter 2

Experimental Setup

2.1 The Versatile Toroidal Facility

We performed experimental research at the Versatile Toroidal Facility (VTF) (see Fig. 2-1 and [40]) at the MIT Plasma Science and Fusion Center. As the name suggests, the defining features of the facility are that it consists of a toroidal vacuum chamber and that it can be fitted for research in a variety of basic plasma physics areas. Previous experiments have focused on magnetic reconnection in nominally toroidally symmetric 2D collisionless regimes [41–45], but important results have also been achieved in such research areas as plasma filament propagation [46].

The vacuum chamber is made of 304-L stainless steel. It is toroidal with the major radius of 95 cm and a rectangular cross section of 65-by-107 cm. 16 horizontal and a total of 32 vertical ports on top and bottom of the machine provide access for diagnostics. A particular cross section together with the two coordinate systems used is shown in Fig. 2-2. One coordinate system is cylindrical and is based on the rotational symmetry of the torus around its center axis (blue). The other system (green) is Cartesian with Z-axis parallel to the axis of rotation for the support of our magnetic null coil (red, see Section 2.2.1). Rotation of the null coil then is about Z-axis of the Cartesian coordinate system. X-axis lies in the R-Z plane of the cylindrical coordinate system and Y-axis then is aligned with the local φ direction. The Cartesian Z-axis also lies in the R-Z plane of the cylindrical coordinate system

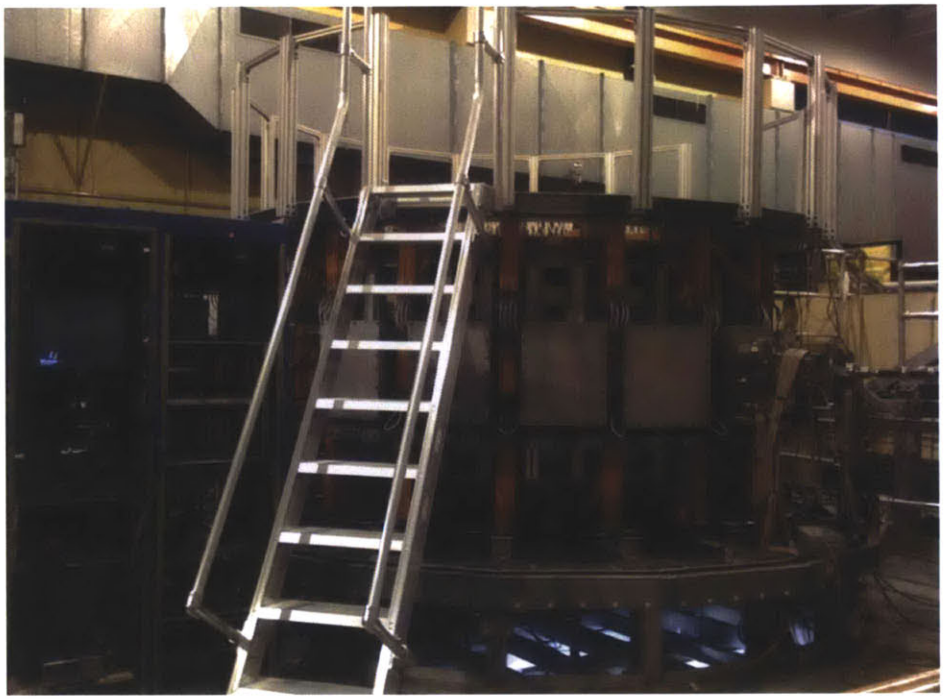

Figure 2-1: A photograph of VTF. Note the horizontal ports, stairs to the top of the machine where half of the vertical ports are located (the other half are on the bottom of the machine), orange toroidal magnetic field coils, and some of the computers and electronics for data acquisition.

and is at a 9° tilt with respect to the cylindrical Z-axis.

In addition to these two coordinate systems we use the the standard terminology for toroidal geometries whereby φ direction is called toroidal with the orthogonal R-Z plane termed the poloidal plane. Thus, in Figure 2-3 the blue arrow is in the toroidal direction while the red arrow is in the poloidal plane and is locally orthogonal to the blue arrow.

We used a 600 l/s Leybold turbomolecular pump in combination with a scroll pump to continuously pump the chamber with a resulting base pressure of 3×10^{-6} Torr (monitored using an ionization gauge). A residual gas analyzer allows us to infer the constituents of this base pressure - water vapor and nitrogen. Other general features of VTF include toroidal magnetic field coils (orange in Fig. 2-1) and data acquisition electronics. The toroidal field coils encircle the vacuum chamber through the hollow center and provide magnetic field that within the chamber is purely in the toroidal direction, is uniform for vertical displacements, and decreases as 1/R for

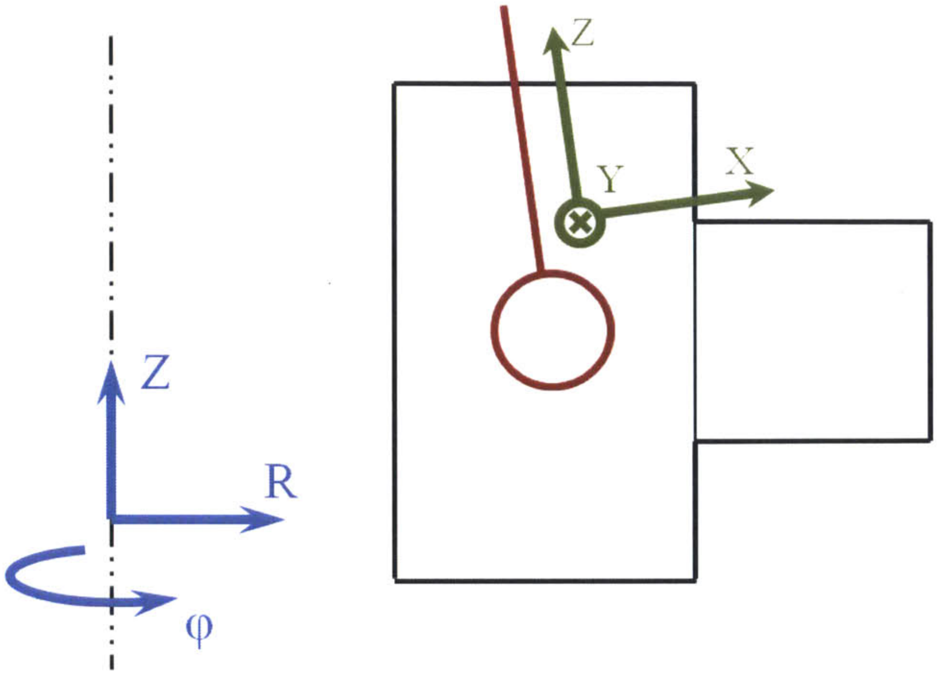

Figure 2-2: Coordinate systems used. One (blue) is cylindrical and aligned with the toroidal chamber (cross section in black). The other (red) is Cartesian and is aligned with the null coil support.

radial displacements. All our experiments were performed with the toroidal field set to 22 mT at R = 1 m.

Data acquisition electronics consists of analogue circuits specific to different diagnostic probes, digitizers, and a network of computers. Starting from a given diagnostic, the signal is fed to analogue circuits and further to ICS645B 2MHz single-ended digitizers sold commercially by the Radstone Corporation (now GE). A network of computers with LabView control software is used to trigger different electronics according to a preprogrammed timing scheme and also to store the data from the digitizers.

2.2 Setup for 3D Reconnection Experiments

The basic goal of our research was to investigate magnetic reconnection in 3D geometries. In particular, we wanted to drive reconnection near 3D magnetic nulls and observe the resulting plasma dynamics. A cartoon illustration of the basic setup is

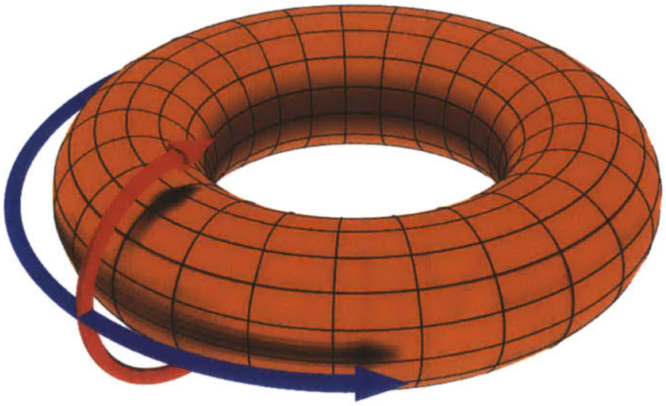

Figure 2-3: Toroidal (blue) and poloidal (red) directions in a toroidal geometry. Reproduced from [47].

presented in Fig. 2-4. We use the plasma gun described in Chapter 3 to create plasma for our experiments. We apply bias voltage to the accompanying anode bias plate located away from the gun further along the background toroidal field $\mathbf{B}_{tor}$. The resulting applied electric field drives plasma current $\mathbf{J}$ which further ionizes background neutral gas and heats the plasma. We then pulse current through a coil - the null coil (see Section 2.2.1) - such that the resulting dipole magnetic field of the coil $\mathbf{B}_{coil}$ is opposite to the background field $\mathbf{B}_{tor}$. The two points where the fields are exactly of the same magnitude but in the opposite directions are magnetic null points. Details of the technical aspects follow while Chapter 4 is dedicated to the expected magnetic field configurations.

The overall VTF geometry is toroidal rather than linear hence the actual implementation is as shown schematically in Fig. 2-5 in a view from top. Plasma beam follows the curved toroidal field between the gun and the bias plate, which are separated by 120 degrees along the toroidal direction equivalent to 2 m in path length.

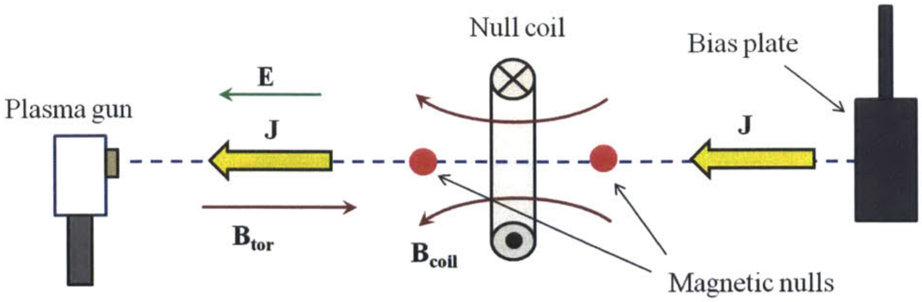

Figure 2-4: Basic experimental setup. Plasma gun and a bias plate are used to create plasma and source plasma current along the background magnetic field. Then we pulse current in the null coil creating field opposite to the background toroidal field and driving formation of two magnetic null points.

2.2.1 Null Coil

The null coil consists of 12 turns of 6 AWG magnet wire tightly wound into a circular shape of mean radius of 12.8 cm. The complete coil is glued together with fiberglass and epoxy to ensure rigidity and provide additional electrical insulation. The coil is nominally located in a poloidal plane at a point in between the plasma gun and the bias plate as shown in Fig. 2-5. The coil can be rotated around its support axis or tilted together with the support in the local φ direction. Correspondingly, this effectively results in rotating the null coil out of the poloidal plane either about axis roughly parallel to the cylindrical Z-axis or about the local cylindrical R-direction. In addition, the coil can be displaced within the poloidal plane when nominally it is centered on the plasma beam.

Fig. 2-6 is a photograph taken during a vacuum break of the coil mounted inside the vacuum chamber. Also labeled and described in other sections are the plasma gun further away toroidally (Section 3), Langmuir, Rogowski, and magnetic coil probe arrays mounted on the null coil (Section 2.4), and a mirror for camera mounted on a vertical port on top of the machine (Section 2.4.4). The pipe setup consisting of an aluminum pipe and a Teflon shield was not used in the particular experiments described in this thesis.

The current in the null coil is pulsed using a circuit consisting of two capacitors $C_1 = 1.2$ mF, $C_2 = 0.1$ mF, an ignitron switch, the null coil, and control electronics

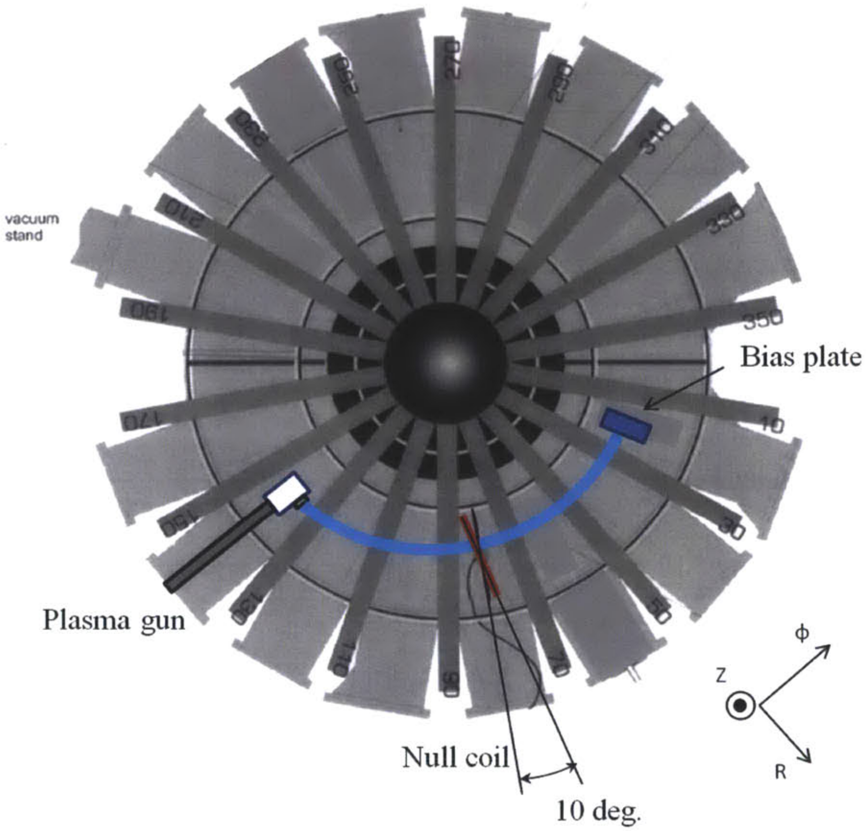

Figure 2-5: View from the top of the basic setup in the toroidal VTF geometry. Plasma beam follows a curved toroidal field line. The null coil is located between the gun and the anode plate and can be rotated. Modified figure from [40].

for charging and firing. The basic circuit is shown in Fig. 2-7. We start with C_1 charged to 2 kV. During a given single experimental run ("shot"), the ignitron is fired at a prescribed time which commences the discharge of C_1 through the null coil. This leads to an eventual polarity change to opposite for C_1 and now a charged state of C_2. The ignitron switch is not fired after the initial trigger and interrupts any further current flowing to C_1. Thus, after the the first oscillation half-cycle, C_1 remains charged while oscillations continue in the RLC loop formed by C_2 and the null coil. We implemented this setup to establish current oscillations in the null coil while firing the ignitron, which produces noise in probe electronics, only once rather than as part of every oscillation cycle. Current in a null coil turn as well as the

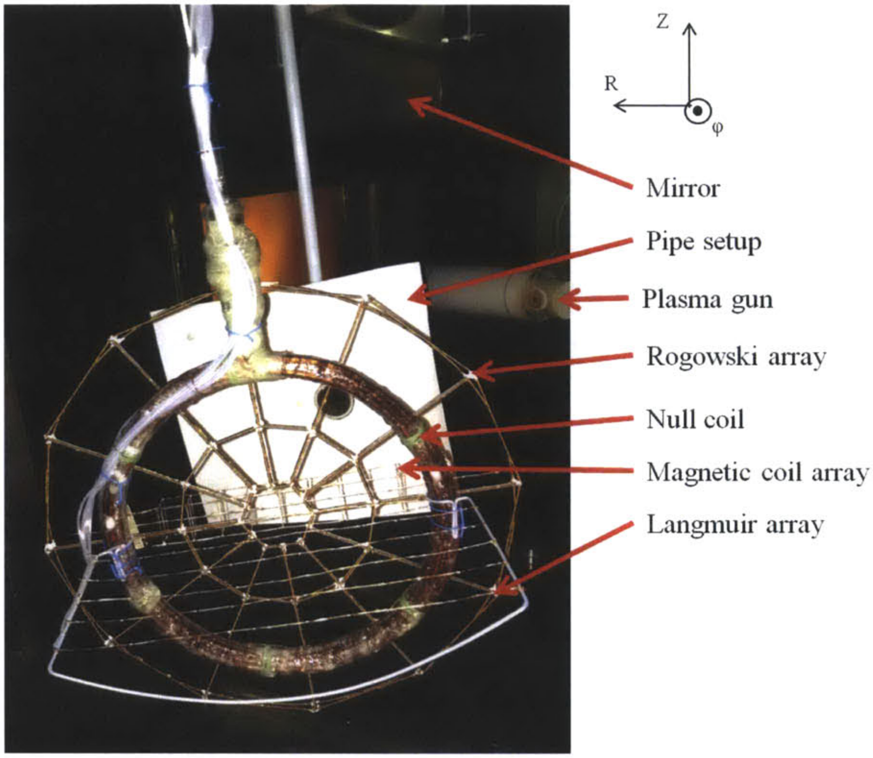

Figure 2-6: A photograph of the null coil mounted inside the vacuum chamber with probe arrays attached. Also seen are the plasma gun and a mirror used for the camera. The pipe setup was not used in the experiments described in this thesis.

corresponding expected total magnetic field at the center of the coil from all 12 turns are plotted as a function of time in Fig. 2-8 top panel. Note the decrease in oscillation amplitude after the first half-cycle when the ignitron switch disconnects C_1 from the null coil oscillation circuit.

To refer to different phases of the experiment we will use the following terminology:

- Compression phase - the time intervals when the null coil current is positive. Field radially inside the coil is enhanced and the plasma beam gets compressed,
- Null phase - the time intervals when the null coil current is negative and of large enough magnitude that two null points are formed. The total field at the center of the coil is opposite to the background field,
- X-line phase - the time intervals when the null coil current is negative but not of large enough magnitude that a null point would form. Instead, a circular

X-line radially inside the null coil separates the closed field lines encircling the null coil and the open field lines of the background field. The total field at the center of the coil is in the same direction as the background field, only decreased in magnitude,

- Coil field increasing (decreasing) - the time intervals when the magnitude of the null coil current and the resulting null coil magnetic field is increasing (decreasing).

The above magnetic field configurations are described in more detail in Chapter 4.

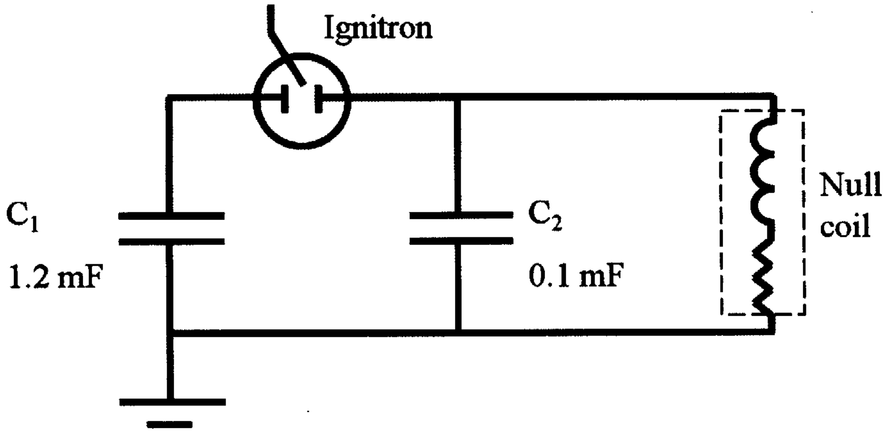

Figure 2-7: Circuit for pulsing the null coil. Ignitron is fired once to discharge C_1 and establish current oscillations in the RLC circuit formed by C_2 and the null coil.

2.2.2 Experimental Procedure

Our experiments were performed according to the timing scheme listed in Table 2.1. As part of this schedule we fire the gun for 7 ms and start the null coil current pulse with the gun already firing. The application of gun bias at 6.5 ms, as described in Chapter 3, further ionizes and heats plasma while driving current along the plasma filament. The gun anode bias current waveform is shown in Fig. 2-8 (bottom). The relative timing of the null coil and gun bias current pulses results in three null coil current oscillations between 7.4 and 9.1 ms during the relative flattop phase of the bias current of $I_{bias} \sim 0.22$ kA. At 12 ms we stop the plasma gun discharge by shorting

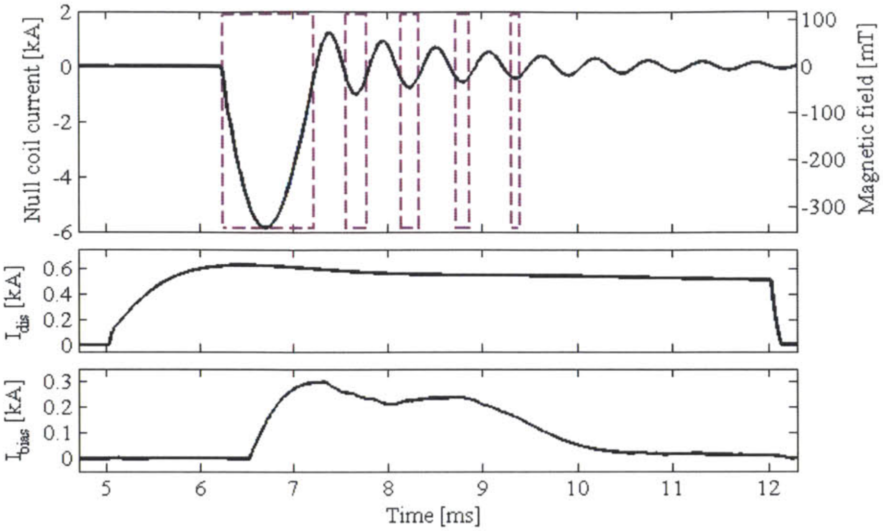

Figure 2-8: Top: current in a null coil turn and the corresponding expected total magnetic field at the center of the coil from all 12 turns as a function of time. Dashed magenta line marks the null phases. Middle: gun discharge current. Bottom: gun anode bias current.

the applied gun voltage using a crowbar circuit. We allow for at least 3 minutes for chamber pump-down after the shot and recharging of capacitor banks before taking another plasma shot.

Time [ms]	Action
0	Trigger digitizers to start recording data
5.0	Fire plasma gun
6.2	Pulse null coil
6.5	Apply gun bias
12.0	Short plasma gun

Table 2.1: Timing schedule for the experiments performed

2.3 Parameters

We use measurements and educated estimates to evaluate the typical plasma parameters in our experiments. Values are listed in Table 2.2.

An immediate conclusion from the plasma parameters is that VTF plasmas are not only short-lived, but also sufficiently tenuous and low-temperature that probes

Density	n	$1 \cdot 10^{18}$ m^{-3}
Temperatures	$k_B T_e$	20 eV
	$k_B T_i$	≤ 1 eV
Magnetic field	B	10 mT
Plasma beta	β	0.08
Plasma frequencies	ω_{pe}	$2\pi \times 9$ GHz
	ω_{pi}	$2\pi \times 30$ MHz
Gyrofrequencies	ω_{ce}	$2\pi \times 300$ MHz
	ω_{ci}	$2\pi \times 4$ kHz
Electron thermal speed	$v_{th,e}$	$3 \cdot 10^6$ m/s
Ion sound speed	c_s	$7 \cdot 10^3$ m/s
Alfvén speed	v_A	$3 \cdot 10^4$ m/s
Gyroradii	$r_{L,e}$	2 mm
	$r_{L,i}$	10 cm
Inertial lengths	d_e	5 mm
	d_i	1 m
Debye length	λ_D	$3 \cdot 10^{-5}$ m
Spitzer resistivity	η_{SP}	$4 \cdot 10^{-6}$ $\Omega \cdot$ m
Electron-ion mean free path	λ_{ei}	13 m
Lundquist number	S	$1 \cdot 10^3$

Table 2.2: Typical plasma parameters in our experiments

can be used throughout the plasma volume as described in the next section.

2.4 Diagnostics

In our choice of diagnostics we were guided by plasma parameters we would like to observe in order to answer the scientific questions posed while also considering the practical limitations of experimental research. In particular, our selection of methods was influenced by the following factors:

- How reproducible are plasma shots? Is it accurate and/or necessary to measure a given parameter during a single shot, to use averages of several shots, or to assemble a data set from several controllably varied shots?

- How feasible and/or necessary is it to build and use an array of probes? What is the trade-off between more data accumulated within a single shot and the complexity of the array and the requirement for additional electronics?

- Do the probes significantly perturb plasma and affect the phenomena investigated?
- What is the previous experience accumulated and resources already available within our research group?

Ultimately, we used a combination of Rogowski, Langmuir, and magnetic coil probes individually and in arrays with data collected over numerous shots both as averages and as part of controlled scans. In addition, fast camera visible light images were available shortly after each shot, required no further data processing, and provided valuable feedback and guidance during the run campaigns. In the following subsections we describe in detail these different diagnostics.

2.4.1 Rogowski Probes

It can be seen from, for example, the generalized Ohm's Law (Eq. 1.1) that current density is an essential parameter in understanding the magnetic topology and plasma dynamics of reconnection. Thus, location and extent of current sheets is important in all of 2D and 3D reconnection models. Consequently, it is one of the goals of this thesis to determine the plasma current structure of the 3D reconnection topologies in our experiments. To address this goal we deployed a set of Rogowski probes that measure the change in time of the current crossing the probe plane. After integration one then obtains an estimate for the spatially averaged current density across the probe plane as a function of time.

The basic principles of a Rogowski probe are illustrated in Fig. 2-9 (left, based on [48]). Each probe consists of a wire wound into a coil with a cross section area A_1. The coil together with the return lead is bent into a closed contour of area A_2 and circumference L. Changing current $\frac{dI}{dt}$ through A_2, according to Ampere's law, induces changing magnetic field along the contour circumference (black arrow), which, in turn, leads to a changing magnetic flux across the coil cross section area A_1. Faraday's law then predicts induced voltage along each of the N coil loops with the total voltage U appearing across the probe leads. Mathematically:

$$U = \mu_0 \frac{N}{L} A_1 \frac{dI}{dt}, \tag{2.1}$$

where μ_0 is permeability of free space.

We built an array of Rogowski coils consisting of a total of 37 constituent coils in four basic shapes arranged into three concentric bands as shown in Fig. 2-9 (right). The diameter of the boundary between the 2nd and 3rd bands is 26 cm corresponding to the null coil radius. Thus, when the array is mounted on top of the null coil as can be seen in Fig. 2-6, we measure the plasma current crossing the null coil plane both radially inside and within a band outside of the null coil. Each constituent coil is constructed by winding a 6 mil HML-coated copper wire in a single tight layer around a 1/16 in. diameter Garolite plastic rod. We measure the coil resistances to be 20 - 25 ohms and estimate the inductances of less than 30 μH and the capacitances of less than 4 nF.

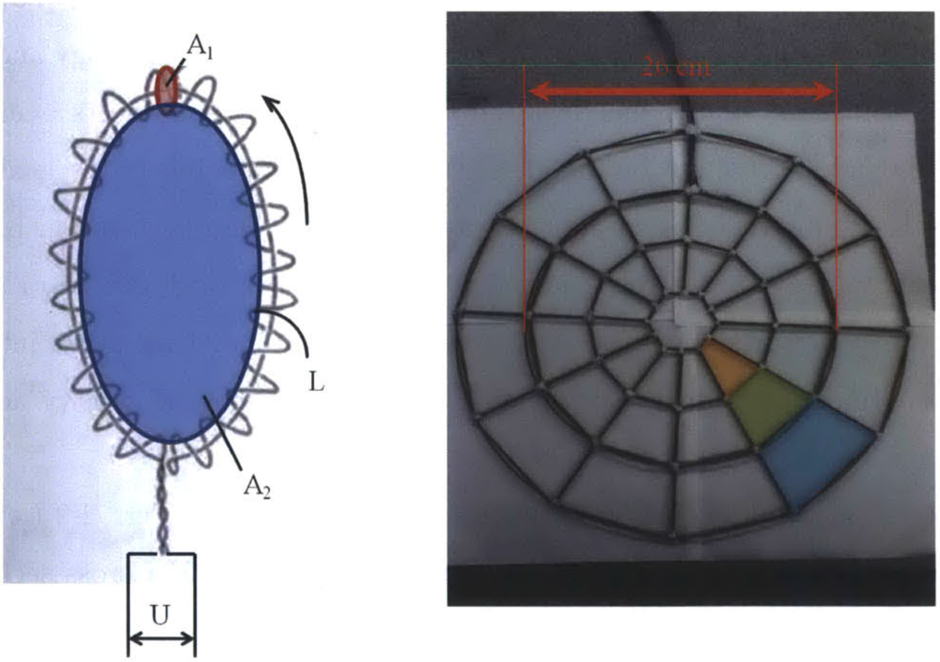

Figure 2-9: Left: basic principles of a Rogowski probe. Changing current through A_2 induces changing flux through A_1, which in turn produces voltage U between the lead. Right: photograph of the Rogowski probe array with three of the constituent coils shaded.

In addition to measuring the induced electric field due to changing current each coil is also capacitively coupled to plasma. Changing plasma potential then also produces voltage signal on the probe leads. Presumably, this signal is a common-mode signal which we reduce using analogue differential amplifiers. The basics of the effective circuit are shown in Fig. 2-10.

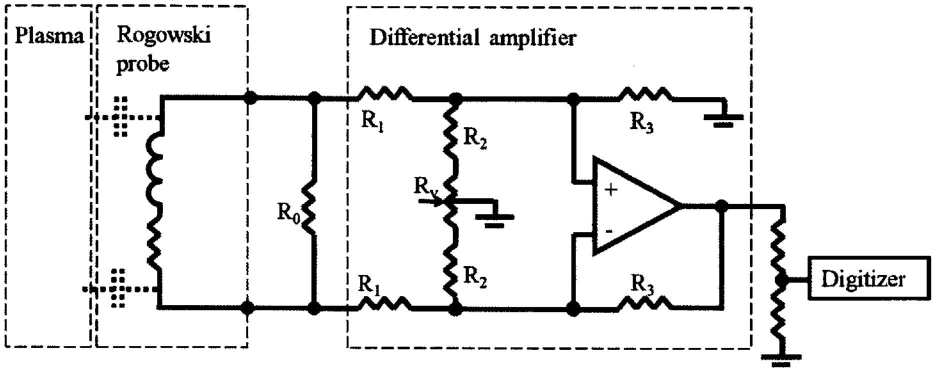

Figure 2-10: The basics of the effective circuit for the Rogowski probes. Each coil is connected to a differential amplifier circuit calibrated for optimal common-mode rejection. The amplifier output signal is then supplied to the digitizer.

The main component is a differential amplifier circuit with the differential mode gain given by R_3/R_1 with R_3 = 20 kΩ and R_1 = 1 kΩ. The complete circuit with additional details not shown is calibrated for optimal common-mode rejection at 10 kHz using a function generator and an oscilloscope. Within the presented circuit, the common-mode rejection is adjusted by trimming the R_v variable resistor to offset any actual differences in the nominally equivalent resistors R_2 = 100 Ω connected to the two inputs of the amplifier.

In addition, we use a R_0 = 10 Ω resistor in parallel to the amplifier circuit input port to reduce the differential mode signal applied to the amplifier. On the output side, a voltage divider reduces the processed signal supplied to the digitizer. It should be noted that the small value of R_0 implies that the coil impedance $i\omega L$ with $L \leq 30$ μH is of comparable magnitude already for f = 50 kHz and higher.

With the Rogowski probe array mounted on top of the null coil, probes pick up significant signals from the current flowing in the null coil. This is a damped sinusoidal signal with a period of ~0.6 ms (see Fig. 2-8 for the null coil current). In addition, we observe a drift in the measured current on the longer experimental time scales of ∼5 ms with contribution from pick-up from gun firing and from a drift in the differential amplifier ground. These low frequency drifts do not allow us to accurately measure the absolute value of plasma current through the given probe's plane. However, the higher frequency plasma current oscillations of characteristic frequency ∼20 kHz discussed in more detailed in Chapter 5 should be measured accurately. In particular, we use the following protocol in processing the integrated Rogowski probe array signals:

1. Subtract a combination of the null coil current, a constant offset, and a constant slope waveform least-squares fits,
2. Subtract the low frequency background obtained using moving average Gaussian smoothing of width 0.05 ms.

In addition to the Rogowski probes in the array, we used several separate Rogowski probes to measure relevant currents in the experiment. For example, the waveforms for the null coil current and the gun anode bias in Fig. 2-8 were obtained using the separate Rogowski probes. The coils in these probes were also each connected to a circuit as in Fig. 2-10 with resistor values chosen for the particular current amplitudes measured. Of course, one does not have to worry about capacitive coupling to plasma for probes that are used on cables outside the vacuum chamber.

We calibrated some of the separate coils directly by discharging capacitors of known capacities through cables threaded through the coils. Knowing the capacity and the initial voltage one can absolutely calibrate the integrated current waveform to the total initial charge of the capacitor. Then, for the remaining separate coils and the Rogowski probe array, we matched the measurements to those of calibrated coils for times when we expect the currents to coincide.

2.4.2 Magnetic Coil Array

We complement the direct current measurements from Rogowski coils with magnetic field measurements from a magnetic coil array which, through Ampere's law, also provide information about the plasma currents. The basic principles of a magnetic coil are illustrated in Fig. 2-11 (left, reproduced from [48]). Each probe consists of n turns of wire wound into a coil. In accordance with Faraday's law, magnetic field B changing in time induces electric field along the wire which can be measured as voltage V across the probe leads. Mathematically:

$$V = -n\left\langle \dot{B} \right\rangle A, \tag{2.2}$$

where A is the probe loop area and $\left\langle \dot{B} \right\rangle$ is the time derivative of the magnetic field averaged over A.

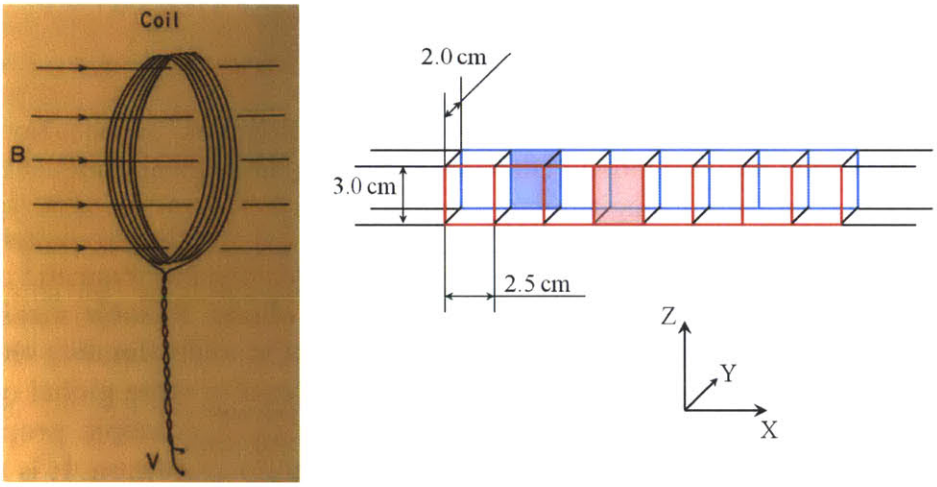

Figure 2-11: Left: basic principles of a magnetic coil. Changing magnetic field B drives voltage V across the probe leads. Right: diagram of the magnetic coil array used. A total of 16 coils are arranged in two rows (red and blue in the figure). Probe loop areas of two coils are shaded.

Our actual implementation of the magnetic coils can be seen in the diagram on the right in Fig. 2-11 and in the photograph in Fig. 2-12. We use a total of 16 coils each consisting of 2 turns in a rectangular shape of 2.5-by-3.0 cm. The coils are arranged in two rows of eight (red and blue in the Fig. 2-11) displaced in the y-direction by 2.0 cm. The whole array is mounted on screws on top of the Rogowski array centered in the z- and x-directions covering area from X = -10 cm to X = +10 cm and from Z = -1.5 cm to Z = +1.5 cm. During a vacuum break we can adjust the y-location of the array along the screws. Thus, the y-coordinate of the coils closer to the null coil can span the range from Y = -6.9 cm to Y = -2.2 cm. For a given location we run and average ten shots.

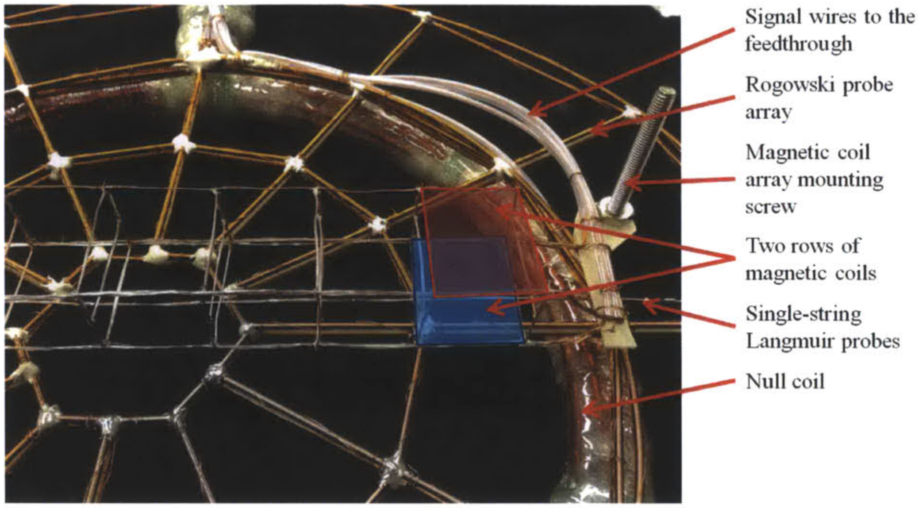
Signal wires to the feedthrough
Rogowski probe array
Magnetic coil array mounting screw
Two rows of magnetic coils
Single-string Langmuir probes
Null coil

Figure 2-12: Magnetic coil array mounted on top of the Rogowski probe array. A magnetic coil from each row is shaded. Distance between the null coil and the magnetic coil array can be adjusted using the mounting screw.

Negligible capacitance between the coils and the plasma allows for simpler electronics compared to the Rogowski probe array avoiding the need for differential amplifiers. Instead, as shown in Fig. 2-13, we measure voltages V_1 and V_2 at the two ends of each probe using two digitizer channels with input resistances of $R_0 = 500\ \Omega$. We use resistors $R_1 = 100\ \Omega$ and $R_2 = 10\ \Omega$ to divide down the voltage applied to the digitizer channels. Each probe has resistance of $R_{coil} \sim 25\ \Omega$.

In our experiments the measured fields are predominantly the magnetic fields due to the current driven in the null coil and are similar to the fields measured in experiments without the plasma ("vacuum shots"). The small difference in the null coil fields is due to the mutual inductance between the null coil and the plasma that results in a small phase shift in the current oscillations in the null coil circuit. Thus, subtracting the vacuum field measurements from the plasma shots leaves not only the sought after signal due to the plasma currents but also an oscillatory signal corresponding to this phase shift in the null coil circuit in plasma shots. Examples of the different components of the measured fields are shown in Fig. 2-14. In the top panel we are presenting the total measured field by two of the magnetic coils.

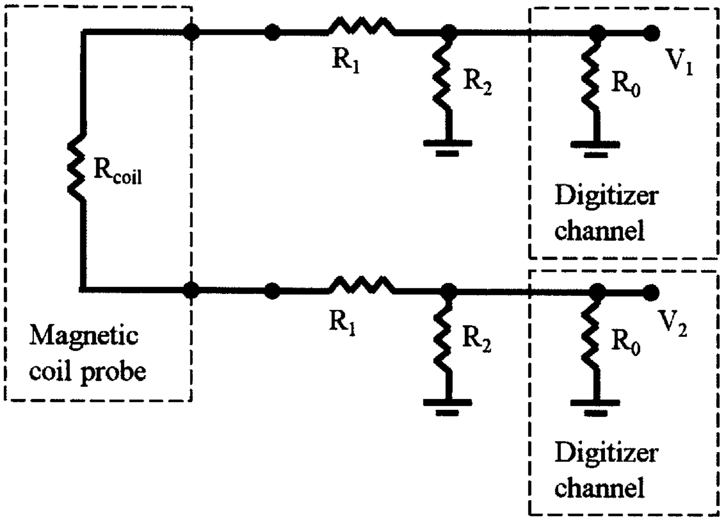

Figure 2-13: Electric circuit for measuring the output voltage of the magnetic coils using digitizers.

Subtracting the vacuum shot measurements produces the fields in the middle panel. Channel 16is presumably distant from the plasma currents and is left with only the component due to the phase shift in the null coil current while channel 4 has also spikes due to the fields produced by currents in the plasma. The bottom panel shows the magnetic field due to the plasma currents alone for channel 4. For all channels we first subtract the vacuum measurement and then obtain the plasma current fields by further fitting and subtracting the channel 4 vacuum field measurement, the channel 16 phase shift component, and a fifth order polynomial fit. The fitting is performed for select time intervals without the plasma current signal.

An example of the magnetic fields due to the plasma current alone for a whole row is shown in Fig. 2-15. Larger plasma fields in the center coils and the symmetry of the signals with respect to the center channels suggests that the plasma currents are predominantly circular in the X-Z plane.

Our magnetic coil array thus provides measurements of the y-component of the magnetic field in the X-Z plane. Reasonable assumptions and mathematical methods allow us to extract further information about the plasma currents sourcing these fields. In particular, we assume that the source currents are circular, parallel to the X-Z plane, and possibly radially displaced along the X-axis. More specifically, we calculated the measured response to a set of a total of 1050 such source current loops located at 21 different Z-coordinates between Z = -0.12 m and Z = +0.12 m with 10 different radii between 0.6 cm and 11.4 cm and with 5 different displacements between -2.4 cm and +2.4 cm along the X-axis. Then for a given point in time we used singular value decomposition (SVD) retaining the 20 largest singular components to express the actual measured signal as produced by a subset of the source current loops.

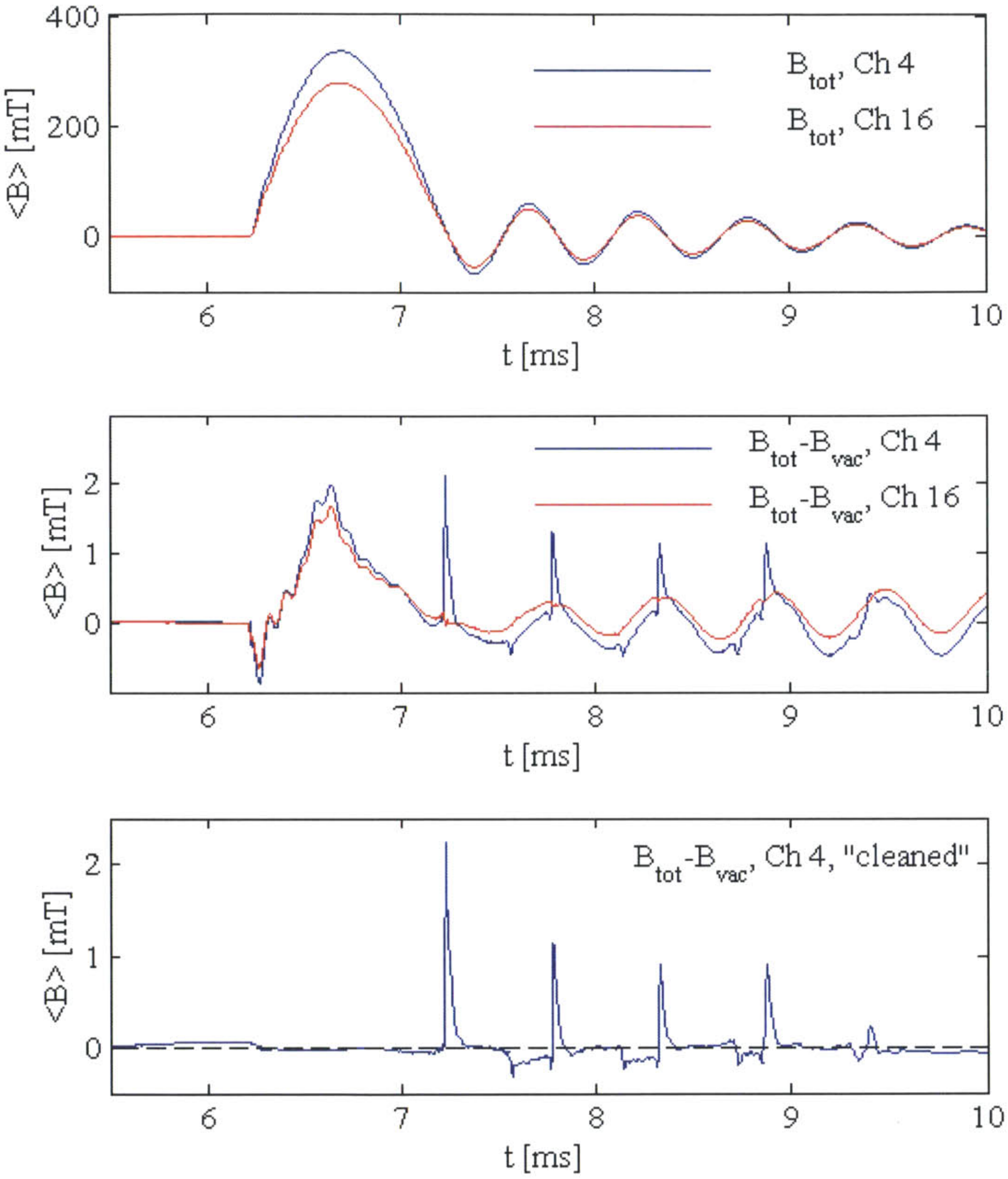

Figure 2-14: Top: an example of the measured fields in two of the magnetic coils. Middle: same as top with vacuum fields subtracted. Bottom: magnetic fields in channel 4 due to plasma currents obtained after further subtracting a fit for the magnetic field component due to the phase shift in the null coil.

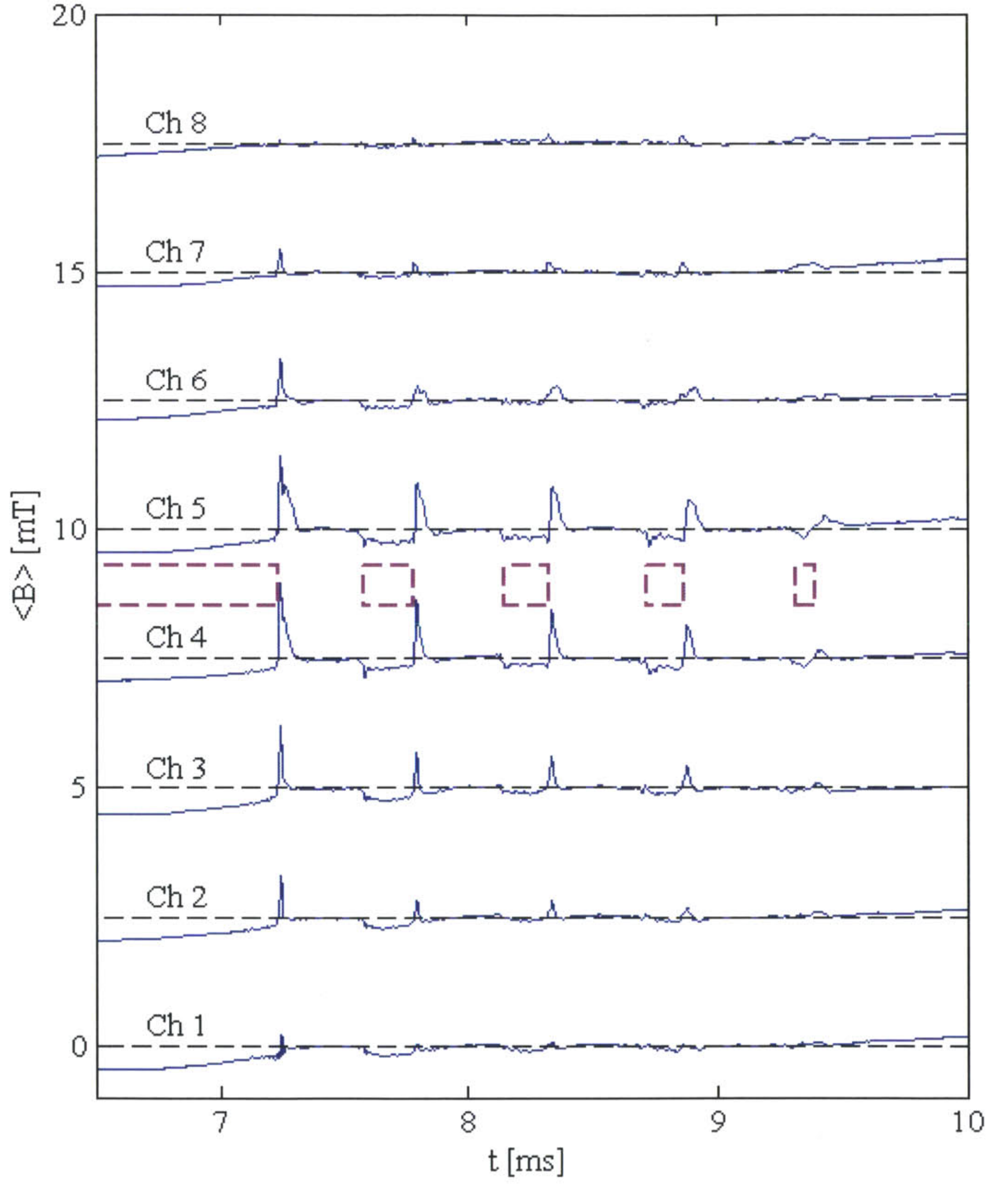

Figure 2-15: An example of the magnetic fields due to the plasma current for a row of the magnetic coils. Dashed magenta line marks the null phase time intervals.

2.4.3 Langmuir Probe Array

Besides currents and magnetic fields, we measure plasma density and temperature using an array of Langmuir probes. The basic principle is to derive plasma parameters from measurements of ion and electron flow to a surface immersed in plasma while varying the bias voltage applied to the surface. Below, we first present in more detail the theoretical principles of the Langmuir probe operation and then discuss the actual implementation in our experiments. Ref. [48] provides a more detailed overview and lists further references.

First, consider a probe in contact with plasma and floating - electrically isolated from the chamber wall, ground, or any other fixed potentials. Due to higher mobility more electrons than ions will flow to the probe and will quickly charge the probe negative. Eventually, the negative potential will reach a large enough magnitude that enough electrons are repelled and the reduced electron particle flux to the probe is equivalent to the nominally smaller ion flux. The probe potential then will no longer change. This steady-state potential is called the floating potential V_f. Again, one expects it to be more negative than the plasma potential V_{pl}. We focus on probe biases V_{bias} near the floating potential and less. At these biases, only the most energetic electrons reach the probe while ions are actually attracted. With flow velocities towards the probe significantly different, equal fluxes then require different ion and electron densities. Thus, the quasineutrality condition is not true in a region called the sheath surrounding the probe. Thickness of the sheath is on the order of several Debye lengths. We aim to determine the plasma parameters in the unperturbed plasma outside of the sheath.

For ions we assume that their temperature is small compared to the energy gain due to the voltage difference between the plasma and the probe. Then at biases near the floating potential and less, as was shown by Bohm and as is further described in Ref. [48], ions flow to the probe at the ion sound velocity c_s. This leads to the ion current to the probe I_i:

$$I_i = neA_pc_s\exp\left(-\frac{1}{2}\right), \tag{2.3}$$

where n is the unperturbed plasma density, e is the electron charge, assuming singly ionized atoms, and A_p is the probe area. The exponential factor accounts for the difference in densities between the inflow at the sheath and of the unperturbed plasma further away from the probe. Here ion current is independent of the bias voltage, hence called the ion saturation current, and of ion temperature. In real experiments, however, ion current increases slightly with increasingly negative probe bias due to expansion of the sheath which effectively increases the probe area.

For electrons, we assume that the Boltzmann relation holds:

$$n_e = n\ \exp\left(\frac{e\left(V_{bias} - V_{pl}\right)}{k_BT_e}\right), \tag{2.4}$$

which translates to the electron current of

$$I_e = -neA_pc_s\sqrt{\frac{m_i}{2\pi m_e}}\ \exp\left(\frac{e\left(V_{bias} - V_{pl}\right)}{k_BT_e}\right). \tag{2.5}$$

Then, from Eqs. 2.3 and 2.5, the total current to the probe as a function of bias V_{bias} is:

$$I\left(V_{bias}\right) = neA_pc_s\left[\exp\left(-\frac{1}{2}\right) - \sqrt{\frac{m_i}{2\pi m_e}}\exp\left(\frac{e\left(V_{bias} - V_{pl}\right)}{k_BT_e}\right)\right]. \tag{2.6}$$

In this treatment, the implicit assumptions are of collisionless plasma near the probes, of low temperature ions, and of Debye length and ion gyroradius much greater than the probe size. Note that it has also been assumed that the electron gyroradius is likewise much greater than the probe size while in our experiments the two quantities can be comparable. However, this should mainly affect the factor in front of the brackets in Eq. 2.5 while leaving the exponential dependence on electron temperature intact [48]. As will be explained below, our analysis uses only the exponential factor of the electron current and is thus applicable even for experiments with comparable sizes of the electron gyroradii and the probes.

To elaborate, we measure the probe current for large magnitude negative bias (-60 V) to determine the ion saturation current. Eq. 2.3 then can be used to calculate density. For these density calculations we assume electron temperature of 20 eV in order to estimate the ion sound velocity c_s. To make an actual electron temperature measurement, we measure the probe current at a range of bias voltages between -70 V and +70 V. Based on Eq. 2.6 we expect a sum of a constant offset and an exponential. As is shown in an example plot in Fig. 2-16 of Langmuir currents of a select probe and time averaged over ten shots for each bias voltage, the experimental trace for large enough biases is no longer exponential. Instead, probe current becomes linear with bias voltage. This signifies that the bias voltage has been increased beyond the validity range of Eq. 2.6 which assumed probe biases near the floating potential and below. This shift to a linear dependence and, as seen in some experimental traces, eventual further decrease in magnitude of slope agrees with expectations based on more complete theoretical treatments which include electron current saturation effects. For our purposes to determine the electron temperature we would fit an exponential to a subset of the bias voltage range from -70 V to up to the inflection point in the graph. For example, in Fig. 2-16 the blue exponential fit is for the bias voltage range of -70 V to +40 V and corresponds to electron temperature of 18 eV.

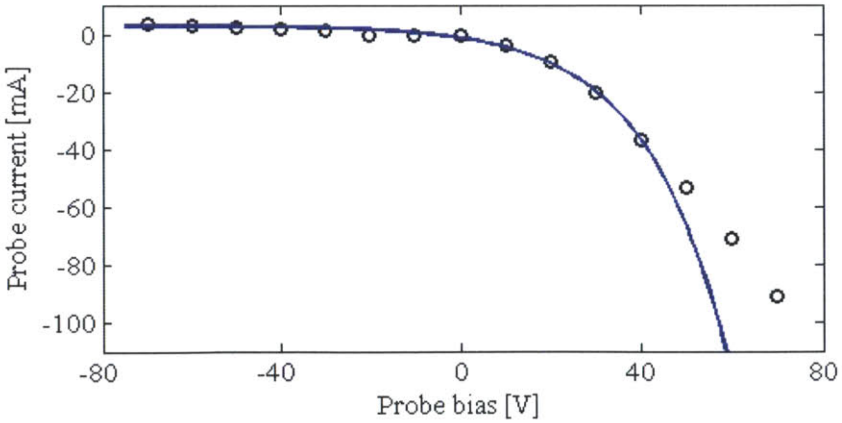

Figure 2-16: Example Langmuir trace for a select probe and time. Black: measured probe current averaged over ten shots for each bias voltage. Blue: exponential fit for the -70 V to +40 V bias voltage range corresponding to electron temperature of 18 eV.

For our probes, we use hollow stainless steel cylinders of 2 mm length and 1.3 mm diameter with soldered on lead wires as schematically shown in Fig. 2-17, left (reproduced from [49]). The hollow cylinders allow us to arrange several probes and their lead wires into a single probe string as shown in an example with two probes in Fig. 2-17, right. We used two sets of Langmuir probes: a single-string Langmuir probe set and an array consisting of six strings.

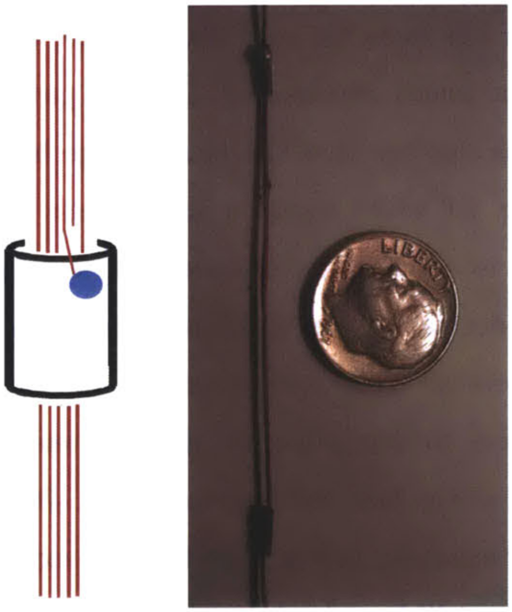

Figure 2-17: Left: schematic of a single Langmuir probe consisting of a hollow stainless steel cylinder with a soldered on lead wire. Right: photograph of two probes as part of a probe string. Reproduced from [49].

The single-string Langmuir probe set can be seen in Figs. 2-6 and 2-18. It consists of 14 probes arranged on a single string that is mounted directly on the Rogowski probe array at Y = -20 mm, Z = 7 mm, and spanning a range from X = -172 mm to X = +172 mm. Thus, while limited to a single Y and Z coordinate, this set of probes provides measurements both radially inside and outside the null coil.

The Langmuir probe array, however, spans a range of Y-coordinates from Y = 0 to Y = 125 mm while limited to the range from X = -139 mm to X = +125 mm. Apart from small unintended deviations of less than 5 mm, all probes are at Z = 0. The array consists of a total of 70 probes with five strings of 12 probes at positive Y

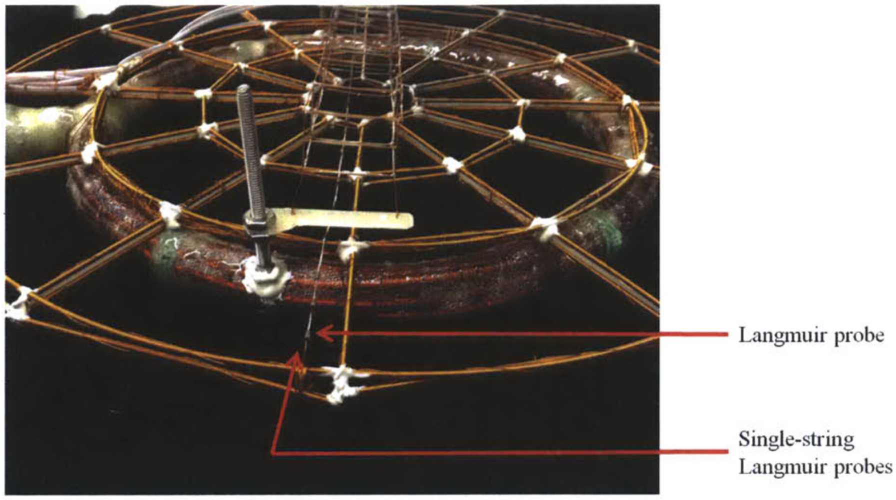

Figure 2-18: Single-string Langmuir probe set mounted on top of the Rogowski array.

coordinates and one string of 10 probes at $Y = 0$ stretched radially within the null coil. The array mounted on the null coil can be seen in Fig. 2-6.

The electric circuit used for Langmuir probes is shown in Fig. 2-19. In order to determine the probe current we aim to measure the voltage drop across a sense resistor with resistance $R_s = 330\ \Omega$. We use a decoupling capacitor $C = 10\ \mu F$ to avoid applying the large DC bias voltage to the digitizer while still measuring the time-dependent plasma signal. A large series resistor $R_1 = 220\ k\Omega$ ensures large overall input resistance for our voltage measurement while a parallel resistor $R_2 = 330\ \Omega$ divides down to acceptable levels the actual voltage applied to the digitizer. Again, the input resistance of the digitizer channels is $R_0 = 500\ \Omega$.

The bias voltage is manually set on a power supply between shots. As verified by digitizing the bias voltage itself, during the shots it remains fixed.

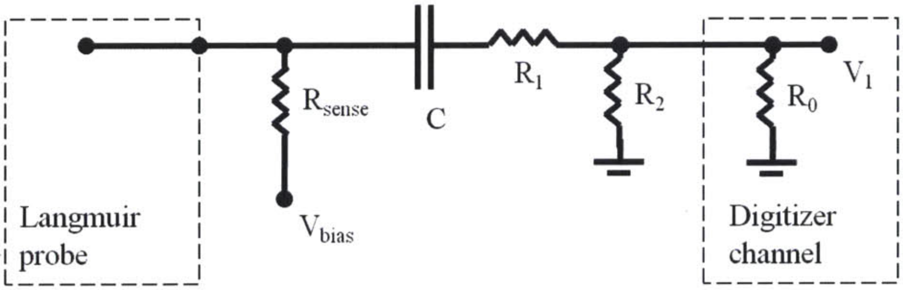

Figure 2-19: Electric circuit for measuring the Langmuir probe current using digitizers.

In previous experiments in our research group with Langmuir probes of this design but with differently created plasmas and, thus, possibly different plasma potentials it was observed that probes can suffer from surface contamination [49]. This would lead to hysteresis in the measured probe currents for bias voltage scans with voltage increasing versus decreasing. We did not observe any such hysteresis. However, at negative bias voltages of -50 V and less we would occasionally observe probes brightening in the visible light camera images. This is explained as probes sourcing electrons and can be seen in data as sharp peaks in the probe current. While these peaks can be easily distinguished in the data, they do overwhelm the real plasma signal and should be avoided. This effect would become more frequent and widespread amongst probes in consecutive shots. We counteract probe contamination by running shots with probes biased at +90 V. Large positive bias voltage leads to an increased electron bombardment and a resulting cleaning of the probe as evidenced by fewer cases of probe brightening in any negative bias voltage shots following the cleaning. We perform this cleaning after every five density measurement shots (run at -60 V bias) and after every shot with bias of less than -40 V during the bias voltage scans.

2.4.4 Fast Camera

We used a Phantom v7.1 camera made by Vision Research to capture high frame rate visible light images of the plasma in our experiments. The resulting frames consisted of 600 × 800 pixels and were captured at a rate of 4700 frames per second. The camera was installed for one of two different views: top and bottom. In the top view, the camera was pointed vertically down looking through a glass window in a vertical port displaced -40 degrees toroidally from the null coil. A tilted mirror that can be seen in Fig. 2-6 was installed high in the chamber and below the port. In combination with this mirror the camera top view provided an overview look of the experimental setup as can be seen in Fig. 6-3. In the bottom view, the camera was pointed vertically up looking through a glass window in a vertical port directly below the null coil. An example of a bottom view image can be seen in Fig. 6-4. We used a 60 μs exposure for the top view images and a 5 μs exposure for the bottom view.

Direct quantitative interpretation of the images is involved due to the line-integrated nature of the data recorded as well as the non-trivial relationship between plasma parameters and the light emitted. It is not attempted here. However, qualitatively fast camera images are used in this work to characterize spatial plasma distribution and magnetic field structure in different field configurations. In addition, the fast camera was invaluable in the experimental process for providing means to quickly evaluate the outcome of a shot without any involved data processing and immediately after the said shot.

Chapter 3

Plasma Gun

3.1 Basic Principles

Plasma in our experiments was created using a washer plasma gun [50–52] built by the author and first used in VTF research on the trigger problem in magnetic reconnection [42, 44, 45]. Originally these plasma sources were developed in the West [53, 54] as well as in the Soviet Union [55] for use in accelerators and in plasma physics research. Nowadays, the guns are considered to be small, clean, directional, and localized sources of ~1 kA electron current and, in addition to VTF, are used in other basic plasma physics facilities (e.g. RWM [56], RSX [57]) as well as in fusion experiments [58].

Basic principles of a washer plasma gun operation are illustrated in Fig. 3-1. The gun consists of a stack of molybdenum (Mo) and boron nitride (BN) washers with a Mo electrode at each end. Neutral gas is injected into the channel formed by the stack. The gun power supply provides discharge voltage V_{dis} across the electrodes breaking down the injected gas. The resulting plasma escapes the channel into the main chamber of the experiment. Additional bias from the bias power supply drives current in the plasma beam.

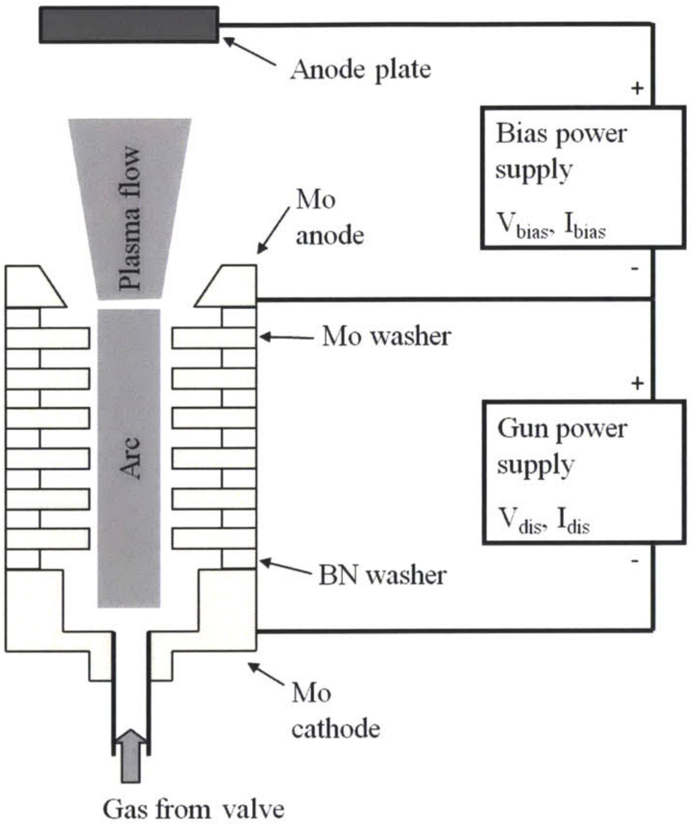
Anode plate
+
Bias power supply
V_{bias}, I_{bias}
-
Plasma flow
Mo anode
Mo washer
+
Gun power supply
V_{dis}, I_{dis}
-
Arc
BN washer
Mo cathode
Gas from valve

Figure 3-1: Basic principles of the plasma gun operation.

3.2 Implementation

An example of an actual design from the RWM facility is shown in Fig. 3-2. To avoid any arcing outside of the main gun channel the stack of washers is contained in an insulator.

In our implementation the stack consists of six Mo and seven BN washers with outside diameters of 14 mm and inside diameters of 6 mm and 10 mm respectively. Each washer is 1.2 mm thick resulting in a total distance of 15.6 mm between the gun cathode and anode. The opening at the gun anode is sloped and over the thickness of 5 mm increases in the inner diameter from 8 mm to 10 mm. An early version of the gun is shown in Figs. 3-3 and 3-4. Eventually, Teflon shielding in addition to the piece shown in Fig. 3-4 was added to more completely surround and insulate the cathode power line. Again, this is necessary to eliminate any arcing between the cathode power line at -400 V and either the anode power line or the gun support both

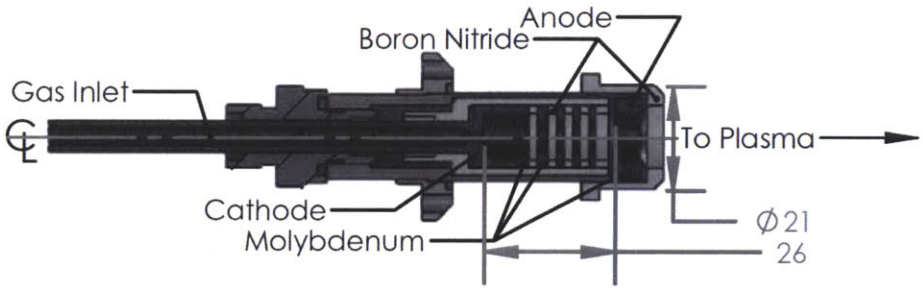

Figure 3-2: An example actual design of a washer plasma gun (RWM facility, reproduced from [56]).

of which are grounded. We shield the gun from the plasma in the chamber using a ceramic housing and a BN shield at the gun output. As can be seen in Fig. 3-4, the gas line is also the cathode power line while the copper connector between the anode power line and the gun also acts as a support.

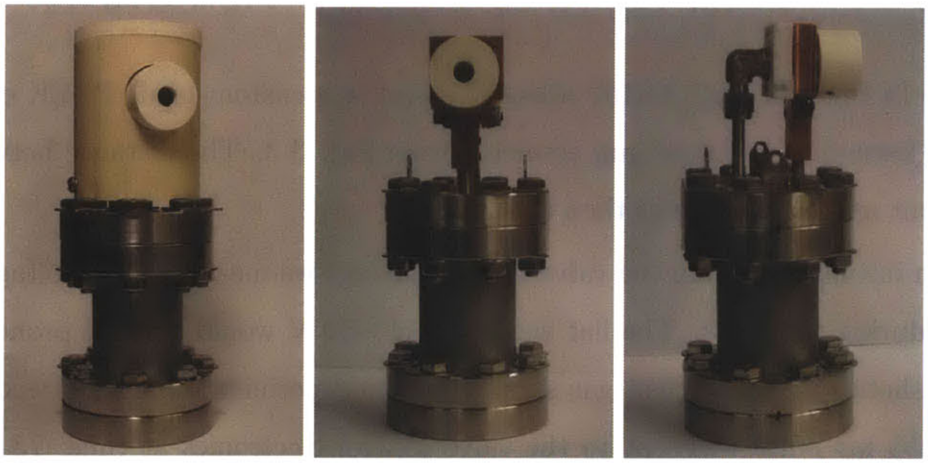

Figure 3-3: Early version of the assembled gun (left) and with the ceramic housing removed (middle and right). More teflon insulation for the cathode power line was eventually added.

Clean and smooth gun operation relies on sufficient supply of gas - argon in our experiments. At the same time, we would prefer to minimize any flow of neutrals into the chamber. Ideally then the gas flow would match exactly in rate and in timing the gun discharge. In reality the flow in the supply line rises smoothly and gradually to a steady state value over a time interval the length of which depends on the pressure in the line and the distance along the supply line between the valve and the gun. Due to this effect we then operated our gun at a 135 Psi line overpressure and placed

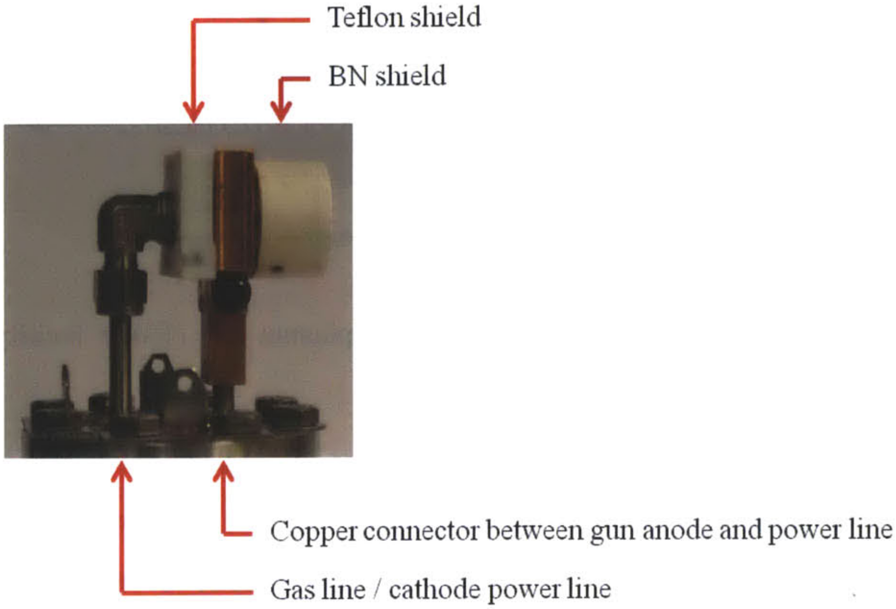
Teflon shield
BN shield
Copper connector between gun anode and power line
Gas line / cathode power line

Figure 3-4: Close up view of the gun with the ceramic housing removed.

the valve (a Predyne A2013-S197 solenoid valve) in a custom-made PEEK container attached immediately to the gun assembly from Fig. 3-3. The distance between the gun output and the valve was then 0.4 m.

When initially choosing the valve timing settings we measured the voltage across the gun during the shots. The flat waveform of ~70 V would become pronouncedly noisy in shots with insufficient gas supply. In our experiments then, for smooth gun firing, a 55 ms pulse was sent to the valve control electronics at time -73 ms with respect to the zero time defined in Table 2.2. Since the valve requires at least a 15 ms pulse to open then the total time the valve was open was likely ~40 ms.

The gun assembly with the ceramic housing and the PEEK valve container was further attached to a 1.5 in diameter stainless steel tube that provided the support and the extension to place the gun output in the middle of the chamber. In order to preclude any arcing between this grounded gun structure and the bias plate at +220 V then a 1 mm Teflon sheet was wrapped around the complete gun assembly inside the main chamber up to the gun's ceramic housing. This setup can be seen in Fig. 2-6.

For the bias plate we used a 8 in by 6 in rectangular stainless steel plate attached to an aluminum rod and centered on the nominal beam location in the poloidal plane. It should be noted that the plate is comparable in size to the observed displacements of the beam during the beam oscillations described in Chapter 5 and is not rotationally symmetric about the beam location. Again, to avoid arcing the rod was placed inside a Teflon tube.

3.3 Electronics

Fig. 3-5 presents a more detailed schematic for our implementation of the general principles from Fig. 3-1.

Both the gun and bias power supplies contain pulse forming networks consisting of capacitors and inductors. The capacitors are charged to 400 V in the gun power supply and to 220 V in the bias power supply. The gun is fired or the bias applied by firing SCR_1 and SCR_3 respectively. The gun power supply has an additional small capacitor C_5 in series with the network and charged to 1.5 kV. Thus the initial voltage applied to the gun is $\sim$1900 V which is enough for the seed breakdown in the gun. C_5 discharges rapidly compared to the network capacitors hence the majority of the power comes from the pulse forming network. The gun is shorted and the gun discharge terminated by firing the SCR_2 crowbar. Not shown in Fig. 3-1 are the electronics necessary for charging the capacitors and for interfacing the power supplies with the triggers from the main control system of VTF.

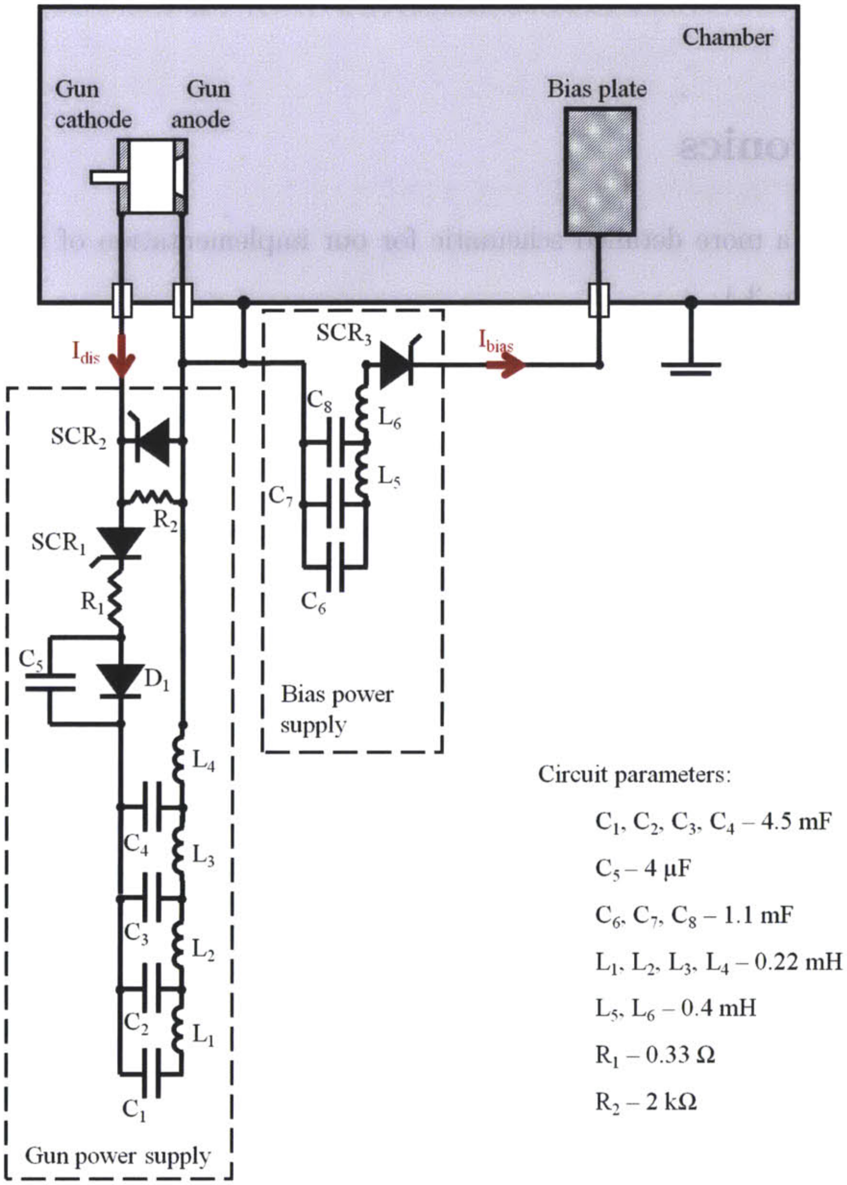
Chamber
Gun cathode
Gun anode
Bias plate
I_{dis}
SCR_3
I_{bias}
SCR_2
R_2
SCR_1
R_1
C_5
D_1
C_8
L_6
L_5
C_7
C_6
Bias power supply
L_4
C_4
L_3
C_3
L_2
C_2
L_1
C_1
Gun power supply

Circuit parameters:

C_1, C_2, C_3, C_4 – 4.5 mF
C_5 – 4 μF
C_6, C_7, C_8 – 1.1 mF
L_1, L_2, L_3, L_4 – 0.22 mH
L_5, L_6 – 0.4 mH
R_1 – 0.33 Ω
R_2 – 2 kΩ

Figure 3-5: Main components of the plasma gun electronics.

3.4 Plasma Gun Currents

The gun and the bias power supplies in Fig. 3-5 drive the correspondingly marked main plasma gun currents I$_{dis}$ and I$_{bias}$ as introduced in the general principles presentation in Fig. 3-1. More detailed current paths are shown in Fig. 3-6 where, in addition, I have in green marked the location of separate Rogowski coils for measurements of specific current components also labeled in green.

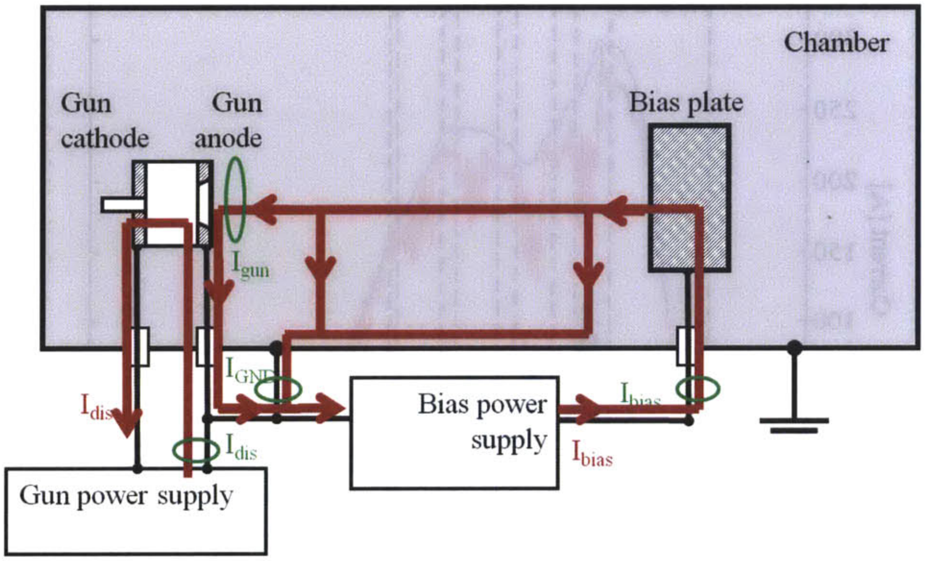

Figure 3-6: The main plasma gun currents (discharge I$_{dis}$ and bias I$_{bias}$) and the location of the separate Rogowski coils.

The first of the two main plasma gun currents is the discharge current I$_{dis}$ whose waveform is shown in Fig. 2-8. It is approximately flat at 0.55 kA. The exact value and shape is unreliable since the waveform consists mainly of the slow current evolution - possibly inaccurate due to long time scale drifts - and of the very fast cutoff at 12 ms that, on the other hand, is too fast and noisy to properly digitize. Nevertheless, the shape agrees to the theoretically expected for the gun power supply pulse forming network with the given circuit components. This current flows along a well-defined path shown in Fig. 3-6 consisting of the gun power supply, the arc between the cathode and the anode within the gun, and the connecting cables.

The second of the two main plasma gun currents is the gun anode bias current I$_{bias}$ shown in Fig. 2-8 and repeated in blue in Fig. 3-7. The nominal current path consists of the anode within the gun, the gun anode bias plate, the plasma beam between the two, the bias power supply, and the connecting cables. However, comparison of the measured current components I_{bias}, I_{gun}, and I_{GND} shown in Fig. 3-7 suggests that some of the bias current flows between the anode bias plate and the chamber wall. The anode bias current paths are also schematically shown in Fig. 3-6.

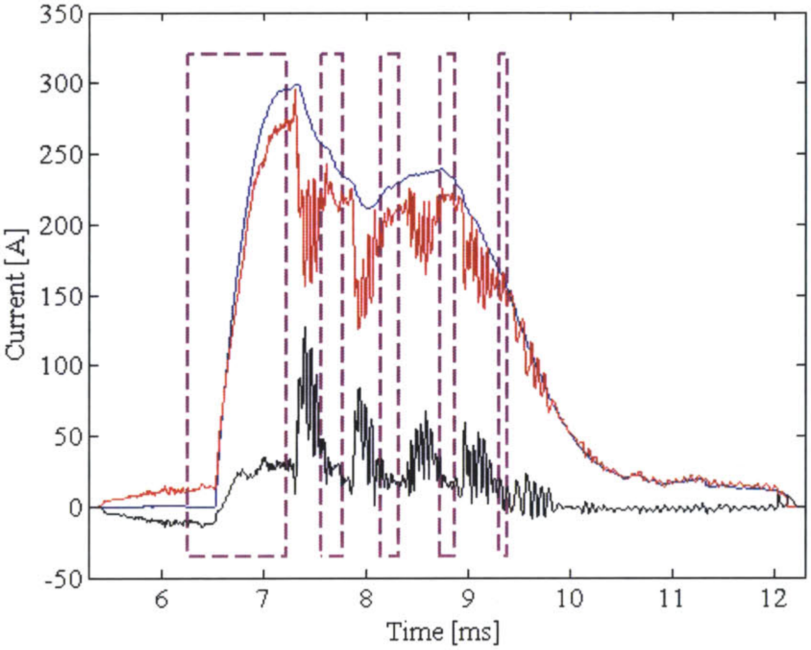

Figure 3-7: The measured current components I_{bias} (blue), I_{gun} (red), and I_{GND} (black) of the gun anode bias current. Enclosed in magenta are the null phase time intervals.

In addition to the two main plasma gun currents we observe an oscillatory current component with path shown in Fig. 3-8 and evident in the I_{gun} and I_{GND} traces in Fig. 3-7. This is the oscillatory current component introduced in Section 2.4 as means to diagnose the overall current structure with the Rogowski probe array. These observed oscillations are described in detail in Chapter 5.

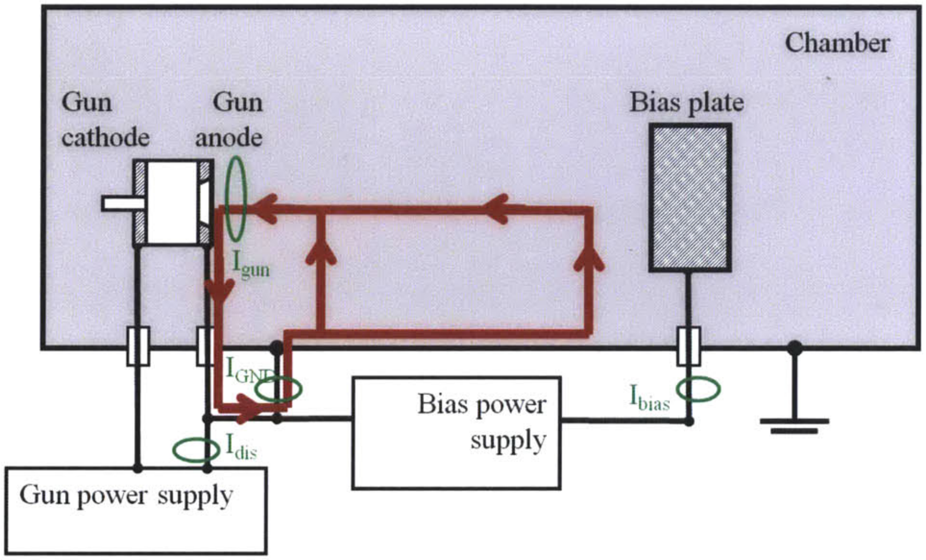
Chamber
Gun cathode
Gun anode
Bias plate
I_gun
I_GND
I_dis
I_bias
Bias power supply
Gun power supply

Figure 3-8: The oscillatory component evident in the I_{gun} and I_{GND} current measurements.

Chapter 4

Expected Field Configurations

In our experiment, the superposition of the background toroidal field and the null coil's dipole field allows for two topologically distinct vacuum magnetic field geometries - normal and tilted.

In the actual plasma experiments, in addition to the external currents in the null coil that produce the vacuum fields, there are plasma currents both sourced by the bias plate as well as induced in response to the driven changes in the magnetic fields. These plasma currents are expected to affect the overall magnetic field geometry. In addition, the plasma response, including magnetic reconnection, is expected to depend on the topology, and one of the goals of this thesis is to experimentally investigate this dependance.

We start by numerically exploring the two different vacuum field topologies. For simplicity we look at the configurations where the background toroidal field is modeled as uniform and straight along the y-direction in cartesian coordinates. The actual background field in the experiment, however, is bent (toroidal) and with 1/R radial dependence in strength.

4.1 Normal

We call the configuration normal when the null coil is in the plane perpendicular to the background field - the x-z plane. The rotational symmetry with respect to the coil dipole axis allows one to calculate the magnetic flux enclosed at a given radius from this axis. Contours of this flux then correspond to magnetic field lines.

Depending on the direction of the current in the null coil, the generated magnetic dipole is either in the positive y-direction (positive current) or in the negative y-direction (negative current). Correspondingly, the total field strength compared to the background field is either increased or decreased by the addition of the coil's dipole field. With total field decreased, the topology may contain an X-line, a single null, or a pair of nulls. Thus one can distinguish four cases:

1. Dipole parallel to the background field; have an X-line,
2. Dipole antiparallel but background field dominates; have an X-line,
3. Dipole antiparallel; background and null coils fields equal and opposite at the center of the coil; have a single null,
4. Dipole antiparallel; null coil field dominates; have two null points.

We start by looking at the first case shown in Figure 4-1 where we have drawn the null coil in red and representative field lines in blue, black, and red. Due to symmetry all of the field lines in the x-y plane remain in the plane. The two magenta points mark X-points in this plane and in full 3D form an X-line in the shape of a circle in the x-z plane. The blue field lines are open field lines which start and end at infinity. The black field lines are closed. In red are separatrices between the two regions of different topologies.

4.1.1 With X-points

With the current in the null coil negative, coil's dipole is opposite to the background field and again, as shown in Figure 4-2, two X-points form (magenta) as part of an X-line in the shape of a circle in the x-z plane. However, now the X-line is radially inside the null coil.

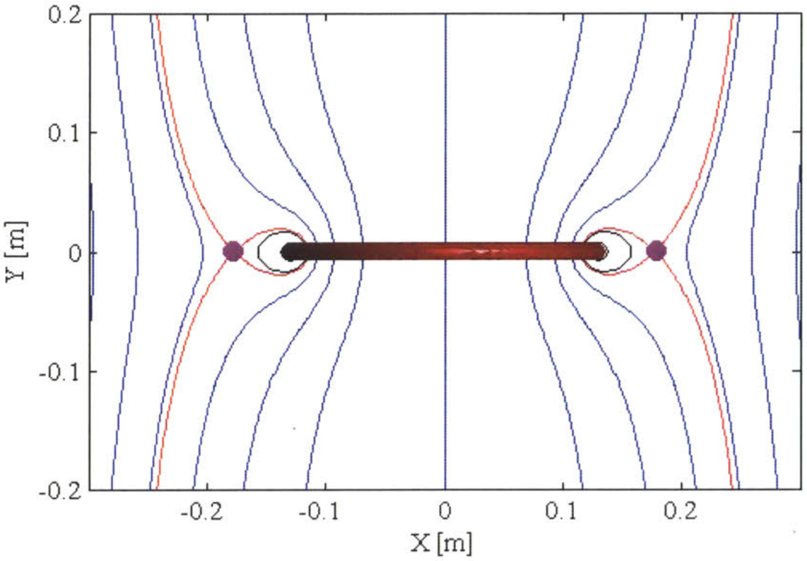

Figure 4-1: Representative open (blue), closed (black), and separatrix (red) field lines with the null coil's dipole parallel to the background field. Also shown are two x-points (magenta). This calculation corresponds to 22.7 mT background field and 10.85 kA total null coil current.

4.1.2 With Null Points

As the null coil current is further decreased, the radius of the X-line decreases and the X-points in the x-z plane move closer. With our parameters, at -4.63 kA the two X-points merge into a single null point located at the coordinate origin and shown in green in Fig. 4-3.

Further decreases lead to a splitting of the single null point into two located on the y-axis. As shown in Figs. 4-4 and 4-5, at -12.4 kA the separation between the null points reaches more than 20 cm.

In this normal configuration the two null points are directly connected with a spine along the y-axis. The fan of each null point, locally parallel to the x-z plane, further away from a given null point connects to the fan of the other null point forming a closed surface that encloses the null coil. All of the field lines inside this fan surface (black), with exception of the spine (red), are closed while all of the field lines outside

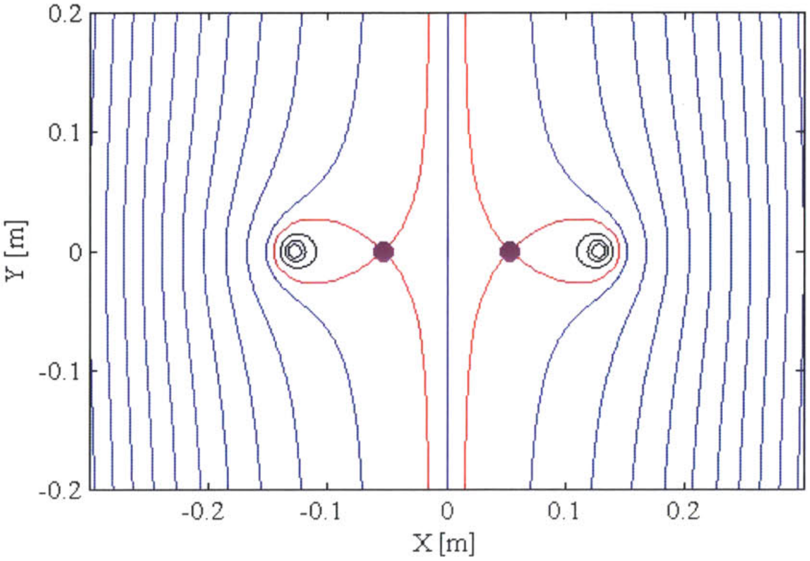

Figure 4-2: Representative field lines with the null coil's dipole antiparallel to the background field and an X-line radially inside the null coil. For clarity, the null coil itself is not shown. Null coil current is -4.00 kA

(blue) are open. Thus, this fan surface is also a separator surface.

Looking at field lines that start in the neighborhood of the y-axis at negative y coordinates, once the nulls have formed, only a single field line - the spine - crosses the null coil plane radially inside of the null coil. All other field lines are directed around the null coil and cross the null coil plane radially outside of the null coil.

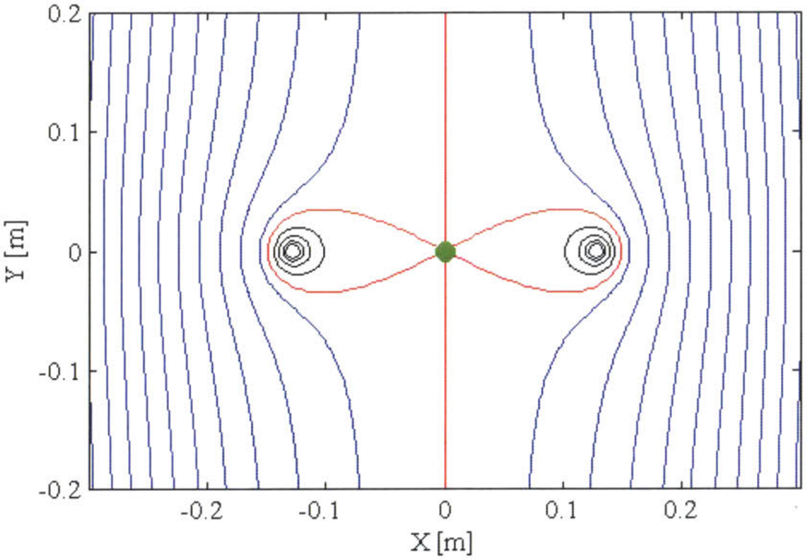

Figure 4-3: Representative field lines with the null coil's dipole antiparallel to the background field and one null point formed (green). Null coil current is -4.63 kA

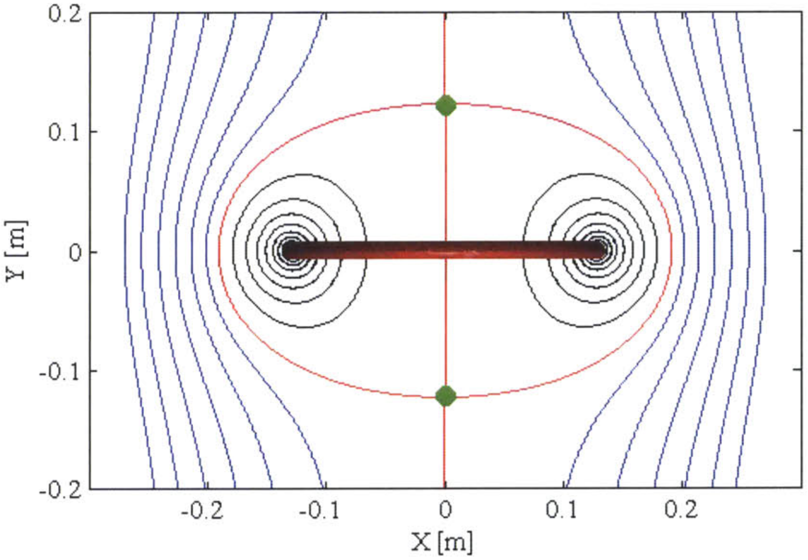

Figure 4-4: Representative field lines with the null coil's dipole antiparallel to the background field and two null points formed (green). Null coil current is -12.4 kA

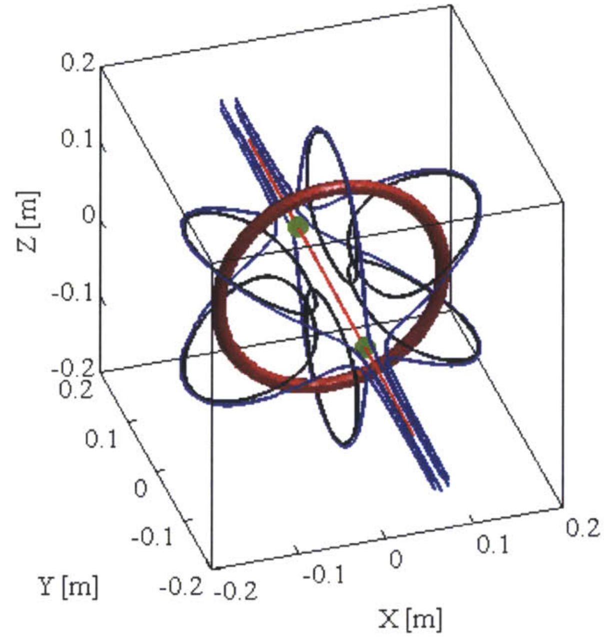
0.2
0.1
0
-0.1
-0.2
Z [m]
0.2
0.1
0
-0.1
-0.2
Y [m]
-0.2
-0.1
0
0.1
0.2
X [m]

Figure 4-5: Representative field lines in 3D with the null coil's dipole antiparallel to the background field and two null points formed (green). Null coil current is -12.4 kA

4.2 Tilted

We call the configuration tilted when the null coil is not in the plane perpendicular to the background field. We limit our investigation to a rotation of the null coil around z-axis. There rotational symmetry is broken and we trace field lines numerically using the calculated values of the total magnetic field.

Again, the direction of the null coil current determines if the component of the coil's magnetic dipole along the background field is positive or negative. We focus on negative current which produces magnetic dipole moment with a negative y-component opposite to the background magnetic field. We recognize three different topologies depending on the relative strengths of the background field and the null coil field at the center of the null coil:

1. Background field dominates at the center of the null coil,
2. Null coil field dominates at the center of the null coil,
3. The limiting case between the above two.

4.2.1 Null Coil Field Dominates

In this topology the net null coil current and the resulting field are large enough that the null coil field dominates the background field at the center of the coil. An example is shown in Fig. 4-6 where we are displaying representative field lines of the x-y plane. The null coil intersects the plane at points O_1 and O_2. Marked in green are the two null points N_1 and N_2. In blue are sample field lines in topologically different regions described below while in red and labeled are separatrices between these regions.

In this plane, all field lines to the left of the separatrix A-N_2-C' and to the right of the separatrix C-N_1-A' flow around the null coil radially outside. Field lines that originate between A and B encircle the null coil once and exit the figure between A' and B'. Lastly, field lines starting between B and C encircle the null coil and asymptotically approach O_1. Similarly, field lines that exit the figure between A' and B' can be traced back to encircle the null coil and asymptotically approach O_2.

In the null point terminology, field lines B-N_1-C and B'-N_2-C' are spines while field lines A'-N_1-O_1 and A-N_2-O_2 belong to the fans of null points N_1 and N_2 correspondingly.

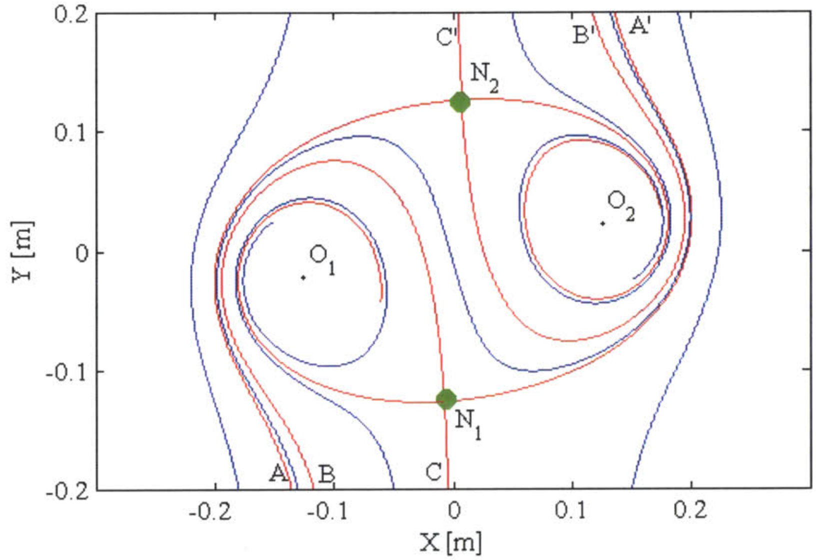

Figure 4-6: Representative field lines in the x-y plane with the null coil tilted, it's dipole antiparallel to the background field and two null points formed (green). Null coil current is -12.4 kA. Null coil field dominates.

These field line topologies extend to field lines outside the x-z plane as well as illustrated in Figs. 4-7 and 4-8 showing representative field lines from two different views. First, there are field lines that flow around the null coil radially outside (black and outside blue). Second, there are field lines that encircle the coil one or several times before exiting the figure (cyan). Also repeated from previous figure are the spines (red) and a field line asymptotically approaching the null coil (inside blue). There are no field lines that would intersect the null coil plane radially inside the null coil without encircling the coil at least once. The two null points are not directly (without encircling the null coil) connected with a field line radially inside of the null coil. Thus, all of the field lines either flow around the null coil or encircle it.

Field lines outside of the x-y plane do not asymptotically approach the coil and instead encircle the coil only a finite number or times if at all. The number of times

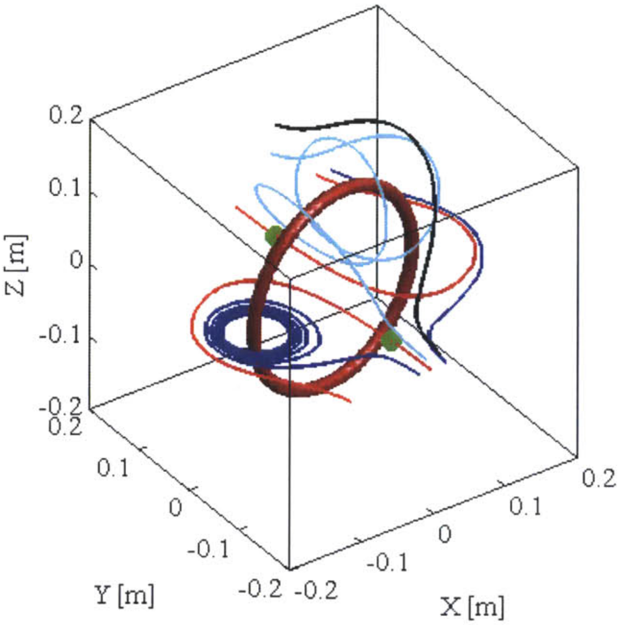

Figure 4-7: Representative field lines in 3D with the null coil tilted, it's dipole antiparallel to the background field and two null points formed (green). Null coil current is -12.4 kA. Null coil field dominates.

a field line starting at a given coordinate in the x-z plane and at Y = -0.2 m encircles the null coil is shown in Fig. 4-9 and will further be referred to as the encirclement number for a given field line.

Field lines with a given encirclement number fill a volume in space. Volumes corresponding to different encirclement numbers are separated by separatrix surfaces that originate at the null points as fan surfaces. Some of the surfaces - originating at the lower, N_1 null point and corresponding to encirclement numbers 0-2 - are depicted in Fig. 4-10. The encirclement number depends on the azimuthal angle of the field line in the fan plane. If one examines fan field lines with increasing azimuthal angles starting with the positive x-direction, then first there is a range of angles for which the encirclement number is zero (Fig. 4-10, left), followed by a range of angles with encirclement number of one (Fig. 4-10, middle), two (Fig. 4-10, right) and so on.

For a given encirclement number, the two separatrix surfaces intersecting the two null points together form a closed separatrix surface as shown in Fig. 4-11. The field line - a separator - at the intersection of the tow separatrix surfaces must then cross

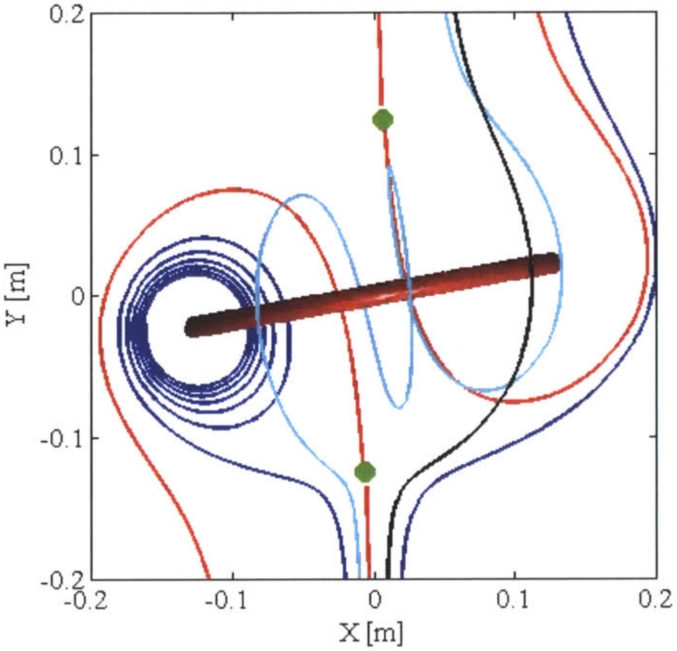

Figure 4-8: Representative field lines in 3D with the null coil tilted, it's dipole antiparallel to the background field and two null points formed (green). Null coil current is -12.4 kA. Null coil field dominates. View along the negative z-axis

both of the null points. Separators for encirclement numbers zero (blue), one (black), and two (magenta) are shown in Fig. 4-12.

Separatrix surfaces of different encirclement numbers are nested as demonstrated in Fig. 4-13 where color is used to indicate the encirclement number of a given surface. Field lines that do not originate at null points, depending on their encirclement number, then lie between certain nested separatrix surfaces consistent with Fig. 4-9.

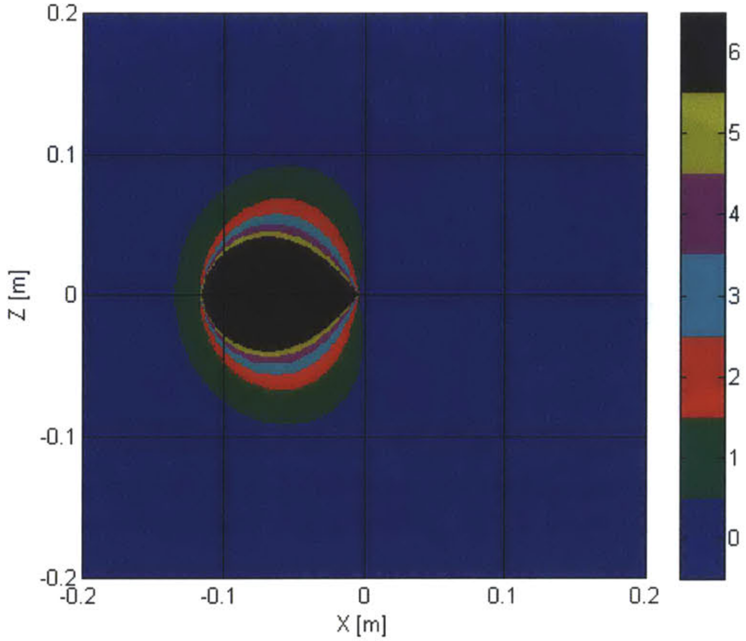

Figure 4-9: Number of times a field line starting at a given coordinate in the x-z plane and at Y = -0.2 encircles the null coil for the tilted and null coil field dominated configuration

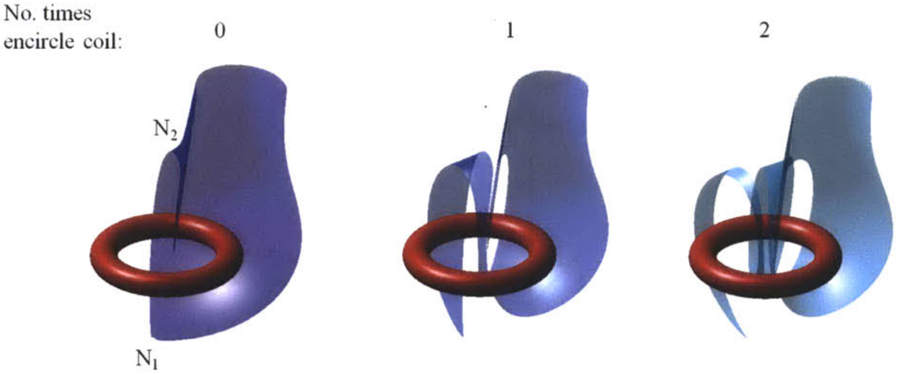

Figure 4-10: Separatrix surfaces originating from the lower, N_1 null point corresponding to different encirclement numbers.

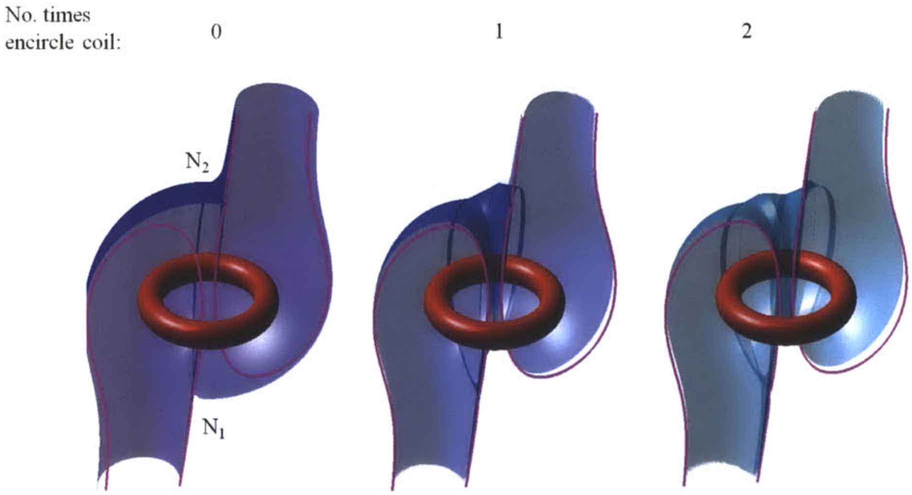

Figure 4-11: Complementary separatrix surfaces of the two null points for different encirclement numbers. Also shown in magenta are the spine lines for the two null points N_1 and N_2.

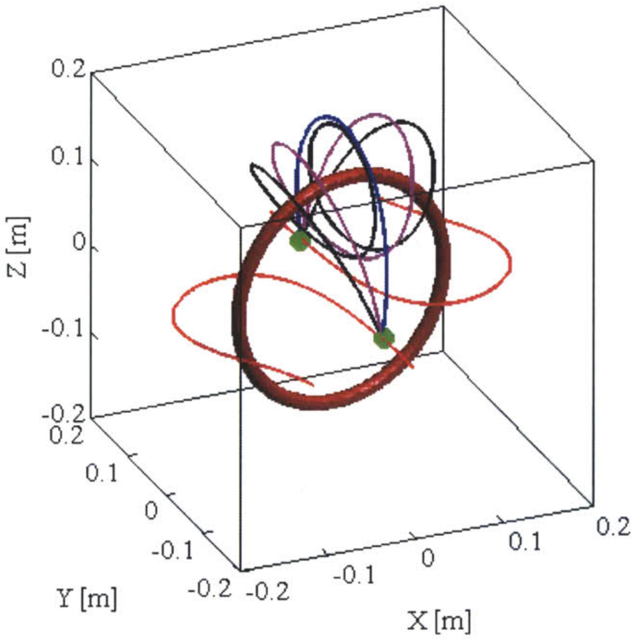

Figure 4-12: Separators for encirclement numbers zero (blue), one (magenta), and two (black) connecting the two null points marked in green. Also shown in red are the spine lines.

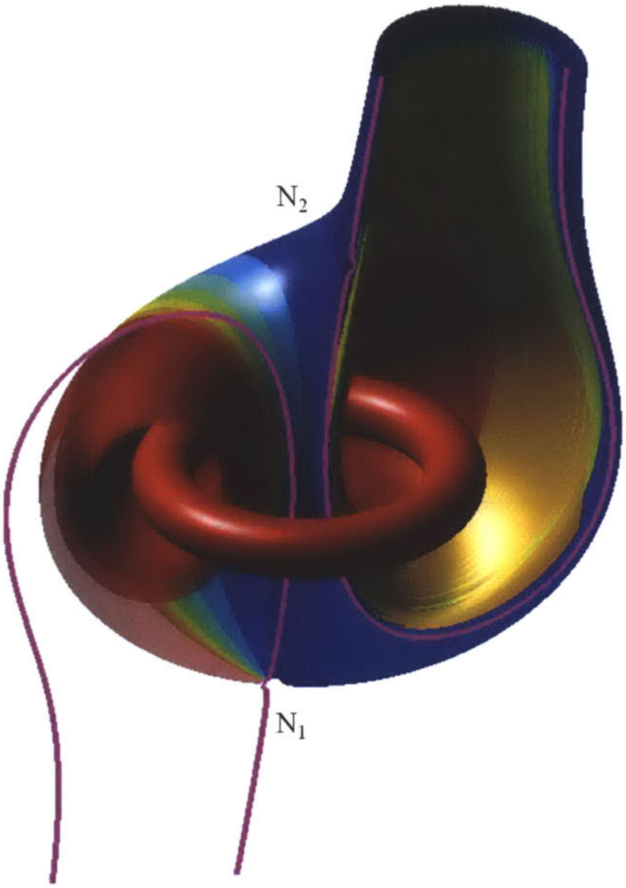

Figure 4-13: Nested separatrix surfaces originating from the lower, N_1 null point corresponding to different encirclement numbers. Also shown in magenta are the spine lines for the two null points N_1 and N_2.

4.2.2 Background Field Dominated and Limiting Configurations

When the current in the tilted null coil is negative but of smaller magnitude, then the background field dominates at the center of the null coil. A representative topology is shown in Fig. 4-14 where the total null coil current is -3.5 kA. In this figure there is a range of field lines starting between B and C and exiting between B' and C' that cross the plane of the null coil radially inside the coil without encircling the coil once. Generalizing to field lines outside the x-z plane as well, the two halfspaces on either side of the null coil are directly (without flowing around) connected with field lines radially inside of the null coil. Thus, in addition to field lines that either flow around the null coil or encircle it, there are field lines directly crossing through the null coil plane.

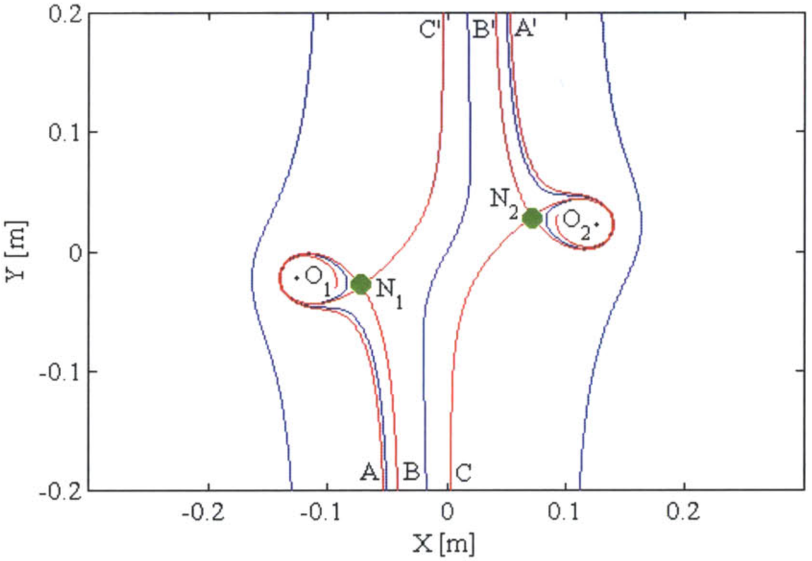

Figure 4-14: Representative field lines in the x-y plane with the null coil tilted, it's dipole antiparallel to the background field, and two null points formed (green). Null coil current is -3.5 kA. Background field dominates.

Lastly, Fig. 4-15 with the total null coil current of -4.15 kA depicts the limiting case between the background and null coil field dominated configurations. Here only a single field line B-N_1-N_2-B' through the null points directly connects the two halfspaces on either side of the null coil. All other field lines either flow around or encircle the null coil.

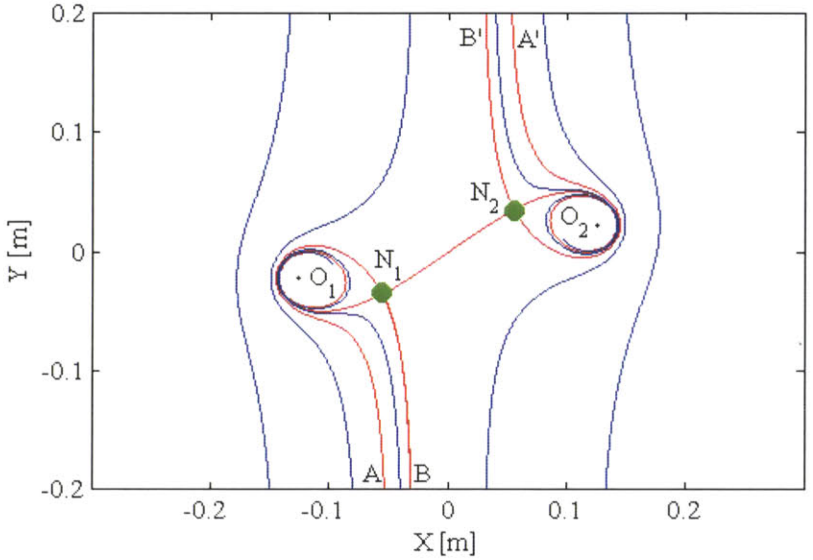

Figure 4-15: Representative field lines in the x-y plane with the null coil tilted, it's dipole antiparallel to the background field, and two null points formed (green). Null coil current is -4.15 kA. This is the limiting case between the background and null coil field dominated configurations.

Chapter 5

Plasma Beam Oscillations

This chapter is dedicated to plasma beam oscillations which we observe even when the null coil is not fired and the only applied magnetic field is the background toroidal field. Understanding the nature of these oscillations is important not only to satisfy scientific curiosity, but also to distinguish any observed reconnection dynamics from the underlying current beam dynamics present even without the reconnection. In addition, as described in Section 2.4, we trace the beam current oscillations to diagnose the overall current structure using the Rogowski probe array, which provides unreliable current measurements at lower frequencies.

5.1 Observations

5.1.1 Current Signatures

As was already mentioned in Chapter 3, the plasma beam oscillations are observed in the separate Rogowski coil current measurements and are present even when the null coil is not fired as shown in Fig. 5-1. During the bias current flattop phase these oscillations are of $\sim$11 A magnitude and $\sim$30 kHz frequency and can also be seen in the Rogowski probe array data presented below.

First, in Fig. 5-2 we plot the current oscillations in the plasma beam flowing out of the gun (black) and the total sum of the oscillations measured by the Rogowski

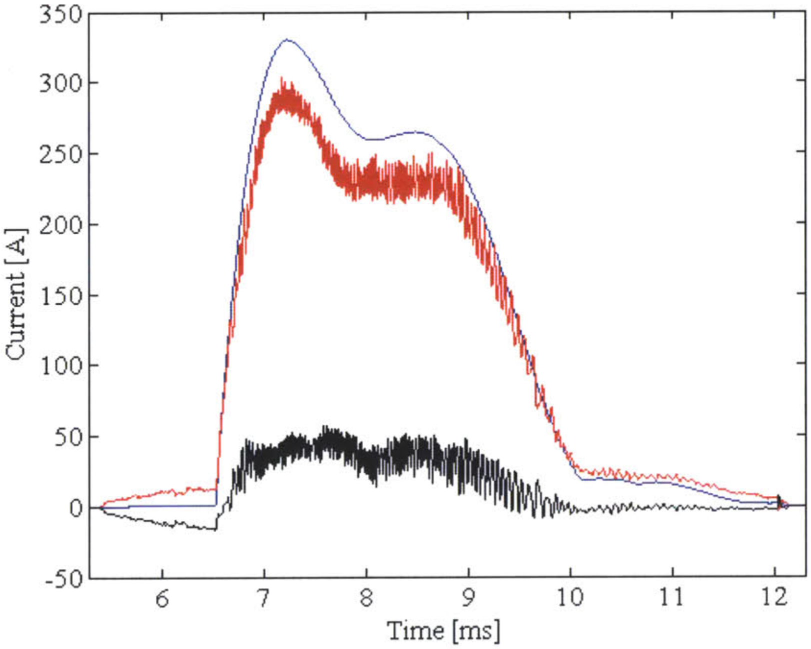

Figure 5-1: The measured current components I_{bias} (blue), I_{gun} (red), and I_{GND} (black) of the gun anode bias current where the latter two exhibit prominent oscillatory component. The null coil was not fired and the only applied magnetic field is the background toroidal field.

probe array coils (blue). This measurement was used to calibrate the Rogowski probe array coils with respect to the separate Rogowski coil measuring the beam current at the gun output. It can be seen that the oscillations agree up to a shift of 4 μs. With separation of gun and array of 1 m this corresponds to the phase speed of 250 km/s.

Second, also in Fig. 5-2 in red is shown the current oscillation summed over the coils in the inner-most band and the center coil. Since this sum is not just a multiple of the total sum (blue) then there must be periodic changes in the radial location of the current as well and not just changes in magnitude.

Furthermore, in Fig. 5-3 we plot the current oscillations of representative four coils of the 12 coils forming the radially inner-most band of the Rogowski probe array. Signals are shifted in time based on the expected phase shift for probes separated by 90 degrees and the angular velocity of a 29 kHz perturbation. We also shift signals vertically. The similarity of the signals differing only in the magnitude of the perturbation suggests that within the area spanned by the inner-most probes

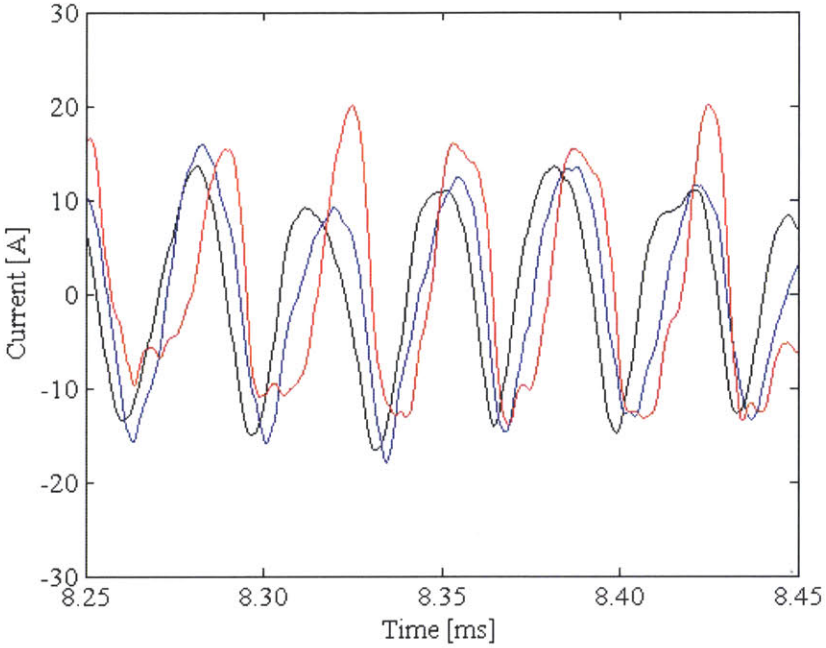

Figure 5-2: The measured current oscillations at the gun output (black) and summed over all of the Rogowski probe array coils (blue). The waveforms are nearly identical except for a phase shift. Also shown (red) is the total signal of the Rogowski probe array coils in the inner-most band and in the center coil.

the observed current oscillation can be interpreted as a gyrating beam of nominally constant current with magnitude then modulated by both the oscillation in the total current magnitude and periodic change in the radial location. Beam gyrations are in the direction of the electron diamagnetic drift.

In addition, if we assume the fluctuations to longitudinally follow at a radius of r = 5 cm the twisted field lines of the plasma beam with 220 A of current in the 22 mT axial magnetic field then the 29 kHz gyrations translate to oscillations along the beam with phase velocity of 230 km/s in close agreement with the measured phase speed of 250 km/s.

Coils in the middle and outer bands do not have waveforms that within each band would be similar in shape and differing only in magnitude and phase. This suggests that in the observed oscillations any component due to the rotating constant current beam is dominated by a rotationally asymmetric component due to a shift in the radial location of current in and out of each of the probe bands. This asymmetry in

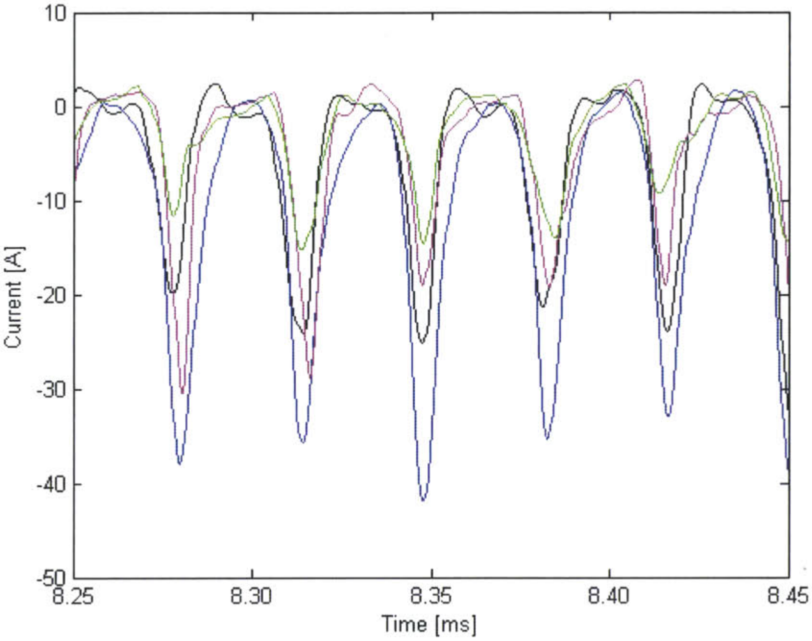

Figure 5-3: The measured oscillations of four Rogowski array coils in the inner band separated by 90 degrees, shifted in time correspondingly, and shifted vertically.

the middle and outer bands can be seen in data frames from a single oscillation period shown in Fig. 5-4. While the oscillations in the inner band have a pronounced component due to a beam rotating, the oscillations in the outer band are just rotationally asymmetric pulses of current through the lower probes. Probes in the middle band exhibit a combination of both a rotational component and a rotationally asymmetric pulsed component.

To summarize, we observe current signatures of the plasma beam oscillations at one dominant frequency (29 kHz) consistent with a superposition of the following modes:

- A beam of current of constant magnitude distributed mainly within the area covered by the center and inner-band probes and gyrating in the direction of the electron diamagnetic drift,
- A rotationally symmetric oscillation in the total current (m = 0 mode),
- A rotationally asymmetric periodic changes in the current location most promi-

nently seen in the outer-band probes as periodic pulses of current through the lower coils.

5.1.2 Density Signatures

In addition to plasma current measurements, we can use data from the Langmuir probe array to further characterize the oscillating beam. Since we did not make Langmuir probe measurements in the dedicated experiments without the null coil firing then we use data at select time intervals from shots with the null coil firing. In particular, we assume that the latter part of the compression phase provide an accurate representation of the beam oscillations.

First, in Fig. 5-5 we plot the densities measured by eight of the single-string Langmuir probes fixed to the Rogowski coil array at the same Y-coordinate of 2.2 cm and spanning a range of x-coordinates between -8.7 and +8.8 cm. z-coordinate of all probes is 0.7 cm. Data is from a single shot at five different times covering one oscillation period. Initially, density is peaked around X = 2 cm and has FWHM of about 3 cm. In panel 3 a half-period later the peak has shifted to X = -1 cm and FWHM has increased to about 5 cm. A full period later in panel 5 the density profile is similar to the original profile in panel 1. These density measurements are consistent with the interpretation that a plasma beam of FWHM of 3-5 cm is gyrating in the x-z plane between X = -1 cm and X = +2 cm.

Second, the density oscillations are in-phase across the Langmuir array in the y-direction and also in-phase with current oscillations. This is illustrated in Fig. 5-6 where we plot the measured density by different Langmuir array probes as well as the current measured by the Rogowski array probes during a compression phase between two null phases marked with the dashed magenta lines. In particular, in the top panel we show the measured density traces for two Langmuir array probes at y = 2.7 cm. The two probes are on the opposite sides of the gyrating beam. Hence, a peak in density measured by one probe corresponds to a dip in density measured by the other. In the middle panel, we show density from Langmuir probes at the same x-coordinates but further away along the y-coordinate at Y = 12.5 cm. The oscillations are in phase with the probes at Y = 2.7 cm indicating that the oscillation wavelength along the y-direction is much larger than 10 cm. In the bottom panel, we show the current fluctuations measured by two of the inner band Rogowski array probes also on opposite sides of the beam. Negative peaks in the current are in phase with peaks in density.

Third, to characterize the electron temperature of the beam plasma we look at shots at different Langmuir probe biases. Again, in an attempt to obtain measurements unaffected by the null coil we use data from the latter part of the compression phase at a time when the current through the null coil is zero. Our results are presented in Fig. 5-7. On the left are ten shot average density profiles for the same probes as in Fig. 5-5 at four select times of zero null coil current each near the end of a compression phase.

On the right are the Langmuir characteristics for the probe at X = -1 cm that samples the beam peak. The corresponding probe is marked in red in the plots on the left. Since in each shot at one of the chosen times the beam can be in a different phase in its oscillation then there is a spread in the measurements beyond that of random shot-to-shot irreproducibility. Each measurement can be sampling the beam peak, a minimum a half-period offset in phase from the peak, or any state in-between. Thus, to physically interpret the data, for each of the biases we look at ten measurements and discard the maximum and minimum values at any given point in time. The leftover largest and smallest values are then assumed to represent the maximum and minimum values as the result of an average beam oscillation. Using this approach we obtain two Langmuir characteristics at each point in time. One corresponds to the beam crossing the given Langmuir probe and the other to the minimum when the beam is the most displaced during its oscillation.

Overall, data from Fig. 5-7 suggests that the average beam peak density is close to $\sim 1 \cdot 10^{18}$ m^{-3} with temperature approaching 20 eV.

To summarize

- Density measurements in one plane indicate a plasma beam oscillating in the X-coordinate consistent with the beam gyrating in the X-Z plane,

- Density increases correspond to increases in current magnitude,
- Density oscillations remain in phase across the Langmuir array indicating that the oscillation wavelength along the Y-direction is much larger than 10 cm,
- Beam peak temperature is close to 20 eV.

In addition, the oscillations in the beam location can be seen in the visible light images captured with the fast camera.

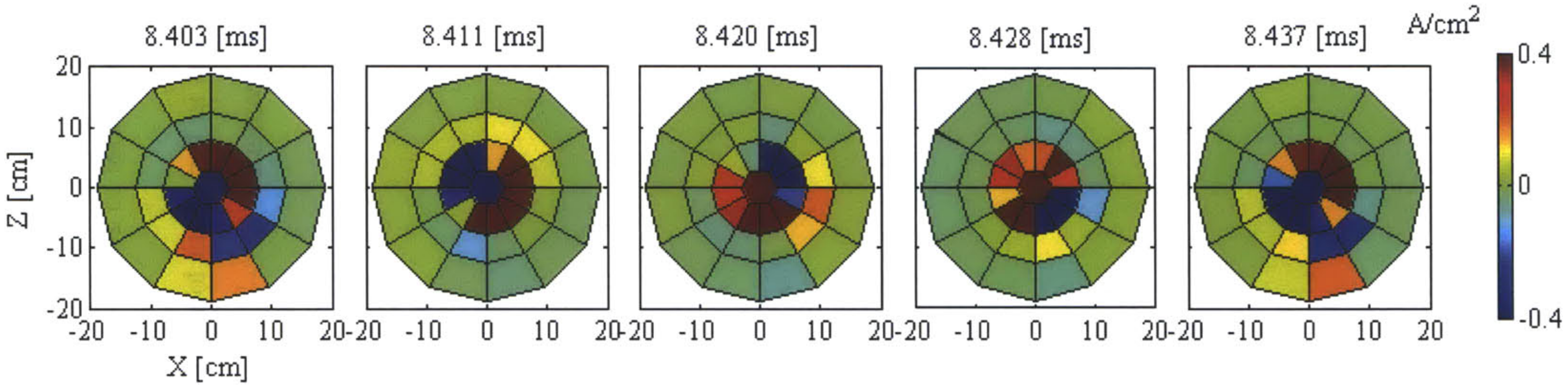

Figure 5-4: Measured current density oscillations in data frames from a single oscillation period. The null coil is not fired.

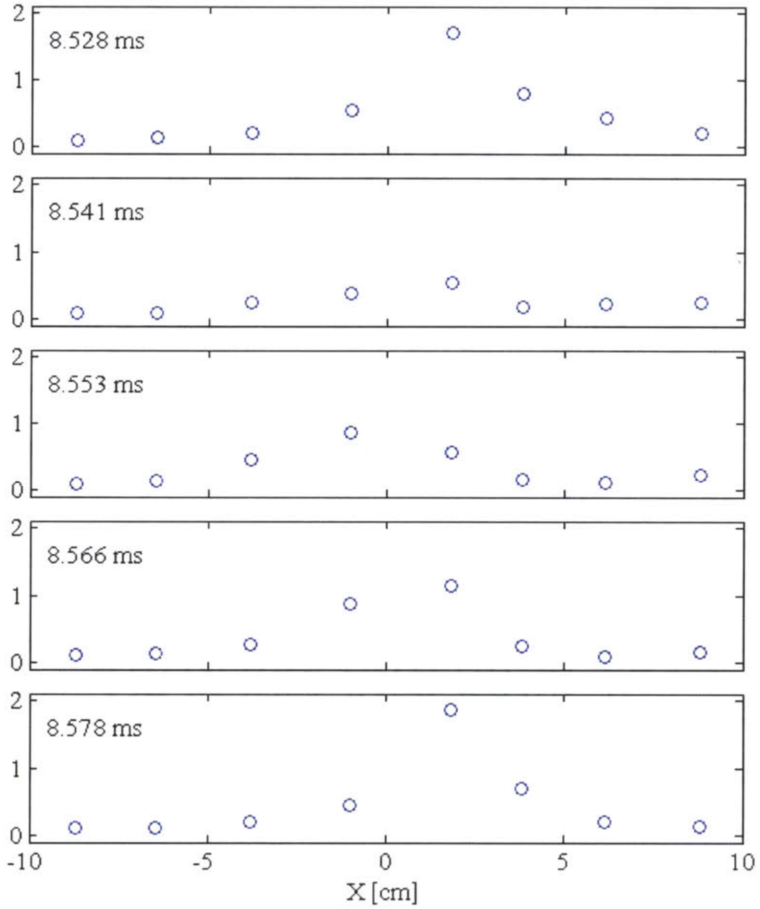

Figure 5-5: Plasma density measured by the single-string Langmuir probes at different x-coordinates at five different times during a single oscillation period consistent with a plasma beam oscillating in the x-coordinate.

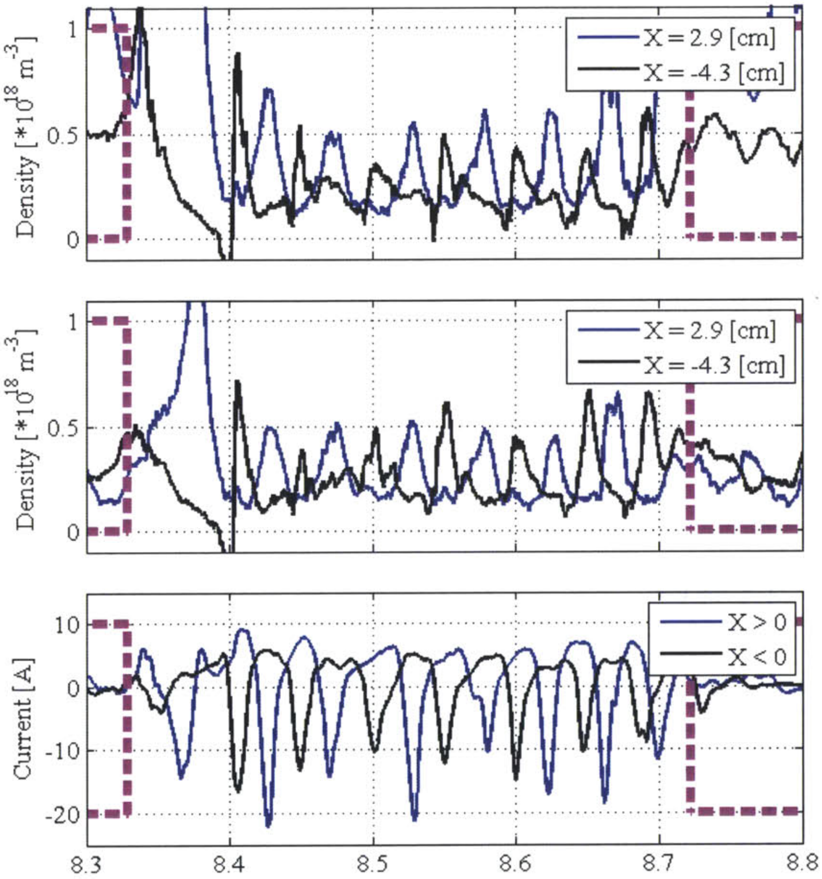

Figure 5-6: Density and current oscillations during a compression phase between two null phases marked with dashed magenta line. Top: density measured by two Langmuir array probes at Y = 2.7 cm on opposite sides of the plasma beam. Middle: same as top only at Y = 12.5 cm. Bottom: current oscillations measured by two of the inner band Rogowski array probes also on opposite sides of the beam.

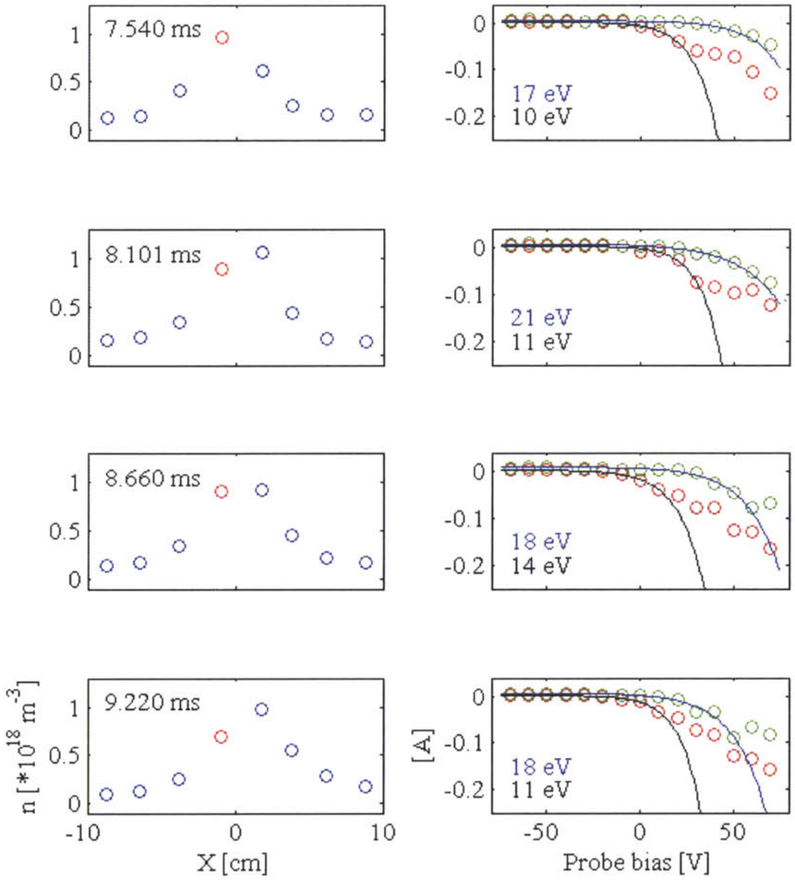

Figure 5-7: Left: average beam density measured by the single-string Langmuir probes. Right: the Langmuir characteristics and the corresponding electron temperature ranges as a result of the gyrating beam for the channel marked in red on the left. All measurements were made at zero null coil current near the end of a compression phase.

5.2 Interpretation

The observed plasma beam oscillations are not the focus of this thesis and here we provide only the basic discussion on the possible nature of the fluctuations.

5.2.1 Kink Instability

Beam instability of the washer plasma guns has already been reported before [59, 60] and attributed to the kink instability of the current-carrying plasma beam. According to the theory first developed by Kruskal and Shafranov [61, 62], a plasma beam becomes unstable when the safety factor $q\left(r\right)$ drops below the threshold value $q\left(a\right) = 1$ at the plasma edge at the radius a. The safety factor can be expressed as

$$q\left(a\right) = \frac{\left(2\pi a\right)^2 B}{\mu_0 I_p L}, \tag{5.1}$$

where B is the axial magnetic field, I_p is the plasma current enclosed in the radius a, and L is the axial length of the beam. This can be rewritten as the threshold value of I_p:

$$I_{p,th} = \frac{\left(2\pi a\right)^2 B}{\mu_0 L}. \tag{5.2}$$

The plasma beam becomes unstable when the current increases above the threshold value. Derivation of these threshold values assumes that the beam is line-tied at both ends. In experiments like ours one end of the beam connects to a bias plate and is not line-tied. In such cases the threshold current is a half of that given by Eq. 5.2.

With $a \sim 5$ cm, $L = 2$ m between the gun and the bias plate, and $B = 22$ mT one gets $I_{p,th} \sim 860$ A and $0.5 \cdot I_{p,th} = 430$ A for the case where only one end of the beam is line-tied. The exact value would depend on the choice for the beam radius a but could conceivably lie below the beam plasma current in our experiment of ~200 A. That being said, we believe that the observed fluctuations are not due to the kink instability the main reasons being that the fluctuations can already be observed in the current magnitude for beam currents of some 20 A (see Fig. 5-1 and show no dependence on the externally set B-field.

5.2.2 Drift Waves

Plasma density oscillations with parallel wavelength much larger than the perpendicular wavelength gyrating in the electron diamagnetic drift direction in a cylindrical plasma column with a radial density gradient can potentially be explained by drift waves. Here we explore this possibility based on the most basic description following Bellan [63]. A review paper by Horton [64] can provide the starting point for a reader interested in a more comprehensive exposition.

The setup for the most basic drift wave is shown in Fig. 5-8. In this model a cylindrical beam of dense plasma stretches along the background magnetic field and is surrounded by a less dense plasma. We assume ions colder than electrons such that for an azimuthal density perturbation on the boundary of the beam ion response is adiabatic while electrons are isothermal. The difference in the electron and ion response leads to an electric field such that the resulting ion E×B drift is out of phase and opposite to the original perturbation and leads to oscillations.

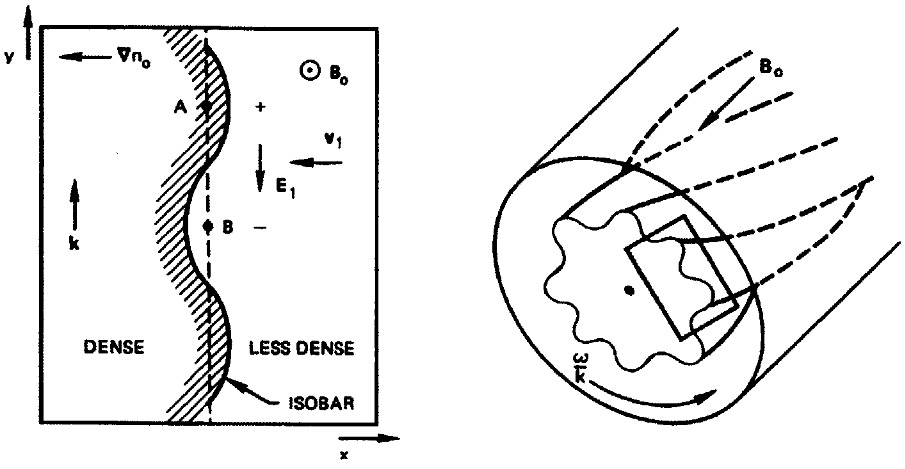

Figure 5-8: Right: basic setup for a drift wave where a cylindrical beam of plasma stretches along the background magnetic field with azimuthal density perturbations. Left: density oscillations out of phase with an opposing E×B drift leads to oscillations. Reproduced from [65].

This oscillation is characterized by azimuthal phase speed equivalent to the electron diamagnetic drift velocity u_{de} given by

$$u_{de} = \frac{k_B T_e}{e L_n B}. \tag{5.3}$$

The oscillation angular frequency then is ω^*:

$$\omega^* = k_y u_{de}. \tag{5.4}$$

In the above equations e is the electron charge, L_n is the radial density gradient length scale, and k_y is the azimuthal wave number.

A more detailed treatment that includes collisions leads to an instability with the oscillatory part ω_r given by

$$\omega_r = \frac{\omega^*}{1 + k_y^2 \rho_s^2}, \tag{5.5}$$

where ρ_s is the ion sound gyroradius:

$$\rho_s^2 = \frac{k_B T_e}{m_i \omega_{ci}^2}. \tag{5.6}$$

Estimating $L_n \sim 5$ cm and $k_y = \mathrm{m/r}$ with m = 1 and r $\sim$ 5 cm leads to $f_r = \frac{\omega_r}{2\pi} \sim 2$ kHz while $L_n \sim 3$ mm already reproduced the observed $f_r = 30$ kHz. These estimates together with the agreement in the qualitative nature of the observed mode suggest that the observed oscillations are due to drift waves.

Chapter 6

Results for the Normal Configuration

The normal configuration is conceptually simpler than the tilted configuration and provides a reference case. Out approach is to first understand the plasma dynamics in the more symmetric normal configuration and then look for differences in the tilted configuration measurements.

6.1 Magnetic Field Structure

Qualitatively, based on the visible light images from the fast camera, we can confirm the overall magnetic field structure of the normal configuration that was described in Chapter 4. In Figs. 6-1 and 6-2 we see the plasma beam in the top and bottom camera views respectively before the beam bias is applied and the null coil is fired. Beam intersects the null coil plane in the center. When the null coil is fired, we observe the visible beam plasma to mostly follow the magnetic field structure. Thus, images taken during the null phase in Figs. 6-3 and 6-4 show the beam plasma following the open field lines and surrounding the closed field line structure of the null coil similar to that of Fig. 4-4. The space around the null coil that is expected to contain closed field lines remains dark.

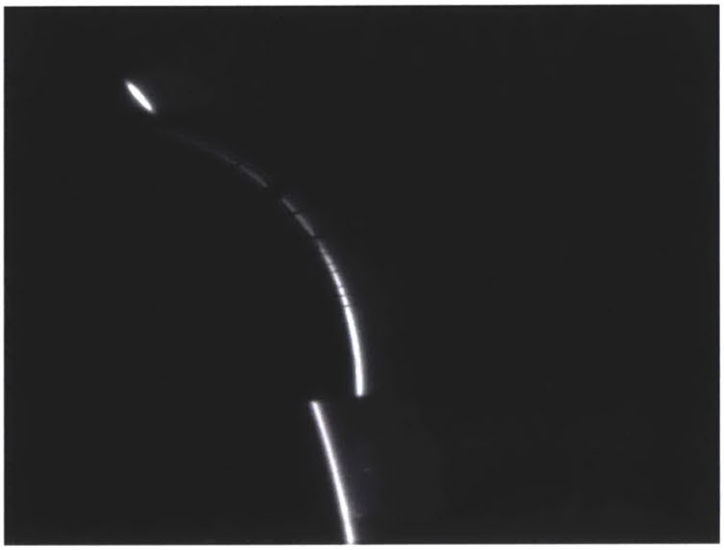

Figure 6-1: Plasma beam before the beam bias is applied and the null coil is fired in a visible light fast camera image from the top view. Beam intersects the null coil plane in the center.

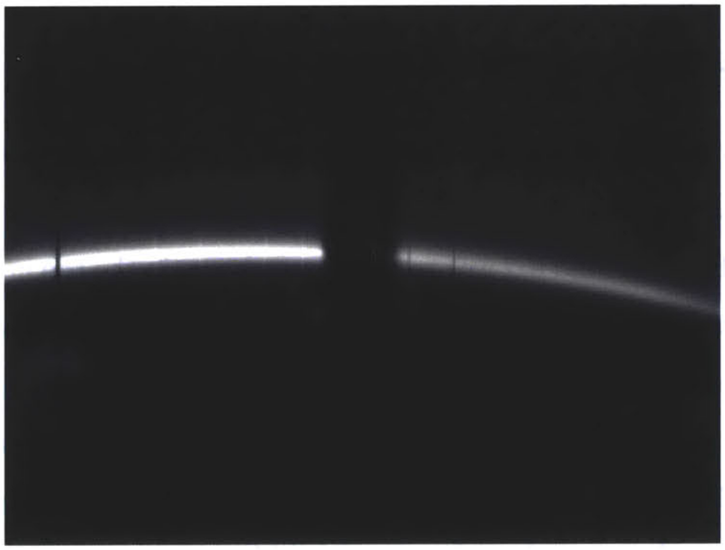

Figure 6-2: Plasma beam before the beam bias is applied and the null coil is fired in a visible light fast camera image from the bottom view.

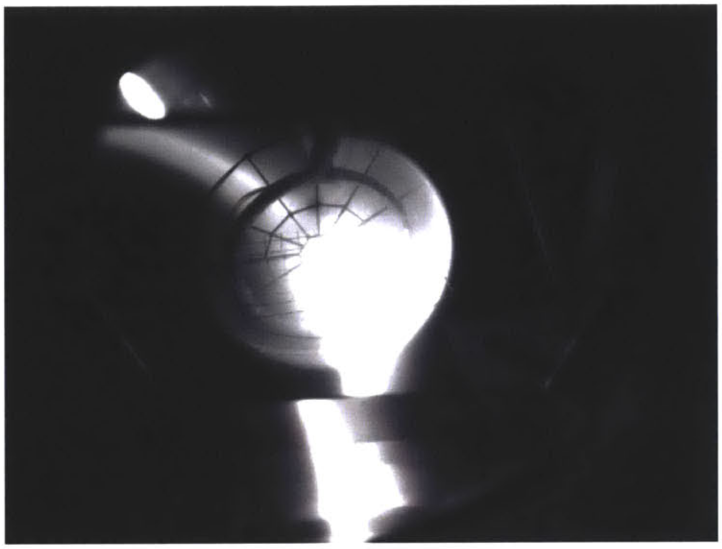

Figure 6-3: Fast camera top view during the null phase.

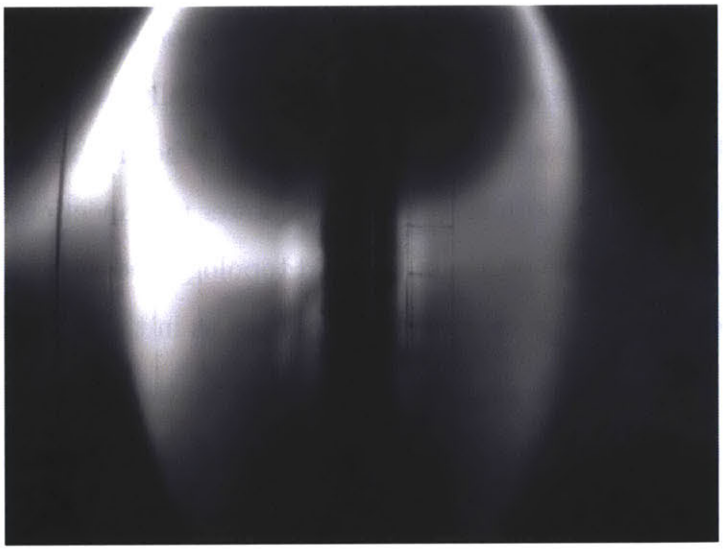

Figure 6-4: Fast camera bottom view during the null phase.

6.2 Current Structure

As described in Chapter 5, our plasma beam undergoes oscillations even in experiments without any current in the null coil. These oscillations lead both to oscillations in the total plasma current magnitude as measured at the gun output as well as periodic gyrations in the beam's poloidal location. As illustrated in Fig. 6-5, nature of these current oscillations is modulated by pulsing current through the null coil. The compression phase exhibits pronounced and regular oscillations of ~20 A amplitude and ~20 kHz frequency qualitatively similar to the case of no null coil current. However, during the null phase the oscillations significantly decrease in magnitude to just a few amperes.

Noteworthy, changes in oscillation amplitude are not symmetric between when the coil field is increasing and when decreasing. More specifically, when the reverse field magnitude is increased then plasma beam oscillations decrease in magnitude as nulls are formed and plasma is spread out. However, when the reverse field magnitude is decreased again then the re-establishment of oscillations is delayed. We believe that these differences are due to different reconnection rates during the time intervals of coil field increasing and decreasing. In one case reconnection is asymmetric reconnection between gun plasma on the open field lines and essentially vacuum on the closed field lines allowing large reconnection rates while in the other reconnection is symmetric with dense gun plasma on both sides leading to lower reconnection rates. This slower reconnection rate delays the return of the field topology and with it re-compression of the plasma beam despite the same driver dynamics as in the coil field increase phase.

During the null phase we observe almost exact anti-correlation between the current fluctuations summed over probes radially inside the null coil (center coil and coils in the two inner bands) and the current fluctuations summed over probes radially outside the null coil (outer probe band). During the same time, as was already described above, current fluctuations at the gun output are of significantly smaller magnitude than during the compression phase. An example of the summed fluctuations is presented in Fig. 6-6 while Fig. 6-7 shows data from the separate probes

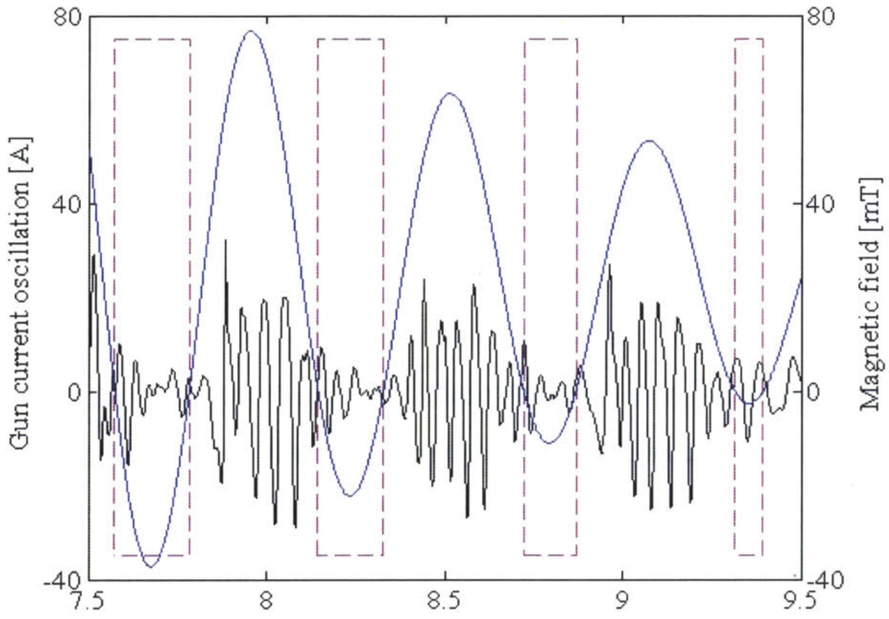

Figure 6-5: Modulation of the oscillations in the total plasma current at the gun output (black) as the null coil current is pulsed (represented by the total estimated field at the center of the coil, blue). The null phase time intervals are enclosed in magenta.

at select moments in time. At times, the anti-correlation is within separate sectors as well whereby an increase in the current in a given coil in the outer band is simultaneous with a decrease in the current in the inner band coils in the same sector. However, this anti-correlation within sectors is not as consistent and persistently true as the anti-correlation between the summed currents.

We interpret these anti-correlated current fluctuations as portions of the current filament between the bias plate and the gun intermittently changing radial location from along the spine radially inside the null coil to around the null coil radially outside. However, one would expect these oscillations in the radial location to be related to oscillations in the current magnitude at the gun output as was the case for the experiments without any null coil current described in Chapter 5. Instead, as in Fig. 6-6, we observe a prominent increase in the anti-correlated current fluctuations while the fluctuations at the gun output significantly decrease in magnitude. This suggests that these fluctuations are unrelated to the plasma beam dynamics and instead originate at the null points.

An alternative interpretation would attribute the anti-correlated current fluctuations to currents flowing along the closed field lines which encircle the null coil. Thus, current flowing in one direction radially outside the null coil returns in the opposite direction radially inside the null coil. This interpretation leaves unclear what process drives these fluctuating currents along the closed field lines. In contrast, our preferred interpretation that the fluctuations are portions of the plasma beam between the bias plate and the gun changing radial location between inside and outside the null coil has the applied bias as a clear driver and only lacks definite explanation for the intermittent changes in the radial location of the current filament.

A hybrid explanation of the anti-correlated current fluctuations involves intermittent field topology changes whereby an open field line between the gun and the bias plate lying radially outside the null coil changes topology to an open field line that still connects the gun and the bias plate but encircles the coil.

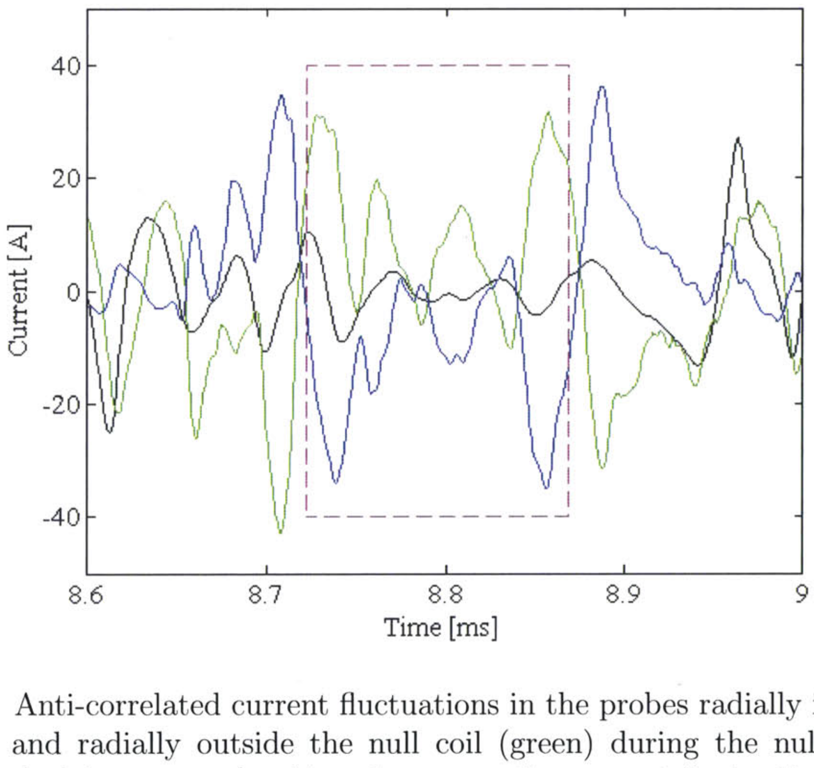

Figure 6-6: Anti-correlated current fluctuations in the probes radially inside the null coil (blue) and radially outside the null coil (green) during the null phase (time interval marked in magenta). Also shown are the current fluctuations at the gun output (black).

In addition, during the X-line phase with null current decreasing we consistently observe in repeated experimental runs a positive current pulse in the coils that are in the inner bands and with positive z-coordinates and a corresponding negative pulse in the coils with negative z-coordinates. This is shown in Fig. 6-8 where on the left we are plotting current fluctuations in four coils, which are marked in magenta in the array data figure on the right. The fluctuations are averages over ten shots. We are also showing in cyan the ten traces from separate experiments used in calculating the average to illustrate the consistency of this observed signature. The vertical dashed magenta line as in previous plots marks the expected end of the null phase and beginning of the X-line phase. The vertical green line corresponds to the time chosen for plotting on the right the average current density from the whole Rogowski array. We observe an increase in the current in the upper inner probes and a decrease in the lower inner probes. This pulse is first observed in the inner band probes and then ~5 μs later in the middle band probes.

This signature is consistent with a loop of current crossing the Rogowski probe array plane and we attribute it to the current sheet along a circular X-line tilted with respect to the Rogowski probe array plane and intersecting it. A pulse that is first observed in the inner probes and only later in the middle probes then agrees with the X-line moving outward as the null coil field is decreased. In a perfectly symmetric normal configuration the X-line would lie in the null coil plane and would not intersect the Rogowski probe array plane. Our data suggests misalignment between the two planes. Furthermore, consistency of observations over ten shots suggests that the symmetry breaking is not random.

In addition, we ran a series of experiments with the null coil and the attached Rogowski probe array displaced within the poloidal plane with respect to the plasma beam. Nominally, the null coil and the array are centered on the plasma beam whereas in this configuration without the null coil fired the beam would intersect the Rogowski probe array at the inner probe band. The field configuration remained normal.

First, as shown in Fig. 6-9, the modulation of the plasma current oscillations at the gun output is less pronounced with the beam displaced.

Second, with the beam displaced, current fluctuations summed over probes radially inside the null coil and summed over probes radially outside the null coil are not anti-correlated during the null phase. Instead, as illustrated in Fig. 6-10, the oscillations have a small phase shift similar to the oscillations in experiments where the null coil is not fired at all. This suggests that in these experiments the current oscillations shift between the inner and outer Rogowski probe bands due to the gyration of the beam which, as was already discussed above, is present even during the null phase unlike in the experiments where the null coil was centered on the beam. The absence of anti-correlated oscillations implies absence of the null point dynamics that were present when the beam was centered on the null coil.

Finally, neither Fig. 6-9 nor Fig. 6-10 exhibit pronounced differences in the current structure between when the coil field is increasing and decreasing. This implies that with the beam displaced the field lines reconnect without inducing a significant plasma current response. As further evidence we did not observe pronounced current loop signatures of the kind shown in Fig. 6-8 for the case of null coil centered on the beam.

To summarize, we have made the following current structure observations in the normal configuration:

- We observe differences in frequency and amplitude of the plasma beam oscillations between compression and null phases. Oscillations are of significantly larger amplitude without nulls present.

- During the X-line phase, we observe differences in the current structure between when the coil field is increasing and decreasing. The re-establishment of oscillations is delayed when the field is decreased in the second part of the null phase and in the following X-line phase. These differences are due to different reconnection rates during the time intervals of coil field increasing and decreasing.

- In the presence of nulls we observe anti-correlated current pulses between the inner and outer probe bands. This suggests portions of the plasma beam between the bias plate and the gun changing radial location between inside and outside the null coil due to dynamics at the null points.

- During the X-line phase with null coil current decreasing in magnitude we observe a current signature consistent with a loop of current crossing the Rogowski probe array plane. We attribute this signature to a current sheet along a circular X-line tilted with respect to the Rogowski probe array plane and intersecting it.

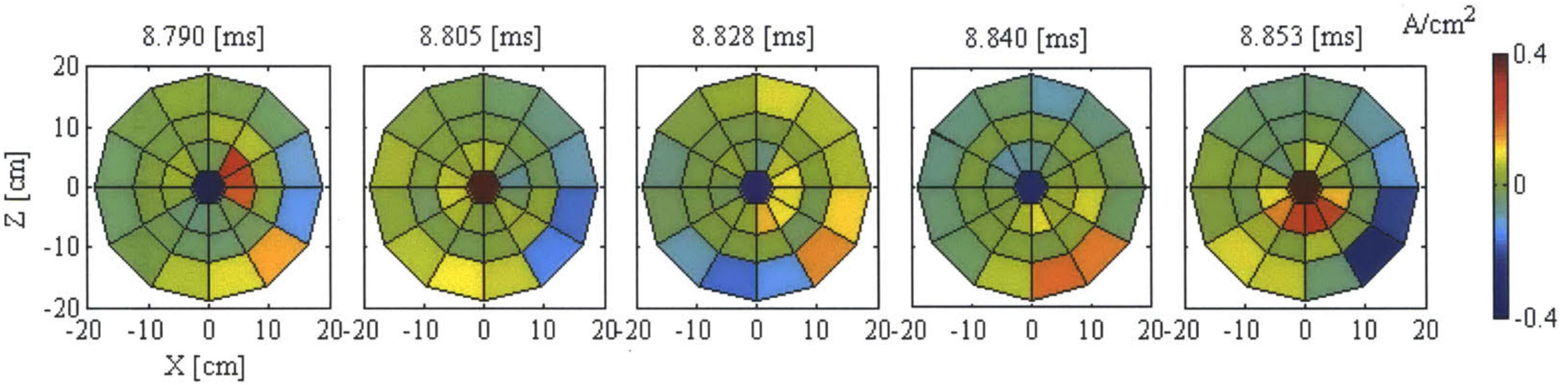

Figure 6-7: Current fluctuations as measured with the Rogowski probe array at select times during a null phase. At times, anti-correlation is not only between fluctuations summed over bands, but also within separate sectors.

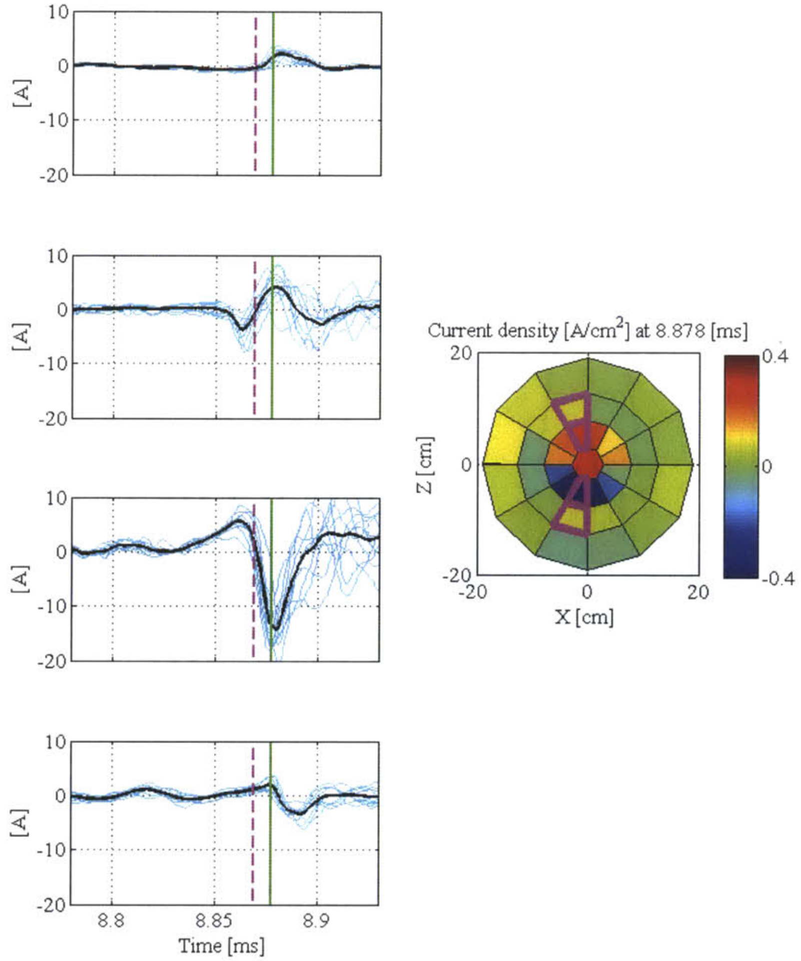

Figure 6-8: Left: current fluctuations in four coils (marked in magenta on the right) averaged over ten shots. Example of the ten separate time traces before averaging (cyan) are shown for one probe. Magenta line marks the expected end of the null phase and beginning of the X-line phase. Right: the average current density from the whole Rogowski array at one select time frame marked in green on the left.

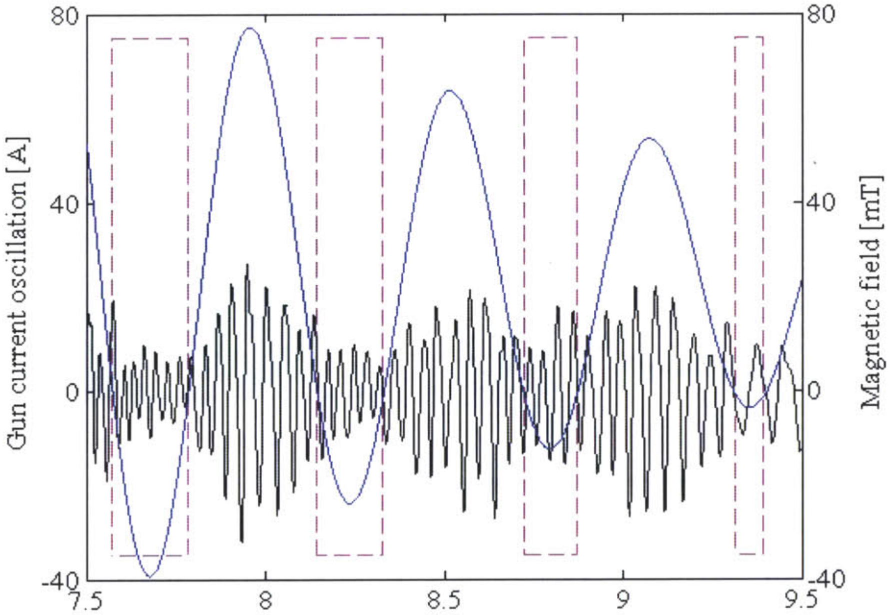

Figure 6-9: Modulation of the oscillations in the total plasma current at the gun output (black) as the null coil current is pulsed (represented by the total estimated field at the center of the coil, blue) for the case when the beam is displaced with respect to the null coil and intersects the Rogowski probe array at the inner probe band. The null phase time intervals are enclosed in magenta.

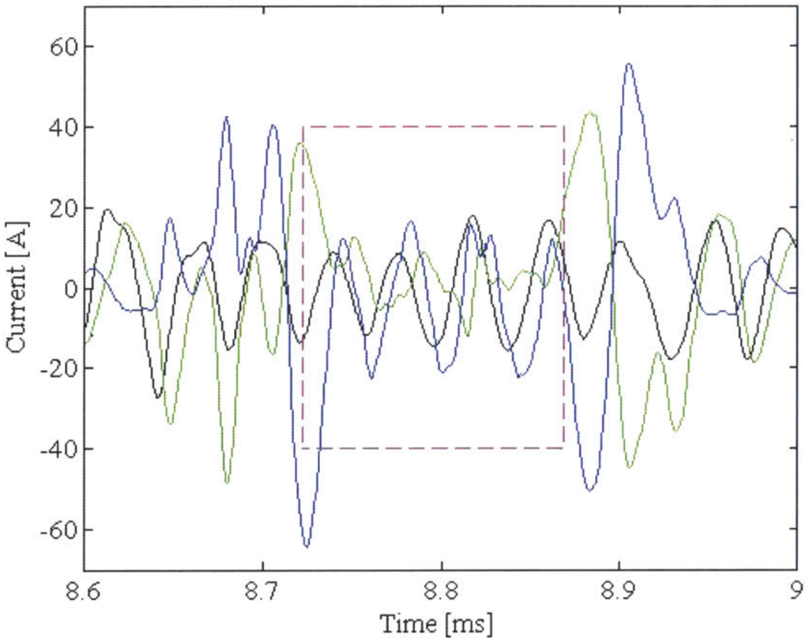

Figure 6-10: Current fluctuation sums in the probes radially inside the null coil (blue) and radially outside the null coil (green) during the null phase (time interval marked in magenta) for the case of plasma beam displaced with respect to the null coil. Also shown are the current fluctuations at the gun output (black).

6.3 Plasma Density Structure

Measurements from Langmuir probes support and complement the Rogowski coil measurements. First, looking at the density measured with the single-string Langmuir probes radially outside the null coil (Fig. 6-11), we again observe the asymmetry in time between the null coil field increasing and decreasing. In the first half of the null phase the dense plasma beam quickly traverses probes in the radially outward direction. The opposite evolution in the second half is less rapid and finite density by the radially inward probe is measured even after the null phase.

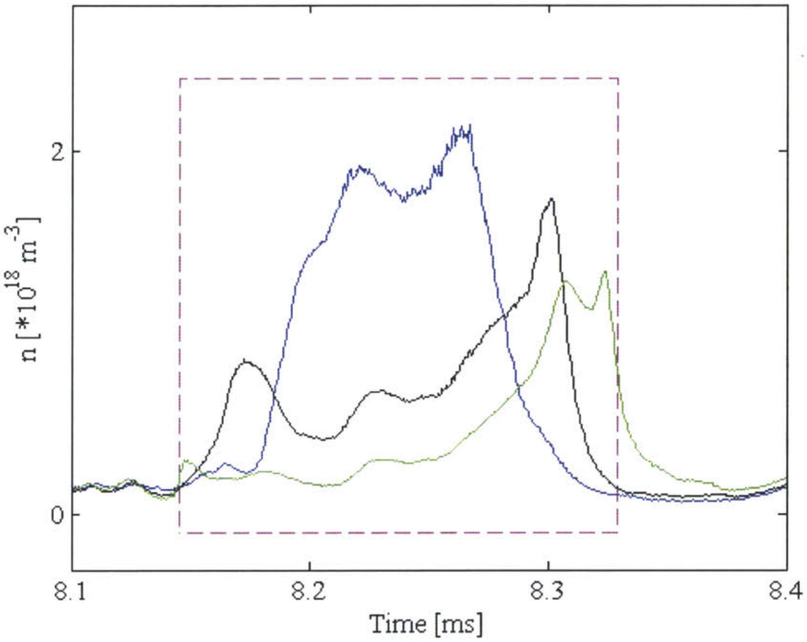

Figure 6-11: Plasma density as measured by the single-string Langmuir probes radially outside the null coil at X = 14.7 cm (green), X = 16.0 cm (black), and X = 17.2 cm (blue).

Next, we use the Langmuir probe array to diagnose the plasma density structure in the x-y plane. After averaging data over ten shots we obtained the density evolution in time depicted in Fig. 6-12. There density surface plots are overlaid with the calculated vacuum field structure (black) for the measured null coil current at each given time. The following observations can be made:

- Plasma follows the magnetic field evolution, except, possibly, near null points,

- High plasma densities ($\sim 1 \cdot 10^{18}$ m^{-3}) are present in the closed field line region,
- During the null phase, density is the largest in the beam on the gun side of the magnetic structure and is less inside the closed field line region. It further decreases in the beam on the bias plate side of the magnetic structure,
- During the X-line phase after the null phase, the plasma beam reaches high density ($>2 \cdot 10^{18}$ m^{-3}) along all of its diagnosed length.

It should be noted that the increased beam density after the null phase is not just a release of the plasma that has accumulated on the upstream (gun) side of the null coil. This can be seen in the density traces in Fig. 6-13. In blue is the average measured plasma density by a single probe within the plasma beam on the gun side of the null coil at Y = -12.5 cm. In black is the same measurement at Y = +12.5 cm. Density indeed increases upstream of the null coil during the null phase. However, there is a spike in density immediately after the null phase not only downstream of the null coil but also upstream.

We do not observe increases in the plasma density after the null phase in the experiments with the displaced beam. The measured average density profiles are shown in Fig. 6-14 (note the different density scale). In comparison to the experiments with the plasma beam centered on the null coil (Fig. 6-12) less plasma is accumulated in the magnetic configuration during the null phase. The lower plasma density then allows for faster Alfvén dynamics and explains the field line reconnection without a significant plasma current response.

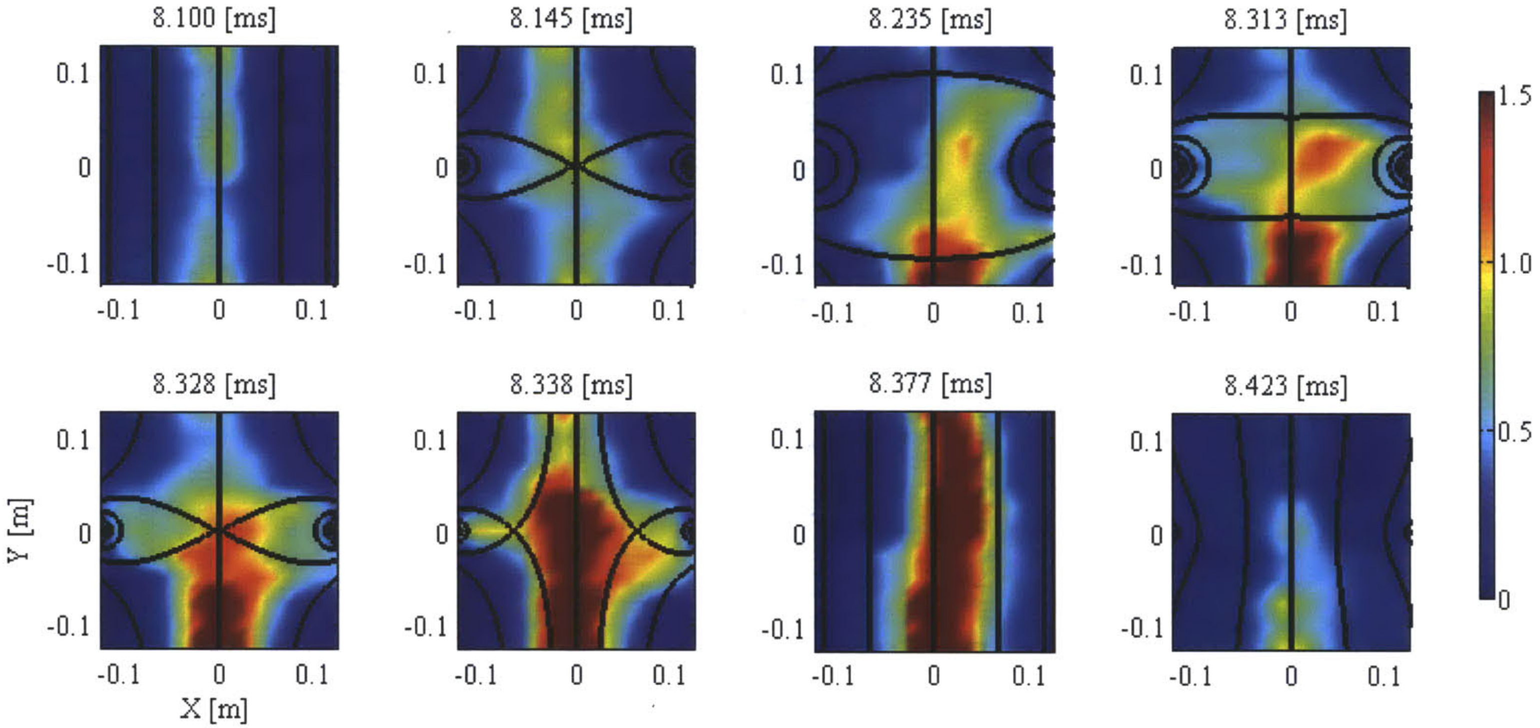

Figure 6-12: Average density evolution in time. Overlaid in black is the calculated vacuum field structure. Density is measured in 10^{18} m^{-3}.

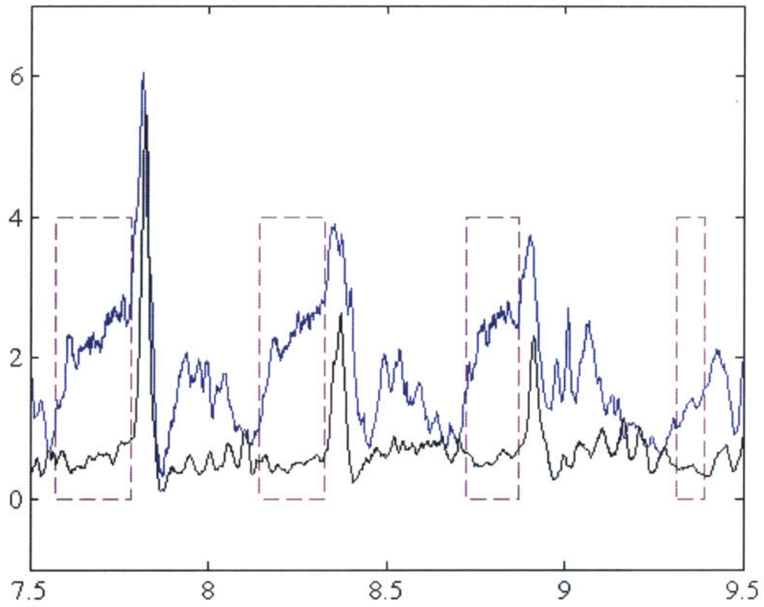

Figure 6-13: Average plasma density measured by a single probe upstream of the null coil (Y = -12.5 cm, blue) and downstream of the null coil (Y = +12.5 cm, black).

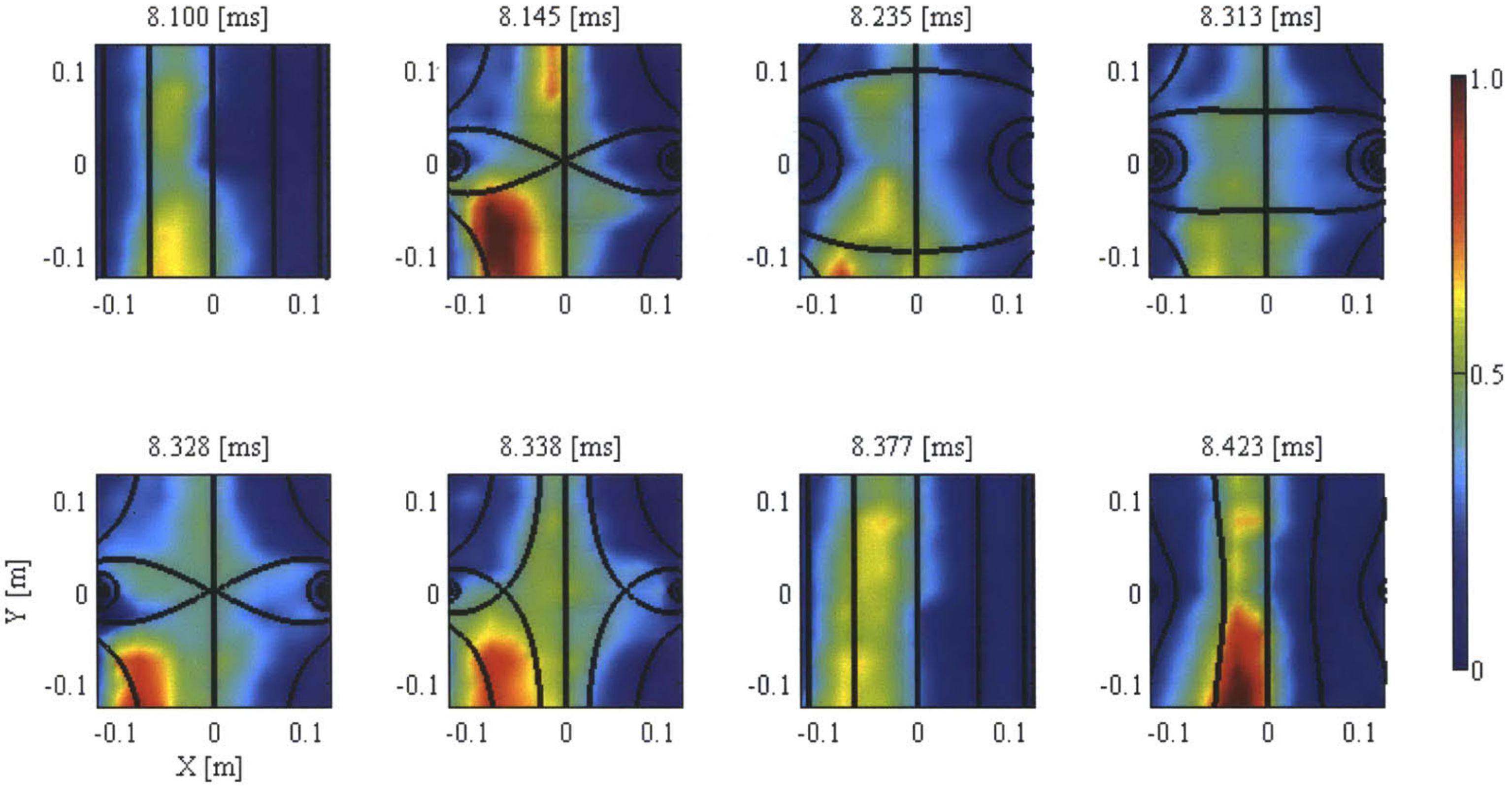

Figure 6-14: Average density evolution in time for the normal configuration with plasma beam displaced. Overlaid in black is the calculated vacuum field structure. Density is measured in 10^{18} m^{-3}.

6.4 Electron temperature

Returning to the configuration with the plasma beam centered, we can investigate the electron temperature evolution in time. We focus on probes and time intervals without beam oscillations, which leads to well defined averages over several shots. In Fig. 6-15 we plot electron temperature in a region of the x-y plane at select times overlayed with the calculated vacuum field lines (black). The four panels correspond to the following experimental times (see also Fig. 6-12):

1. Largest null coil current leading to the two null points the most displaced during the given null coil current oscillation,
2. Null point near Y = 5.5 cm and within the area diagnosed with the Langmuir probe array. Also, we observe pronounced signature in the magnetic coil array data (see Fig. 6-16 below),
3. End of the null phase and beginning of the X-line phase. Single null point present,
4. Pronounced current loop signature in the Rogowski array data (Fig. 6-8).

We observe the following:

- Electrons along the spine remain at low temperatures (<15 eV). Electrons are at higher temperatures (>15 eV) on the closed field lines in the top two panels,
- We observe no temperature signature for the null point,
- Electrons are heated to ~20 eV during the reconnection phase at X ~ -2 cm along the spine.

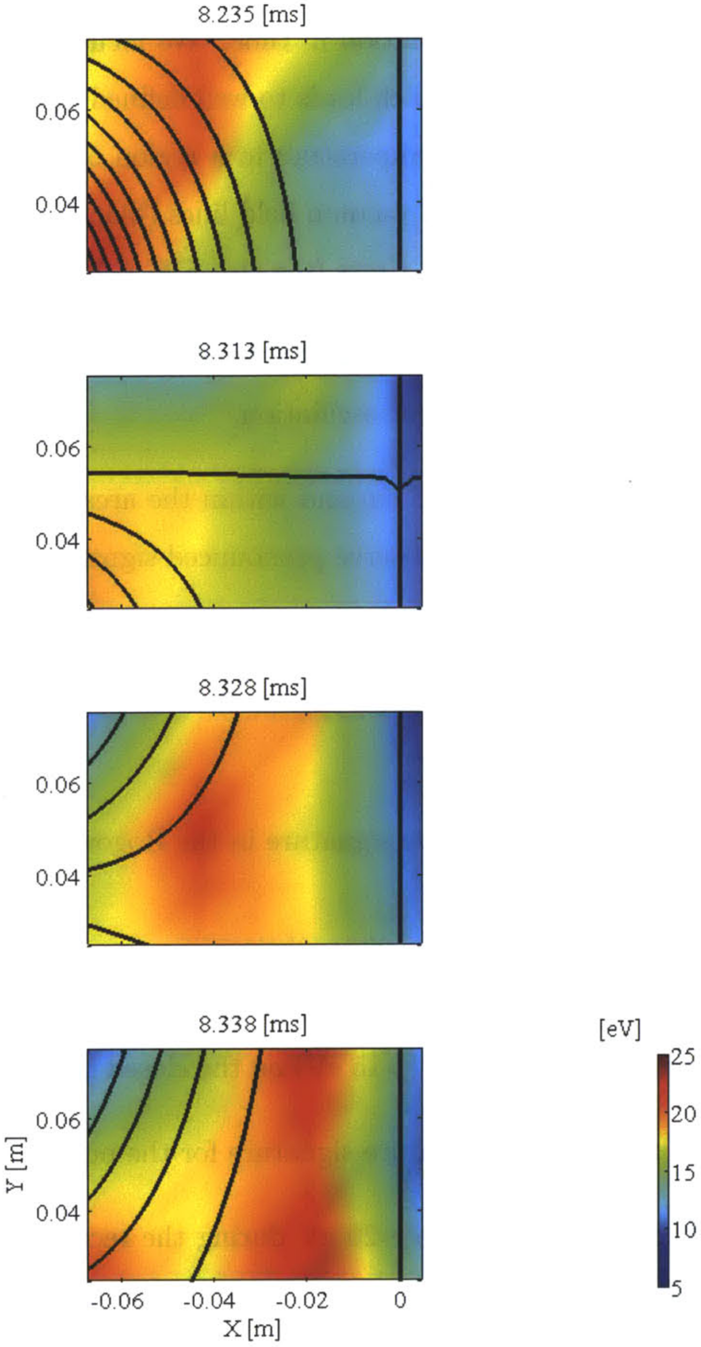

Figure 6-15: Electron temperature at select times overlaid with the calculated vacuum field lines (black).

6.5 Magnetic Coil Array Measurements

Additional important observations can be made using the magnetic coil array data. In Fig. 6-16 we present the experimentally observed z-component of the plasma current at three select times. For reference, we also plot the z-component of the vacuum electric field induced by the changing current in the null coil. Overlaid in black are the vacuum magnetic field configurations. The first two times were already used in the context of other diagnostics above: with null points near Y = ± 5.5 cm and during the X-line phase. The third time exhibits pronounced azimuthal current described further in Section 6.5.2. We also use this select time in Fig. 6-17 to illustrate the measured magnetic fields due to plasma currents that are then used to infer these currents.

6.5.1 Diamagnetic Currents Across Separatrices

As can be seen in the top panel of Fig. 6-16, the two null points are associated with current rings of opposite polarity. We interpret these currents as diamagnetic currents induced by pressure gradients across the separatrices. Recall that in the fluid model diamagnetic current density J_d is given by [63]:

$$\mathbf{J}_d = -\nabla \times \left(\frac{P_\perp \hat{B}}{B} \right), \tag{6.1}$$

where $P_\perp$ is pressure perpendicular to the magnetic field of magnitude B and direction $\hat{B}$. For uniform magnetic field Eq. 6.1 becomes

$$\mathbf{J}_d = -\frac{\nabla P_\perp \times \mathbf{B}}{B^2}. \tag{6.2}$$

Assuming our plasmas of essentially uniform temperature thus with pressure determined by density then we expect higher pressure on the gun side of the lower null than on the closed field lines between the nulls and even lower pressure on the open field lines on the bias plate side of the magnetic structure (see Fig. 6-12). The predicted directions of diamagnetic currents are illustrated in Fig. 6-18 and are in agreement with the observations.

Quantitatively from Eq. 6.2 it follows that

$$J_d \sim \frac{\nabla P_\perp}{B} \sim \frac{k_B T_e}{B} \frac{\delta n}{\delta x}. \tag{6.3}$$

For $\delta n \sim 1 \cdot 10^{18}$ m^{-3}, $\delta x \sim 5$ cm, $T_e \sim 20$ eV, and $B \sim 10$ mT then $J_d \sim 0.6$ A/m^2 in agreement with observations.

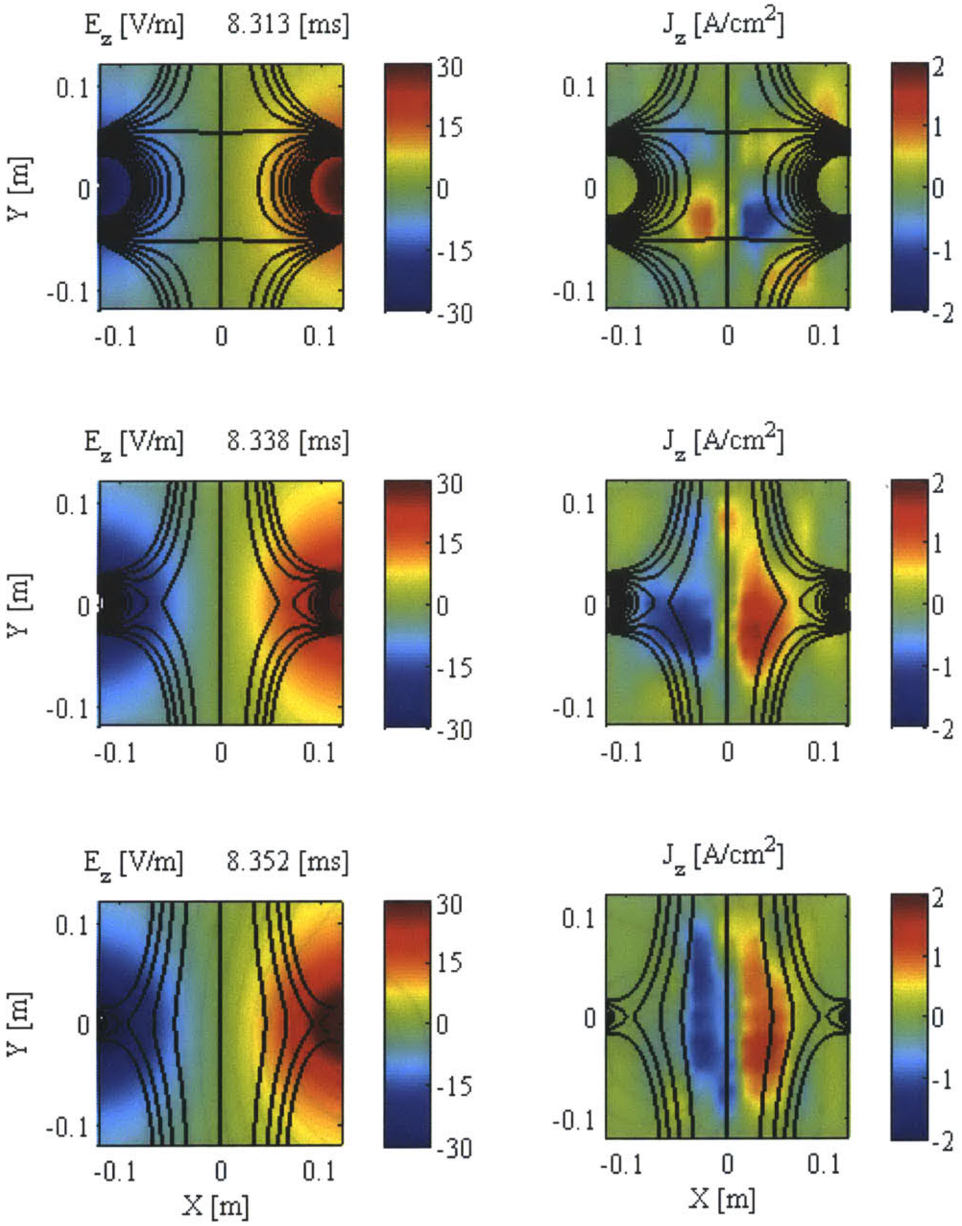

Figure 6-16: The measured z-component of the plasma current (right) at select times: when the null points are near Y = ±5.5 cm (top), during the X-line phase (middle), and with pronounced azimuthal currents (bottom). Also shown is the z-component of the vacuum electric field induced by the changing current in the null coil (left). Overlaid (black) are the vacuum magnetic field configurations.

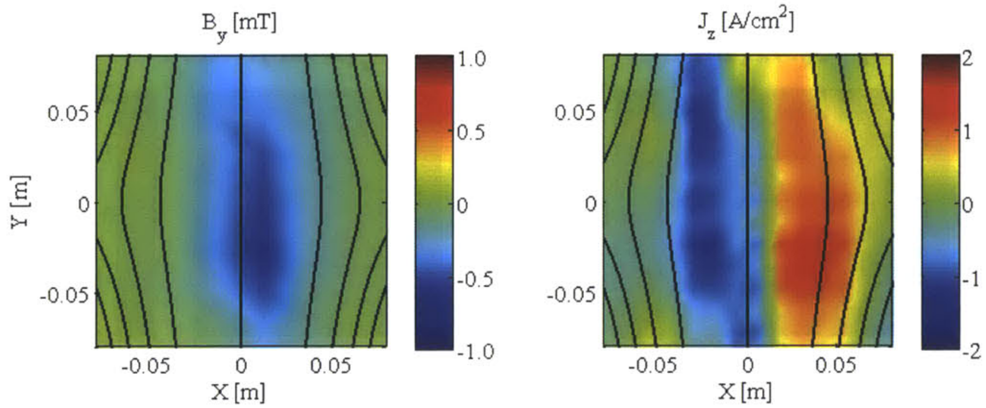

Figure 6-17: An example measured B_y component of the magnetic field (left) due to pronounced inferred azimuthal plasma currents (right).

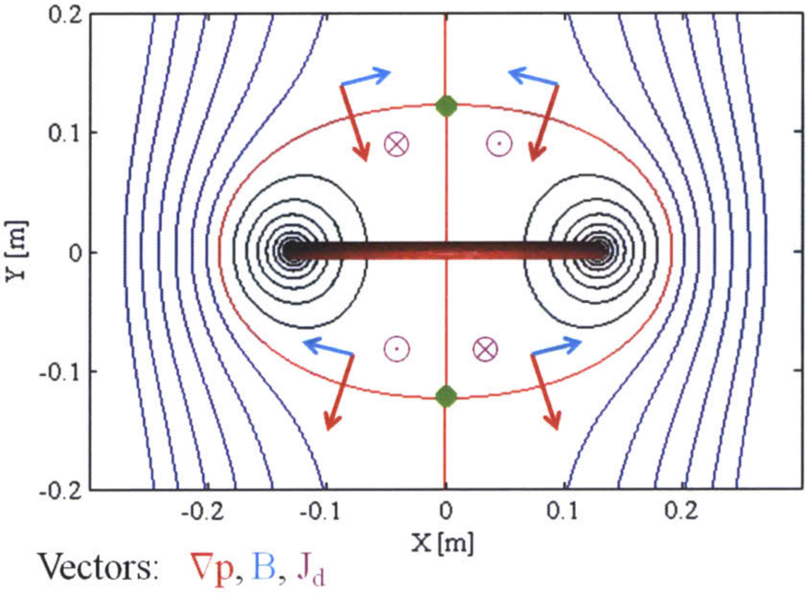

0.2
0.1
0
-0.1
-0.2
-0.2
-0.1
0
0.1
0.2
Y [m]
X [m]
Vectors: ∇p, B, J$_d$

Figure 6-18: The expected diamagnetic current polarities (purple) near null points based on pressure gradient (red vectors) and magnetic field (blue vectors) directions.

6.5.2 Reconnection and Azimuthal Current Sheet

As shown in the middle panel of Fig. 6-16, during the X-line phase we observe a pronounced plasma current encircling the spine in the driving electric field direction. Initially localized near the null coil plane with time it extends in the ±y-direction similarly to the increased plasma density (Fig. 6-12) and forms an azimuthal current sheet encompassing the gun plasma beam as shown in the bottom panel of Fig. 6-16.

The current surrounding the X-line can be identified as the reconnection current sheet. The measured plasma current J $\sim$ 1 A/cm^2 for a vacuum driving electric field E $\sim$ 10 V/m implies effective resistivity $\eta^* \sim 10^{-3}$ Ω·m much higher than the classical Spitzer resistivity $\eta_{SP} < 10^{-5}$ Ω·m in our experiments. This discrepancy suggests that the reconnection observed cannot be explained as Sweet-Parker reconnection mediated by the classical Spitzer resistivity. It is not surprising as fast electron kinetic effects are bound to play an important role in our reconnection experiments possibly invalidating predictions based on fluid models. The importance of the kinetic effects is indicated by the Dreicer (runaway) electric field [66] for electrons:

$$E_D = 0.43\,\frac{ne^3 \ln\Lambda}{8\pi\epsilon_0^3 k_B T_e}, \tag{6.4}$$

which for our parameters is $E_D \sim 2$ V/m and is comparable to the driving electric field. Recall that the Dreicer electric field is the characteristic minimum electric field that in the absence of all loss mechanisms other than the electron-ion collisional drag can accelerate electrons to high (even relativistic) energies.

Our observations of the reconnection rate significantly larger than explained by the classical Spitzer resistivity are consistent with the results from the Magnetic Reconnection Experiment (MRX) [67]. The authors in their experiments varied the plasma collisionality and correspondingly observed different magnetic reconnection modes ranging between the MHD Sweet-Parker regime and the two fluid Hall reconnection regime. An empirical scaling for the effective resistivity as a function of the ratio of the ion skin depth d_i to the Sweet-Parker current sheet width δ was obtained (Fig. 6-19). In our experiments $d_i \sim 1$ m and, based on Eq. 1.18, $\delta \sim 3$ mm resulting in a ratio $d_i/\delta \sim 500$. While this parameter ratio is outside the reported range for the MRX reconnection scaling, qualitatively an extrapolation would predict a large effective resistivity exceeding $\eta^* = 25$ consistent with our observations.

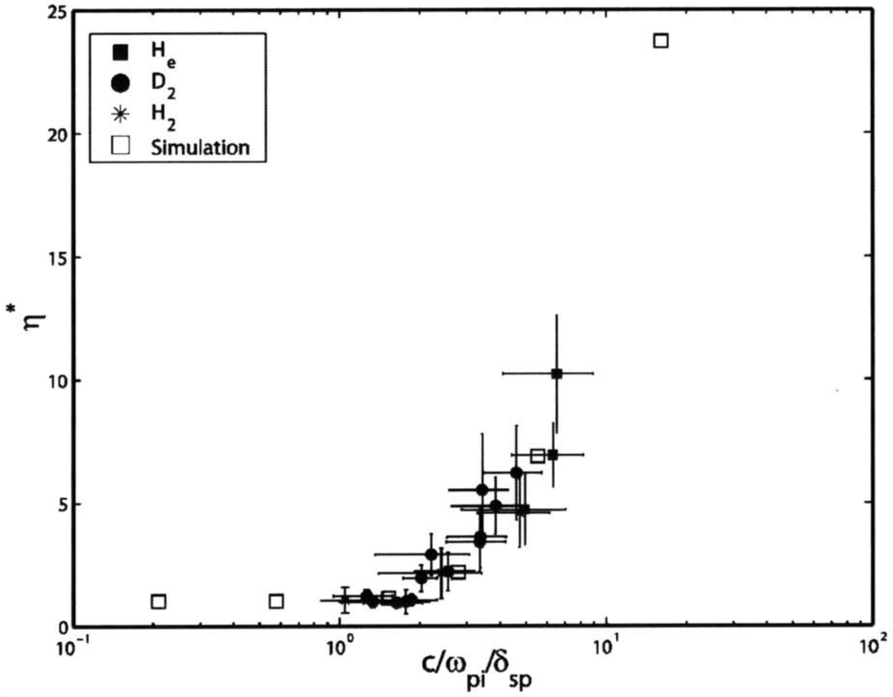

Figure 6-19: The empirical scaling for the effective resistivity in MRX as a function of the ratio of the ion skin depth d_i to the Sweet-Parker current sheet width δ. Reproduced from [67].

In addition to the X-line reconnection current sheet, we observe an azimuthal current sheet. Noteworthy that while the increased density lasts into the compression phase, the azimuthal current sheet disappears as the current in the null coil switches polarity. We explain this sheet as an additional current driven along the twisting field lines of the gun plasma beam. A possible source for the drive is the electric field induced by the null coil and plotted in the left panels in Fig. 6-16. Another source is, again, the diamagnetic currents accompanying the increased plasma density. As illustrated in Fig. 6-20 now the density gradients are predominantly parallel to the x-axis towards the origin, the magnetic field is in the y-direction, and the resulting diamagnetic currents according to Eq. 6.2 encircle the gun plasma beam in the same direction as observed.

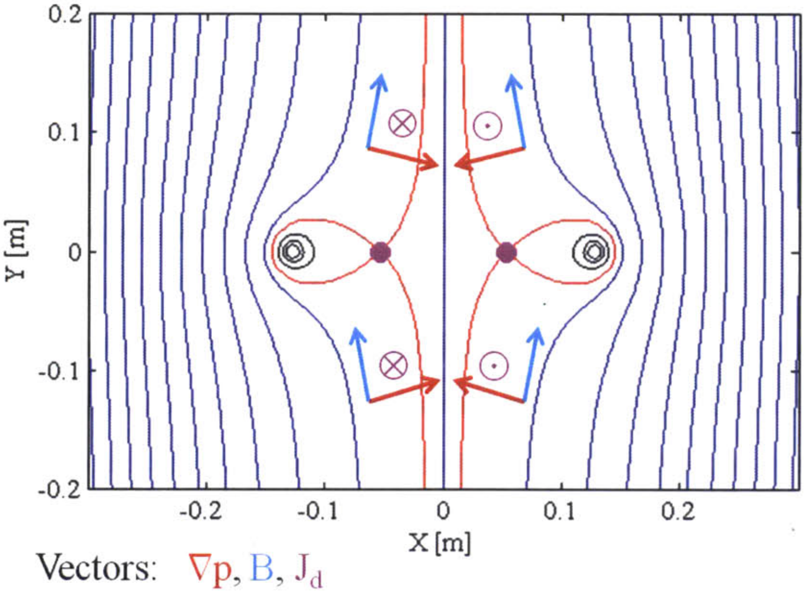

Figure 6-20: The expected diamagnetic current polarities (purple) for the plasma beam based on the pressure gradient (red vectors) and the magnetic field (blue vectors) directions.

6.6 Summary and Interpretation

We observe that in the normal configuration with the beam centered on the coil the plasma beam oscillations are almost extinguished during the null phase. These oscillations persist in a configuration with the beam displaced.

At the null points, we observe current loops, which we explain as diamagnetic currents due to pressure gradients across the separatrices. We believe that dynamics at the null points lead to anti-correlated current fluctuations crossing the null coil plane radially inside the null coil and radially outside. We do not observe anti-correlated fluctuations in the displaced beam configuration.

We observe reconnection along a circular X-line after the null phase. The evidence is as follows:

1. A current loop corresponding to the reconnection current sheet observed in the Rogowski array data and in the magnetic coil data,

2. An increase in plasma density around and along the spine upstream and downstream of the null coil,

3. Electron heating at the location of the current loop.

The observed reconnection is faster than explained by the classical Spitzer resistivity and is qualitatively consistent with an extrapolated MRX magnetic reconnection scaling. Since the driving electric field is comparable to the Dreicer electric field then kinetic effects are likely important in explaining the fast reconnection.

The X-line current sheet is observed to transition to an azimuthal current sheet surrounding the gun plasma beam and also consistent with diamagnetic currents.

Reconnection after the null phase leads to a delay in the plasma beam and field dynamics compared to the time interval with the same null coil drive but before the null phase when no reconnection is observed.

Visible light images qualitatively confirm the overall magnetic field structure of the normal configuration.

Chapter 7

Results for the Tilted Configuration

7.1 Magnetic Field Structure

Again, the visible light images from the fast camera provide qualitative confirmation of the overall magnetic field structure of the tilted configuration that was described in Chapter 4. Fig. 7-1 shows the plasma beam intersecting the null coil plane before the beam bias is applied and the null coil is fired. Beam again intersects the null coil plane in the center only the coil itself is tilted out of the poloidal plane. When the null coil is fired, the visible beam plasma again outlines the magnetic field structure similar to that in Fig. 4-6. In particular, in the image in Fig. 7-2 taken during the null phase from the bottom view the darker area surrounding the null coil actually consists of striations as would be expected for a plasma filament encircling the coil. In addition, one can see visible plasma tracing the spine in the bottom left corner of the image after approaching the null point along the original beam in the middle of the image. Plasma spread to the spine in the opposite direction to its original flow can also be seen to the bottom in the camera bottom view in Fig. 7-2 and to the left in the camera top view in Fig. 7-3. The encircling structure of field lines is even more prominent in Fig. 7-4 from an experiment where the beam is displaced and here seen when the null coil is fired but before the bias is applied.

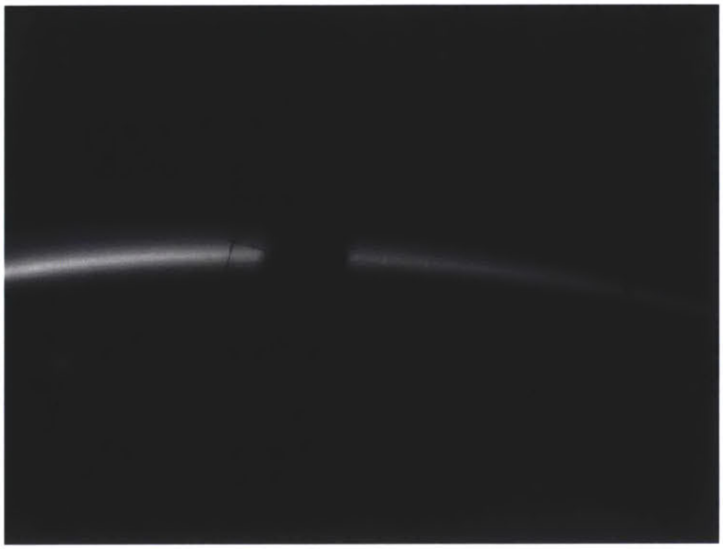

Figure 7-1: Plasma beam before the beam bias is applied and the null coil is fired in a visible light fast camera image from the bottom view. Beam intersects the tilted null coil plane in the center.

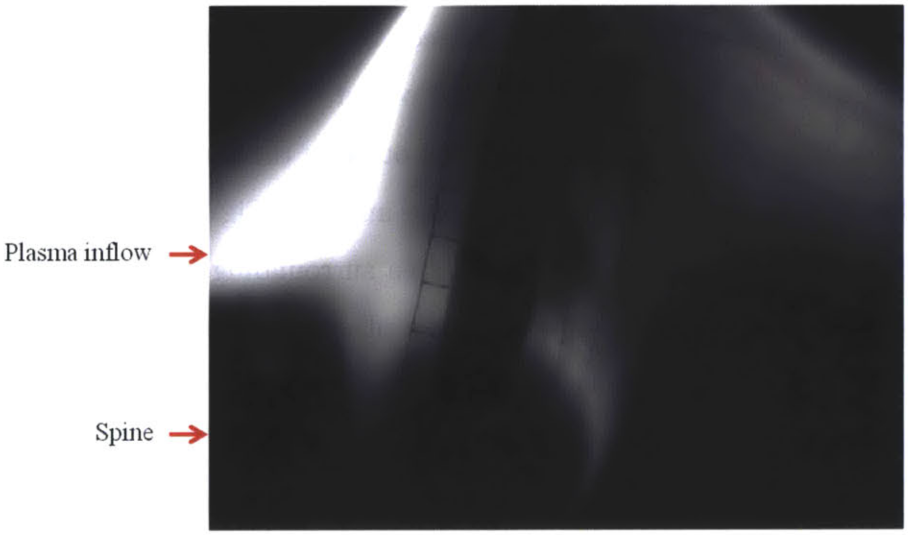

Figure 7-2: Fast camera bottom view during the null phase for the tilted configuration. Note the plasma spread to the spine in the opposite direction to its original flow.

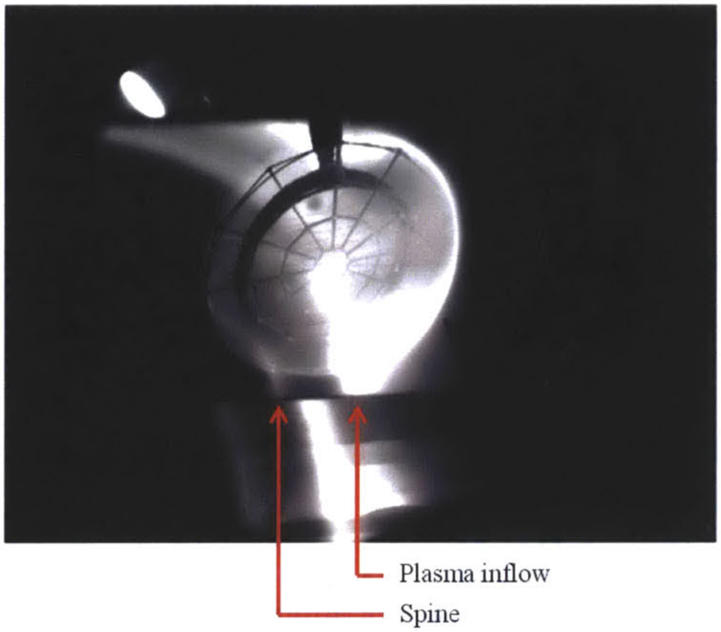

Figure 7-3: Fast camera top view during the null phase for the tilted configuration. Note the plasma spread to the spine in the opposite direction to its original flow.

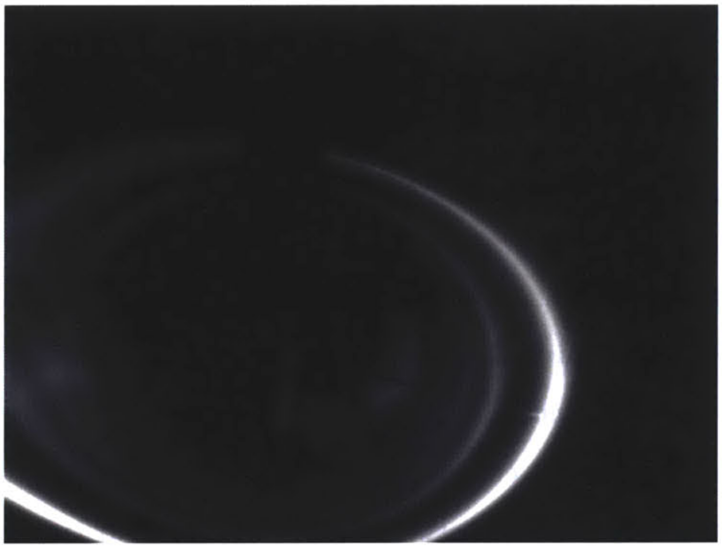

Figure 7-4: Fast camera bottom view for a displaced plasma beam before bias is applied but the null coil is already fired.

7.2 Current and Plasma Density Structures

As was the case for the normal configuration with the beam displaced, the beam current oscillations for the tilted configuration are modulated by the null coil but are still present during the null phase. This is shown in Fig. 7-5.

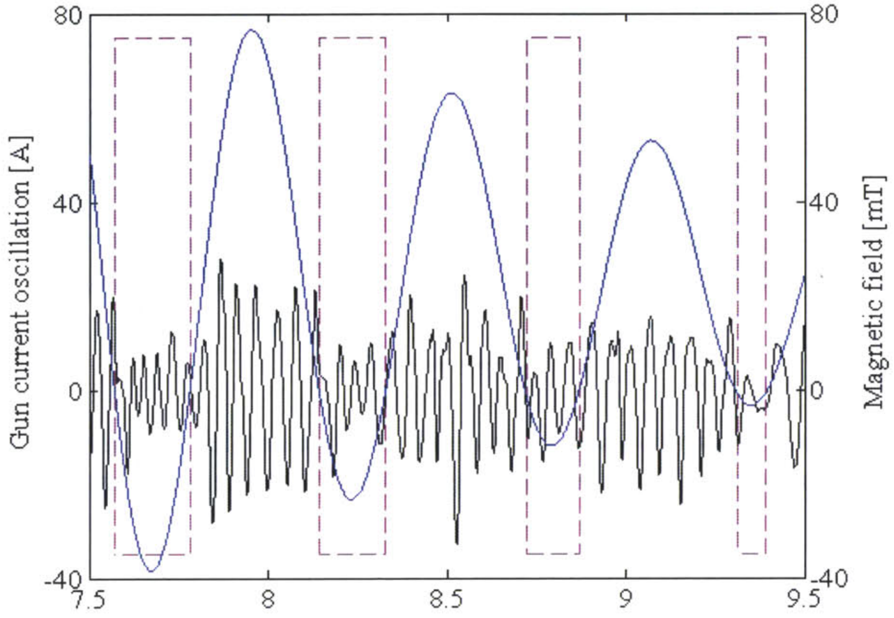

Figure 7-5: Modulation of the oscillations in the total plasma current at the gun output (black) as the null coil current is pulsed (represented by the total estimated field at the center of the coil, blue) for the tilted configuration. The null phase time intervals are enclosed in magenta.

However, as shown in Fig. 7-6 and unlike in the normal configuration with the displaced beam (Fig. 6-10), we still observe current oscillations anti-correlated between probes radially inside the null coil and radially outside.

Neither the total plasma current oscillations nor the anti-correlated oscillations exhibit the asymmetry in time between when the coil field is increasing and when decreasing. We also did not observe any pronounced current loop signatures of the kind shown in Fig. 6-8 for the case of null coil centered on the beam.

As for the plasma density measurements in the tilted configuration, we do not observe any increases in plasma density during the X-line phase after the null phase.

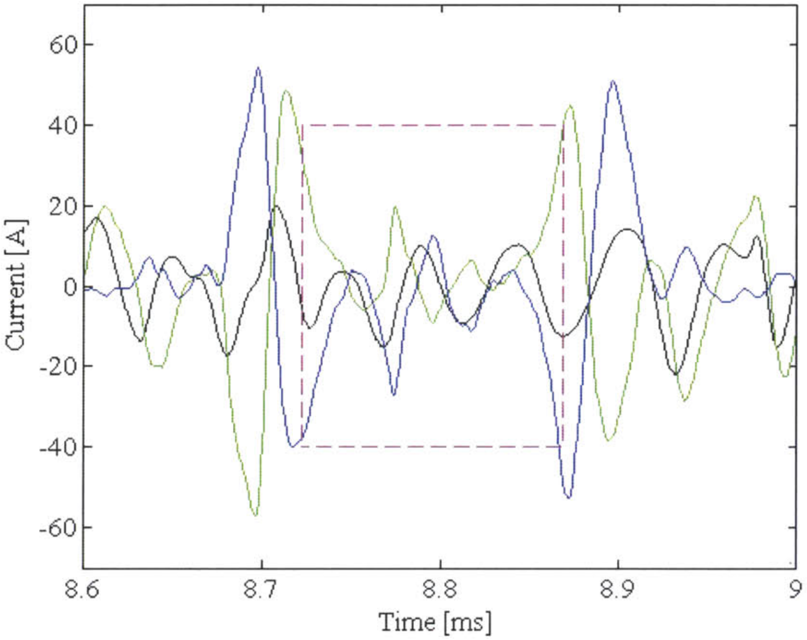

Figure 7-6: Anti-correlated current fluctuations in the probes radially inside the null coil (blue) and radially outside the null coil (green) during the null phase (time interval marked in magenta) for the tilted configuration. Also shown are the current fluctuations at the gun output (black).

Plasma density measurements at select times are presented in Fig. 7-7. As was the case for the experiments with the displaced plasma beam in the normal configuration, the low plasma density allows for faster Alfvén dynamics and explains the field line reconnection without a significant plasma current response.

7.3 Interpretation

Based on the presented measurements for the tilted configuration we conclude that null point dynamics leading to anti-correlated current fluctuations are still present in the tilted configuration. However, we do not observe signs of X-line reconnection as we did for the normal configuration with the beam centered - plasma beam density does not increase after the null phase, current waveforms are symmetric in time before and after the null phase, and we do not observe a current loop in the Rogowski array data. This field line reconnection without a significant plasma current response is due to the low plasma density which allows for faster Alfvén dynamics.

As was the case for the normal configuration, visible light images qualitatively confirm the overall magnetic field structure of the tilted configuration including field lines encircling the null coil and a spine field line that reverses its direction.

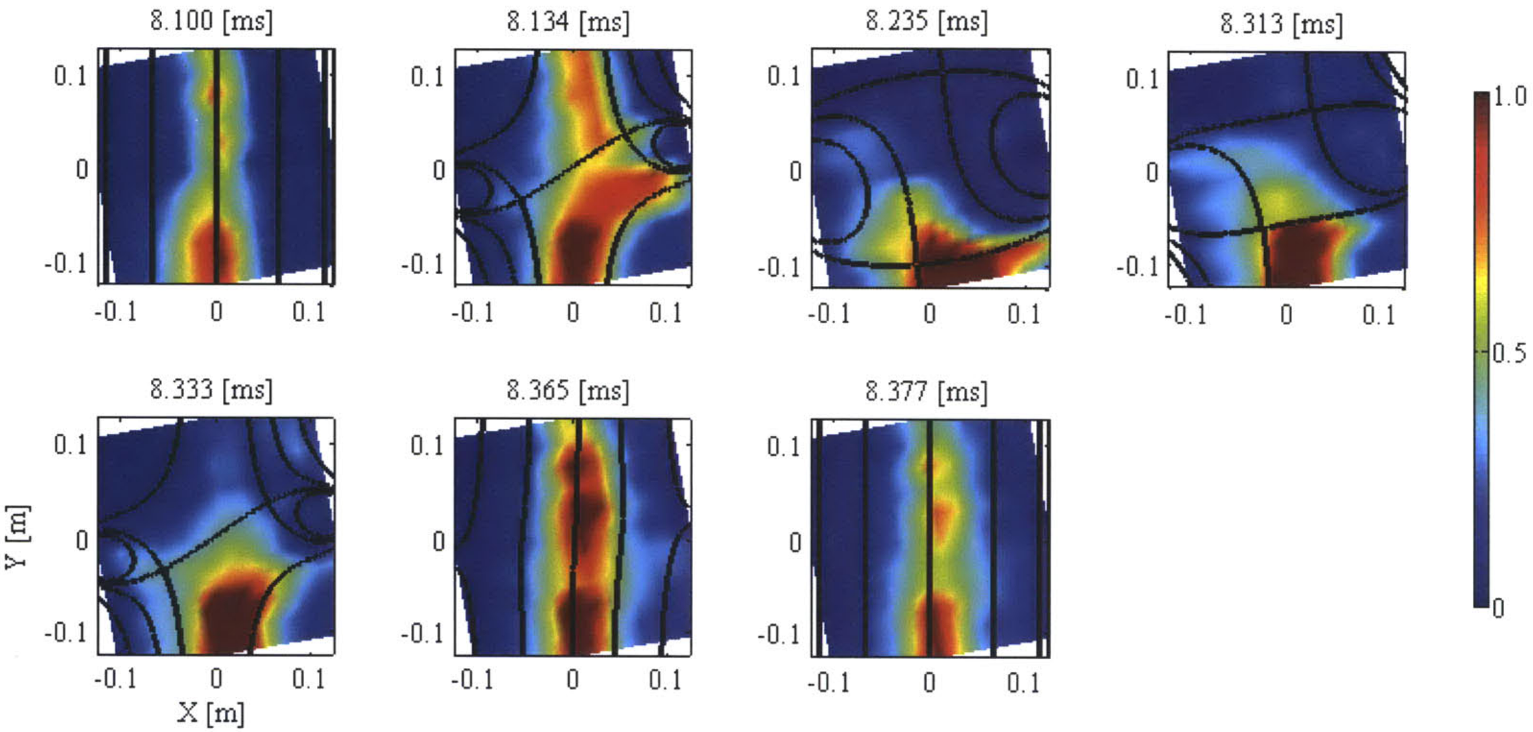

Figure 7-7: Average density evolution in time for the tilted configuration. Overlaid in black is the calculated vacuum field structure. Density is measured in 10^{18} m^{-3}.

Chapter 8

Discussion and Conclusions

Magnetic reconnection is a common and important plasma phenomenon that is not yet fully understood. Unresolved questions include the nature of reconnection in 3D and in this thesis we have attempted to further the knowledge on this topic.

The following has been achieved:

- Designing and constructing an experimental setup for investigating magnetic reconnection in 3D. Setup includes a washer plasma gun and a suite of diagnostics potentially useful in other areas of basic plasma physics research,

- Characterizing the gun plasma beam. We have also observed a plasma beam rotation that we attribute to drift waves,

- Theoretical investigation of magnetic field configurations of a current coil in a background field. Notably, a coil tilted with respect to the background field produces nested separatrix surfaces consisting of field lines that encircle the null coil a certain number of times. The results are, to the best of our knowledge, original, immediately applicable to our experimental setup, and contain features of relevance to the interaction of the Earth's magnetic field with the IMF,

- Experimentally verifying the basic structure of the theoretically investigated magnetic field configurations using a fast visible light camera,

- Driving and diagnosing plasma dynamics in the presence of magnetic nulls. When driving the gun plasma beam with current through the null points we observed fluctuations in the location of the beam between radially inside the null coil and radially outside. Pressure gradient across the separatrix surfaces drives diamagnetic currents near the null points,

- Driving and diagnosing reconnection in a configuration with the null coil aligned with the gun plasma beam and the background magnetic field (normal configuration). We observe plasma heating, the X-line current sheet, and an increase in density in the exhaust. The driving electric field induced by the null coil and the current are not related by the classical Spitzer resistivity. Thus, the observed reconnection cannot be explained as Sweet-Parker reconnection mediated by the classical resistivity. The X-line current sheet extends to an azimuthal current sheet around the plasma beam. The azimuthal current sheet is also consistent with diamagnetic currents.

- Driving and diagnosing plasma dynamics with the null coil tilted with respect to the background field or displaced with respect to the gun plasma beam. We again observed fluctuations in the current between radially inside and radially outside the null coil when the beam targeted a null.

For future work we suggest changing the current in the null coil at a higher rate thus driving faster null point motion in space and forcing a plasma current response to magnetic reconnection at the null points. We also suggest further investigating the cause of the plasma beam oscillations since experiments without the oscillations present would be conceptually simpler and easier to analyze. In addition, a Rogowski coil array that provides not only high frequency current fluctuation measurements but also reliable absolute current readings would allow to further describe the current structure in this experimental setup.

Bibliography

[1] J. W. Dungey. LXXVI. conditions for the occurrence of electrical discharges in astrophysical systems. *Philosophical Magazine Series 7*, 44(354): 725, 1953. ISSN 1941-5982. URL `http://www.informaworld.com/10.1080/14786440708521050`.

[2] Eric R. Priest and Terry Forbes. *Magnetic Reconnection: MHD Theory and Applications.* Cambridge University Press, 2000.

[3] Joachim Birn and Eric R. Priest, editors. *Reconnection of Magnetic Fields: Magnetohydrodynamics and Collisionless Theory and Observations.* Cambridge University Press, 2007.

[4] Ellen G. Zweibel and Masaaki Yamada. Magnetic reconnection in astrophysical and laboratory plasmas. *Annual Review of Astronomy and Astrophysics*, 47(1):291–332, September 2009. ISSN 0066-4146, 1545-4282. doi: 10.1146/annurev-astro-082708-101726. URL `http://www.annualreviews.org/doi/abs/10.1146/annurev-astro-082708-101726`.

[5] Masaaki Yamada, Russell Kulsrud, and Hantao Ji. Magnetic reconnection. *Reviews of Modern Physics*, 82(1):603–664, March 2010. ISSN 0034-6861, 1539-0756. doi: 10.1103/RevModPhys.82.603. URL `http://link.aps.org/doi/10.1103/RevModPhys.82.603`.

[6] G. Paschmann. Space physics: Breaking through the lines. *Nature*, 439:144–145, 2006.

[7] E.R. Priest and T.G. Forbes. The magnetic nature of solar flares. *The Astronomy and Astrophysics Review*, 10(4):313–377, March 2002. ISSN 0935-4956, 1432-0754. doi: 10.1007/s001590100013. URL `http://link.springer.com/10.1007/s001590100013`.

[8] Kazunari Shibata and Tetsuya Magara. Solar flares: Magnetohydrodynamic processes. *Living Reviews in Solar Physics*, 8(6), 2011.

[9] P. F. Chen. Coronal mass ejections: Models and their observational basis. *Living Reviews in Solar Physics*, 8(1), 2011.

[10] J. T. Gosling. Magnetic reconnection in the solar wind. *Space Science Reviews*, 172(1-4):187–200, November 2012. ISSN 0038-6308, 1572-9672. doi: 10.1007/s11214-011-9747-2. URL `http://link.springer.com/10.1007/s11214-011-9747-2`.

[11] J. W. Dungey. Interplanetary magnetic field and the auroral zones. *Physical Review Letters*, 6(2):47, 1961.

[12] Margaret G. Kivelson and C. T. Russell, editors. *Introduction to Space Physics.* Cambridge University Press, 1995.

[13] C. Thompson, M. Lyutikov, and S. R. Kulkarni. Electrodynamics of magnetars: implications for the persistent x-ray emission and spin-down of the soft gamma repeaters and anomalous x-ray pulsars. *The Astrophysical Journal*, 574(1):332, 2002. URL `http://iopscience.iop.org/0004-637X/574/1/332`.

[14] S. von Goeler, W. Stodiek, and N. Sauthoff. Studies of internal disruptions and m=1 oscillations in tokamak discharges with soft x-ray techniques. *Physical Review Letters*, 33:1201, 1974.

[15] N. Sauthoff, S. von Goeler, and W. Stodiek. A study of disruptive instabilities in the PLT tokamak using x-ray techniques. *Nuclear Fusion*, 18:1445, 1978.

[16] John Wesson. *Tokamaks.* International Series of Monographs on Physics. Oxford University Press, 2011.

[17] E. N. Parker. Sweet's mechanism for merging magnetic fields in conducting fluids. *Journal of Geophysical Research*, 62:509, 1957.

[18] J. Birn, J. F Drake, and M. A. Shay. Geospace environmental modeling (GEM) magnetic reconnection challenge. *Journal of Geophysical Research*, 106:3715, 2001.

[19] M. Øieroset, T. D. Phan, and M. Fujimoto. In situ detection of collisionless reconnection in the earth's magnetotail. *Nature*, 412:414, 2001.

[20] Yang Ren, Masaaki Yamada, and Stefan Gerhardt. Experimental verification of the hall effect during magnetic reconnection in a laboratory plasma. *Physical Review Letters*, 95:055003, 2005.

[21] M. Øieroset, R. P. Lin, T. D. Phan, D. E. Larson, and S. D. Bale. Evidence for electron acceleration up to ~300 keV in the magnetic reconnection diffusion region of earth's magnetotail. *Physical Review Letters*, 89(19), October 2002. ISSN 0031-9007, 1079-7114. doi: 10.1103/PhysRevLett.89.195001. URL `http://link.aps.org/doi/10.1103/PhysRevLett.89.195001`.

[22] J. Egedal, W. Daughton, and A. Le. Large-scale electron acceleration by parallel electric fields during magnetic reconnection. *Nature Physics*, February 2012. ISSN 1745-2473, 1745-2481. doi: 10.1038/nphys2249. URL `http://www.nature.com/doifinder/10.1038/nphys2249`.

[23] J. F. Drake, M. Swisdak, H. Che, and M. A. Shay. Electron acceleration from contracting magnetic islands during reconnection. *Nature*, 443(7111):553–556, October 2006. ISSN 0028-0836, 1476-4687. doi: 10.1038/nature05116. URL `http://www.nature.com/doifinder/10.1038/nature05116`.

[24] D. W. Longcope and C. E. Parnell. The number of magnetic null points in the quiet sun corona. *Solar Physics*, 254(1):51–75, January 2009. ISSN 0038-0938, 1573-093X. doi: 10.1007/s11207-008-9281-x. URL `http://link.springer.com/10.1007/s11207-008-9281-x`.

[25] C. J. Xiao, X. G. Wang, Z. Y. Pu, H. Zhao, J. X. Wang, Z. W. Ma, S. Y. Fu, M. G. Kivelson, Z. X. Liu, Q. G. Zong, K. H. Glassmeier, A. Balogh, A. Korth, H. Reme, and C. P. Escoubet. In situ evidence for the structure of the magnetic null in a 3d reconnection event in the earth's magnetotail. *Nature Physics*, 2: 478–483, July 2006. ISSN 1745-2473, 1745-2481. doi: 10.1038/nphys342. URL `http://www.nature.com/doifinder/10.1038/nphys342`.

[26] C. J. Xiao, X. G. Wang, Z. Y. Pu, Z. W. Ma, H. Zhao, G. P. Zhou, J. X. Wang, M. G. Kivelson, S. Y. Fu, Z. X. Liu, Q. G. Zong, M. W. Dunlop, K.-H. Glassmeier, E. Lucek, H. Reme, I. Dandouras, and C. P. Escoubet. Satellite observations of separator-line geometry of three-dimensional magnetic reconnection. *Nature Physics*, 3:609–613, June 2007. ISSN 1745-2473, 1745-2481. doi: 10.1038/nphys650. URL `http://www.nature.com/doifinder/10.1038/nphys650`.

[27] M. Dunlop, Q.-H. Zhang, C.-J. Xiao, J.-S. He, Z. Pu, R. Fear, C. Shen, and C. Escoubet. Reconnection at high latitudes: Antiparallel merging. *Physical Review Letters*, 102, February 2009. ISSN 0031-9007, 1079-7114. doi: 10.1103/PhysRevLett.102.075005. URL `http://link.aps.org/doi/10.1103/PhysRevLett.102.075005`.

[28] K. Schindler, M. Hesse, and J. Birn. General magnetic reconnection, parallel electric fields, and helicity. *Journal of Geophysical Research*, 93:5547, 1988.

[29] M. Hesse and K. Schindler. A theoretical foundation of general magnetic reconnection. *Journal of Geophysical Research*, 93:5559, 1988.

[30] E. R. Priest and D. I. Pontin. Three-dimensional null point reconnection regimes. *Physics of Plasmas*, 16(12):122101, 2009. ISSN 1070664X. doi: 10.1063/1.3257901.

[31] D. I. Pontin. Three-dimensional magnetic reconnection regimes: A review. *Advances in Space Research*, 47:1508, 2011.

[32] J. W. Dungey. The structure of the exosphere, or adventures in velocity space. In C. DeWitt, J. Hieblot, and A. Lebeau, editors, *Geophysics, The Earth's Environments*, page 505. Gordon and Breach, New York, 1963.

[33] S. W. H. Cowley. A qualitative study of the reconnection between the earth's magnetic field and an interplanetary field of arbitrary orientation. *Radio Science*, 8:903, 1973.

[34] J.C. Dorelli, A. Bhattacharjee, and J. Raeder. Separator reconnection at earth's dayside magnetopause under generic northward interplanetary magnetic field conditions. *J. Geophys. Res*, 112:A02202, 2007.

[35] R. L. Stenzel, M. C. Griskey, J. M. Urrutia, and K. D. Strohmaier. Three-dimensional electron magnetohydrodynamic reconnection. i. fields, currents, and flows. *Physics of Plasmas*, 10(7):2780, 2003. ISSN 1070664X. doi: 10.1063/1.1578998. URL `http://scitation.aip.org/content/aip/journal/pop/10/7/10.1063/1.1578998`.

[36] T. Gray, M. R. Brown, C. D. Cothran, and V. S. Lukin. Three-dimensional reconnection and relaxation of merging spheromak plasmas. *Physics of Plasmas*, 17(10):102106, 2010. ISSN 1070664X. doi: 10.1063/1.3492726.

[37] V. S. Lukin and M. G. Linton. Three-dimensional magnetic reconnection through a moving magnetic null. *Nonlinear Processes in Geophysics*, 18(6):871–882, November 2011. ISSN 1607-7946. doi: 10.5194/npg-18-871-2011. URL `http://www.nonlin-processes-geophys.net/18/871/2011/`.

[38] T. P. Intrator, X. Sun, G. Lapenta, L. Dorf, and I. Furno. Experimental onset threshold and magnetic pressure pile-up for 3d reconnection. *Nature Physics*, 5: 521–526, May 2009. ISSN 1745-2473, 1745-2481. doi: 10.1038/nphys1300. URL `http://www.nature.com/doifinder/10.1038/nphys1300`.

[39] Eric E. Lawrence and W. Gekelman. Identification of a quasiseparatrix layer in a reconnecting laboratory magnetoplasma. *Physical Review Letters*, 1103:105002, 2009.

[40] J. Egedal, A. Fasoli, M. Porkolab, and D. Tarkowski. Plasma generation and confinement in a toroidal magnetic cusp. *Review of Scientific Instruments*, 71: 3351, 2000.

[41] W. Fox, M. Porkolab, J. Egedal, N. Katz, and A. Le. Laboratory observation of electron phase-space holes during magnetic reconnection. *Physical Review Letters*, 101(25):255003, December 2008. doi: 10.1103/PhysRevLett.101.255003. URL `http://link.aps.org/doi/10.1103/PhysRevLett.101.255003`.

[42] Noam Katz, Jan Egedal, Will Fox, Ari Le, Jeff Bonde, and Arturs Vrublevskis. Laboratory observation of localized onset of magnetic reconnection. *Physical Review Letters*, 104(25):255004, June 2010. doi: 10.1103/PhysRevLett.104.255004. URL `http://link.aps.org/doi/10.1103/PhysRevLett.104.255004`.

[43] W. Fox, M. Porkolab, J. Egedal, N. Katz, and A. Le. Laboratory observations of electron energization and associated lower-hybrid and trivelpiece–gould wave turbulence during magnetic reconnection. *Physics of Plasmas*, 17:072303, 2010.

[44] Noam Katz, Jan Egedal, Will Fox, Ari Le, Arturs Vrublevskis, and Jeff Bonde. Experimental investigation of the trigger problem in magnetic reconnection. *Physics of Plasmas*, 18(5):055707, 2011. ISSN 1070664X. doi: 10.1063/1.3562937.

[45] Jan Egedal, Noam Katz, Jeff Bonde, Will Fox, Ari Le, Miklos Porkolab, and Arturs Vrublevskis. Spontaneous onset of magnetic reconnection in toroidal plasma caused by breaking of 2d symmetry. *Physics of Plasmas*, 18(11):111203, 2011. ISSN 1070664X. doi: 10.1063/1.3626837.

[46] Noam Katz, Jan Egedal, Will Fox, Ari Le, and Miklos Porkolab. Experiments on the propagation of plasma filaments. *Physical Review Letters*, 101(1):015003, July 2008. doi: 10.1103/PhysRevLett.101.015003. URL `http://link.aps.org/doi/10.1103/PhysRevLett.101.015003`.

[47] David Burke. Toroidal coord.png by DaveBurke (own work) [GFDL (http://www.gnu.org/copyleft/fdl.html), CC-BY-SA-3.0 (http://creativecommons.org/licenses/by-sa/3.0/) or CC-BY-2.5 (http://creativecommons.org/licenses/by/2.5)], via wikimedia commons, September 2006. URL `http://en.wikipedia.org/wiki/Torus`.

[48] I. H. Hutchinson. *Principles of Plasma Diagnostics*. Cambridge University Press, 2nd edition, 2005.

[49] Noam Katz. *Experimental Investigation of the Trigger Problem in Magnetic Reconnection*. PhD thesis, Massachusetts Institute of Technology, Cambridge, MA, 2010.

[50] G. Fiksel, A. F. Almagri, D. Craig, M. Iida, S. C. Prager, and J. S. Sarff. High current plasma electron emitter. *Plasma Sources Science and Technology*, 5:78, 1996.

[51] D. J. D. Hartog, D. J. Craig, G. Fiksel, and J. S. Sarff. Impurities, temperature and density in a miniature electrostatic plasma and current source. *Plasma Sources Science and Technology*, 6:492, 1997. URL `http://iopscience.iop.org/0963-0252/6/4/006`.

[52] N. W. Eidietis. *Non-Inductive Startup of the Pegasus Spherical Torus Using Localized Washer-Gun Current Sources*. PhD thesis, University of Wisconsin-Madison, Madison, WI, 2007.

[53] Kenneth W. Ehlers, James D. Gow, Lawrence Ruby, and John M. Wilcox. Development of an occluded-gas ion source. *Review of Scientific Instruments*, 29(7): 614, 1958. ISSN 00346748. doi: 10.1063/1.1716272. URL `http://scitation.aip.org/content/aip/journal/rsi/29/7/10.1063/1.1716272`.

[54] K. K. Jain, P. I. John, A. M. Punithavelu, and P. P. Rao. Gas injected washer plasma gun. *Journal of Physics E: Scientific Instruments*, 13(9):928, 1980. URL `http://iopscience.iop.org/0022-3735/13/9/008`.

[55] G. I. Dimov and G. V. Roslyakov. A pulsed charge-exchange source of negative hydrogen ions. *Prib. teh. eksp.*, 17(1):29, 1974.

[56] C. Paz-Soldan, W. F. Bergerson, M. I. Brookhart, D. A. Hannum, R. Kendrick, G. Fiksel, and C. B. Forest. The rotating wall machine: A device to study ideal and resistive magnetohydrodynamic stability under variable boundary conditions. *Review of Scientific Instruments*, 81(12):123503, 2010. ISSN 00346748. doi: 10.1063/1.3505487.

[57] I. Furno, T. Intrator, E. Torbert, C. Carey, M. D. Cash, J. K. Campbell, W. J. Fienup, C. A. Werley, G. A. Wurden, and G. Fiksel. Reconnection scaling experiment: A new device for three-dimensional magnetic reconnection studies. *Review of Scientific Instruments*, 74(4):2324, 2003. ISSN 00346748. doi: 10.1063/1.1544051.

[58] D. J. Battaglia, M. W. Bongard, R. J. Fonck, and A. J. Redd. Tokamak startup using outboard current injection on the pegasus toroidal experiment. *Nuclear Fusion*, 51:073029, 2011.

[59] I. Furno, T. Intrator, D. Ryutov, S. Abbate, T. Madziwa-Nussinov, A. Light, L. Dorf, and G. Lapenta. Current-driven rotating-kink mode in a plasma column with a non-line-tied free end. *Physical Review Letters*, 97(1), July 2006. ISSN 0031-9007, 1079-7114. doi: 10.1103/PhysRevLett.97.015002. URL `http://link.aps.org/doi/10.1103/PhysRevLett.97.015002`.

[60] X. Sun, T. Intrator, L. Dorf, I. Furno, and G. Lapenta. Transition of MHD kink-stability properties between line-tied and non-line-tied boundary conditions. *Physical Review Letters*, 100(20), May 2008. ISSN 0031-9007, 1079-7114. doi: 10.1103/PhysRevLett.100.205004. URL `http://link.aps.org/doi/10.1103/PhysRevLett.100.205004`.

[61] M. Kruskal and J. L. Tuck. The instability of a pinched fluid with a longitudinal magnetic field. *Proceedings of the Royal Society A: Mathematical, Physical and Engineering Sciences*, 245(1241):222–237, June 1958. ISSN 1364-5021, 1471-2946. doi: 10.1098/rspa.1958.0079. URL `http://rspa.royalsocietypublishing.org/cgi/doi/10.1098/rspa.1958.0079`.

[62] V. D. Shafranov. The stability of a cylindrical gaseous conductor in a magnetic field. *Atomic Energy*, 5:38, 1956. URL `http://www.springerlink.com/index/X86674703124H306.pdf`.

[63] P. M. Bellan. *Fundamentals of Plasma Physics.* Cambridge University Press, 2008.

[64] W. Horton. Drift waves and transport. *Reviews of Modern Physics*, 71(3):735, 1999. URL `http://journals.aps.org/rmp/abstract/10.1103/RevModPhys.71.735`.

[65] Francis F. Chen. *Introduction to Plasma Physics and Controlled Fusion*, volume 1. Springer, 2nd edition, 2006.

[66] H. Dreicer. Electron and ion runaway in a fully ionized gas. i. *Physical Review*, 115(2):238, 1959. URL `http://journals.aps.org/pr/abstract/10.1103/PhysRev.115.238`.

[67] Masaaki Yamada, Yang Ren, Hantao Ji, Joshua Breslau, Stefan Gerhardt, Russell Kulsrud, and Aleksey Kuritsyn. Experimental study of two-fluid effects on magnetic reconnection in a laboratory plasma with variable collisionality. *Physics of Plasmas*, 13(5):052119, 2006. ISSN 1070664X. doi: 10.1063/1.2203950. URL `http://link.aip.org/link/PHPAEN/v13/i5/p052119/s1&Agg=doi`.